

## AN ABSTRACT OF THE THESIS OF

Xiang Lin for the degree of Master of Science in Wood Science presented on December 01, 2011.

Title: Direct Coupling of Imaging to Morphology-Based Numerical Modeling as a Tool for Mechanics Analysis of Wood Plastic Composites

Abstract approved:

---

John A. Nairn

Polymeric composites reinforced with bio-materials have advantages over composites with synthetic reinforcements. Bio-based composites use low-cost and renewable reinforcements, have nonabrasive properties for machining, have improved damping characteristics, and have potential for energy recycling. However, the limited use of bio-based composites is because their mechanical properties are typically much lower than those of synthetic composites.

The objective of this study was to combine state-of-the-art imaging tools with emerging numerical modeling methods for an integrated, multi-level characterization of bio-based reinforcements and their composites. Digital photography (2D) will allow collection of full-field digital images of the surface of sample composites, which will be used for characterization of the morphological structure of fillers (copper wire or wood particle) and of model composites. Mechanical experiments (tension load) on isolated fillers and on model composites will allow imaging of the deformed material. By correlating relative positions of thousands of surface features between consecutive images, digital image correlation (DIC) algorithms can be used to map surface deformation fields and calculate surface strain fields.

Digital imaging methods can only record deformations and strains. The interpretation of those strains in terms of material properties, such as position-dependent modulus of a heterogeneous composite material, requires simultaneous modeling. The modeling must

use morphology-based methods that can handle anisotropy, heterogeneity, and the complex structure of bio-based composites such as wood plastic composites. This research used the material point method (MPM) as a modeling tool. MPM is a particle-based, meshless method for solving problems in computational mechanics. The crucial advantage of MPM over other methods is the relative ease of translating pixels from digital images into material points in the analysis. Thus digital images (2D) used in our experiments were used as direct input to the MPM software, so that the actual morphologies, rather than idealized geometries, were modeled. This procedure removes typical uncertainties connected with idealization of the internal features of modeled materials. It also removes variability of specimen to specimen due to morphology variations.

Full-field imaging techniques and computer modeling methods for analysis of complex materials have developed independently. This research Coupled imaging and modeling and used inverse problem methodology for studying bio-particulate composites. The potential of coupling experiments with morphology-based modeling is a relatively new area. This work studied the morphology and mechanical properties of copper wire (for validation experiments) and wood particles used for reinforcement in polymer composites. The goal was to determine the in situ mechanical and interfacial properties of copper wire and then wood particles. By comparison of DIC results to MPM, the conclusion is MPM simulation works well by simulating 3D composite structure and using Matlab software to do qualitative and quantitative comparisons. Copper validation tests showed that copper wire is too stiff compared to polymer such that the inclusion modulus had low effect on the surface strains (DIC experimental results). Wood particle worked better because modulus of wood is much lower than copper. By qualitative comparison of the wood particle specimens, we could deduce that the in situ properties of wood particles are lower than bulk wood. Quantitative analysis concentrated on small area and got more exact results. In a 90 degree particle quantitative study, MPM simulations were shown to be capable of tracking the structure of wood particle plastic, which involved failure. The entire approach, however, is not very robust. We can get some results for mechanical properties, but it does not seem possible to extract all anisotropic properties from a few DIC tests, as some researcher have suggested.

©Copyright by Xiang Lin  
December 01, 2011  
All Rights Reserved

Direct Coupling of Imaging to Morphology-Based Numerical Modeling as a Tool for  
Mechanics Analysis of Wood Plastic Composites

by  
Xiang Lin

A THESIS

submitted to

Oregon State University

in partial fulfillment of  
the requirement for the  
degree of

Master of Science

Presented December 01, 2011  
Commencement June, 2012

Master of Science thesis of Xiang Lin presented on December 01, 2011.

APPROVED:

---

Major Professor, representing Wood Science

---

Head of the Department of Wood Science and Engineering

---

Dean of the Graduate School

I understand that my thesis will become part of the permanent collection of Oregon State University libraries. My signature below authorizes release of my thesis to any reader upon request.

---

Xiang Lin, Author

## ACKNOWLEDGEMENTS

This research was funded by the US Department of Agriculture.

I would like to express sincere appreciation to my major professor, Dr. John A Nairn for his guidance and patience in the last three years, and professor, Dr. Lech Muszyński for his valuable advice and help. Dr. Edward. Lee in the Department of Wood Science and Engineering at OSU provided great help with learning MPM software. Matthew J. Schwarzkopf in the Department of Wood Science and Engineering helped me in the mechanical testing and DIC experiments. Special thanks should be given to all the faculty and staff in Wood Science Department community, with whom I spent really wonderful three years in Corvallis. I would also like to say thank you to my parent for their support and assistance.

## CONTRIBUTION OF AUTHORS

Matthew J. Schwarzkopf assisted with experimental data collection. Dr. John A. Nairn was involved with the writing of Chapter 1-6.

## TABLE OF CONTENTS

### Page

CHAPTER 1. INTRODUCTION .....	1
CHAPTER 2: MATERIAL POINT METHOD (MPM) RESOLUTION STUDY .....	17
CHAPTER 3: VIRTUAL INTERFACE STUDY .....	25
CHAPTER 4: COPPER WIRE VALIDATION STUDY .....	38
CHAPTER 5: WPC EXPERIMENTS AND QUALITATIVE ANALYSIS .....	66
CHAPTER 6: WPC QUANTITATIVE ANALYSIS .....	94
CHAPTER 7: CONCLUSION AND FUTUREWORK .....	108
BIBLIOGRAPHY .....	110



## LIST OF FIGURES

<u>Figure</u>	<u>Page</u>
Figure 1.1: Extruder .....	3
Figure 1.2: Extruder equipment: (a) cooling section, (b) Tractor, (c) Cutter, (d) Handling table ....	4
Figure 1.3: Application of wood plastic composite: (a) bench, (b) garbage bin, (c) Flooring, (d) French.....	9
Figure 1.4: WPC decking .....	10
Figure 1.5: WPC products (a) WPC panels, (b) WPC Joist, (c) WPC pipe, (d) WPC siding .....	10
Figure 2.1: A schematic view of a two-dimensional MPM calculation.....	17
Figure 2.2: Visualization of specimen surface and converted image. a. micrograph of copper/polymer composite surface. b. converted 256 level grayscale (black and white) bitmap image .....	18
Figure 2.3: Four different element sizes, from left to right are 0.05 by 0.05mm, 0.025 by 0.025mm, 0.0125 by 0.0125mm, and 0.00625 by 0.00625mm. ....	19
Figure 2.4: Different resolution on Copper-PE Composite. A has cellsize 0.05 by 0.05mm, B has cellsize 0.025 by 0.025mm, C has cellsize 0.0125 by 0.0125mm, and D has cellsize 0.00625 by 0.00625mm. ....	20
Figure 2.5: Tension experiment for 2D MPM model, the yellow part is zero-displacement boundary, green part is copper, and arrow represents applied load .....	21
Figure 2.6: Time-stress plot with different damping property with element size 0.5 by 0.5mm..	22
Figure 2.7: (a) Time-Stress plot (b) Time-Strain Energy plot. Circle indicates elements size 0.25 by 0.25mm, square indicates elements size 0.0125 by 0.0125mm, and triangle indicates elements size 0.00625 by 0.00625mm.....	22
Figure 3.1: View for three dimensional interphase and two dimensional interface .....	26
Figure 3.2: A schematic view of shear sliding displacement and normal displacement, $u_n$ and $u_t$ are the normal and tangential discontinuities displacement; $D_n$ and $D_t$ are the interface parameters .....	26
Figure 3.3: Sample for numerical model. (a). left is 3D sample drawing. (b) right is simplified wood particle model.....	27

## LIST OF FIGURES(Continued)

<u>Figure</u>	<u>Page</u>
Figure 3.4: 2D Material point method model for sample composite, the rectangular in the center of sample represents wood particle, material around it is polymer matrix, and there are two crack line(imperfect interface) between wood particle and polymer matrix.....	28
Figure 3.5: radial opening (X loading) and tangential sliding (Y loading) on MPM simulation. (a). Radial opening with crack interface on tangential plane. (b). Longitudinal sliding with crack interface on tangential plane. (c). Longitudinal sliding with crack interface on tangential plane and cross section. ....	30
Figure 3.6: X-loading (radial opening), For $Dt = \infty$ , vary $Dn$ .....	31
Figure 3.7: X-loading (radial opening), For $Dn = \infty$ , vary $Dt$ .....	32
Figure 3.8: Y-loading model 1 (longitudinal sliding), For $= \infty$ , vary.....	32
Figure 3.10: Y-loading model 2 (longitudinal sliding). For $Dt = \infty$ , vary $Dn$ .....	33
Figure 3.9: Y-loading model 1 (longitudinal sliding). For $Dn = \infty$ , vary $Dt$ .....	33
Figure 3.11: Y-loading model 2 (longitudinal sliding), For $Dn = \infty$ , vary $Dt$ .....	34
Figure 3.12: MPM Visual results of axial (x direction) strain for radial opening (X loading) model. (a). Perfect interface model. (b). Interfacial properties $Dt = \infty$ and $Dn = 200$ .....	35
Figure 3.13: MPM Visual results of transverse (Y direction) strain for longitudinal sliding (Y loading) model 2 (four crack lines). (a). Interfacial properties $Dn = Dt = \infty$ . (b). Interfacial properties $Dt = 1000$ and $Dn = \infty$ . (c). Interfacial properties $Dt = 10$ and $Dn = \infty$ . ....	36
Figure 4.1: Stress-strain relationship for copper wire experiment (DIC) and pure polymer MPM 2D simulation, solid line represents pure polymer MPM 2D simulation results and broken line represents copper wire experiment results. ....	39
Figure 4.2: Visualization of a part of specimen surface. This micrograph images area of $2.25 \times 1.6$ mm. ....	40
Figure 4.3: Visualization of specimen surface and converted image. a. micrograph of copper composite. b. converted 256 level grayscale bitmap image .....	41
Figure 4.4: Tension experiment on 2D MPM simulation, the red part is polymer, green part is copper wire, and arrow on the right represents applied load .....	42

## LIST OF FIGURES(Continued)

<u>Figure</u>	<u>Page</u>
Figure 4.5: Visual axial strain results. (a) DIC axial strain results for copper wire specimen. (b) Magnification of DIC results (c) MPM 2D simulation of axial strain result for copper wire sample. ....	43
Figure 4.6: 3D strain distribution. (a). 2D visualization of strain on centre layer (x-y plane). (b). 2D visualization of strain on layer far away from inclusion(x-y plane). (c). 3D visualization of strain on centre layer (x-y plane). (d). 2D visualization of strain on layer far away from inclusion(x-y plane).....	44
Figure 4.7: Layer containing copper fiber. (a) Visualization of MPM on a layer contain fiber. (b) Structure of one layer on 3D MPM simulation .....	45
Figure 4.8: 3D MPM simulation structure for copper wire specimen, the coordinate of each layer is on thickness (Z) direction. Gap between layers is 0.069 mm .....	46
Figure 4.9: 3D symmetric simulation on MPM for Copper-Polymer Composite, the coordinate of each slice is on thickness (Z) direction. Interval is 0.0345 mm. ....	47
Figure 4.10: Tension experiment for MPM model, the red part is boundary condition, green part is polymer matrix, and black dashed line represents copper wire inside matrix .....	47
Figure 4.11: Illustration of transferred data form from DIC and MPM results.....	49
Figure 4.12: Visual image of DIC axial strain .....	52
Figure 4.13: Effect of different fiber modulus on axial strain for layer with coordinate 0.0345 mm .....	53
Figure 4.14: Effect of different fiber modulus on axial strain for layer with coordinate 0.138mm .....	54
Figure 4.15: Effect of different fiber modulus on axial strain for layer with coordinate 0.3795 mm .....	55
Figure 4.16: Visual image of DIC transverse ( $\epsilon_{yy}$ ) strain .....	56
Figure 4.17: Effect of different fiber modulus on transverse strain. (a) Wire modulus 30000MPa ( coordinate z=0.138). (b) Wire modulus 120000MPa ( coordinate z=0.138). (c) Wire modulus 30000MPa (coordinate z=0.3795). (d) Wire modulus 120000MPa (coordinate z=0.3795).....	57
Figure 4.18: Visual image of DIC shear strain .....	58
Figure 4.19: Effect of different fiber modulus on shear strain .....	59

## LIST OF FIGURES(Continued)

<u>Figure</u>	<u>Page</u>
Figure 4.20: Four selected regions on DIC axial strain field.....	60
Figure 4.21: Deviation error for selected regions in a layer with coordinate $z = 0.3795\text{mm}$ .....	61
Figure 4.22: Deviation error for axial strain in a layer with coordinate $z = 0.3795\text{mm}$ .....	62
Figure 4.23: Sensitivity analysis for MPM simulations .....	63
Figure 4.24: Deviation error for transverse strain. Layer with coordinate $z = 0.3795\text{mm}$ . ....	64
Figure 4.25: Deviation error for shear strain. Layer with coordinate $z = 0.3795\text{mm}$ . ....	64
Figure 5.1: Visualization of a part of WPC sample surface used in the MPM simulations. (a) 0 degree wood particle sample. (b) 90 degree wood particle sample. (c) 45 degree wood particle sample. ....	67
Figure 5.2: Converted 256 level grayscale bitmap image. (a) 0 degree wood particle sample. (b) 90 degree wood particle sample. (c) 45 degree wood particle sample. ....	71
Figure 5.5: Simple 3D MPM simulation model, assumed half sample is from coordinate $Z = 0$ to $0.325\text{mm}$ and assumed half wood particle is from $Z$ coordinate $0$ to $0.1083\text{mm}$ .....	74
Figure 5.4: Simple 3D MPM simulation model, half sample is from coordinate $Z = 0$ to $0.315\text{mm}$ ; half wood particle is from coordinate $Z = 0$ to $0.105\text{mm}$ .....	74
Figure 5.3: Simple 3D MPM simulation model, half sample is from coordinate $Z = 0$ to $0.37917\text{mm}$ ; half wood particle is from coordinate $Z = 0$ to $0.11667\text{mm}$ .....	74
Figure 5.6: Tension experiment for MPM model, the red part is boundary condition, green part is polymer matrix, and black dashed line represents wood particle inside matrix .....	75
Figure 5.7: DIC result for axial strain.....	76
Figure 5.8: Tension results of MPM simulation for axial strain with wood particle properties sample 1 (8834MPa). (a) Layer with coordinate $0.1458\text{mm}$ . (b) Layer with coordinate $0.2605\text{mm}$ . (c) Layer with coordinate $0.3792\text{mm}$ .....	77
Figure 5.9: Tension results of MPM simulation for axial strain in a layer with coordinate $0.3792\text{mm}$ (a) Inclusion property is sample 2. (b) Inclusion property is sample 3. (c) Inclusion property is sample 5.....	78

## LIST OF FIGURES(Continued)

<u>Figure</u>	<u>Page</u>
Figure 5.10: Tension results of MPM simulation for transverse strain with wood particle properties sample 2 and sample 3 (coordinate $Z = 0.3792\text{mm}$ ). (a). transverse strain with inclusion property sample 2. (b). transverse strain with inclusion property sample 3. (c) DIC results for transverse strain .....	80
Figure 5.11: Tension results of MPM simulation for shear strain in a layer with coordinate $Z = 0.3792$ . (a). Shear strain with inclusion property sample 2. (b). Shear strain with inclusion property sample 3. (c) DIC results for shear strain .....	81
Figure 5.12: DIC results of axial strain .....	82
Figure 5.13: Tension results of MPM simulation with wood particle properties sample 1 in different layer. (a) Layer with coordinate $0.315\text{mm}$ . (b) Layer with coordinate $0.21\text{mm}$ . (c) Layer with coordinate $0.1575\text{mm}$ .....	83
Figure 5.14: Tension results of MPM simulation in a layer with coordinate $Z = 0.1575\text{mm}$ . (a). Axial strain with inclusion property sample 2. (b). Axial strain with inclusion property sample 3 .....	84
Figure 5.15: Axial strain results of MPM tension simulation for different yield strength in a layer with coordinate $Z = 0.1575\text{mm}$ .....	85
Figure 5.16: Axial strain results of MPM tension simulation for different wood particle transverse modulus in a layer with coordinate $Z = 0.1575\text{mm}$ . (a). Axial strain with inclusion property sample 3. (b). Axial strain with inclusion property sample 6. (c). Axial strain with inclusion property sample 7. ....	87
Figure 5.17: Axial strain in a layer with coordinate $Z = 0.1575\text{ mm}$ .....	88
Figure 5.18: Transverse strain in a layer with coordinate $z = 0.1575\text{ mm}$ (a). low yield stress MPM simulation results; (b). low transverse modulus MPM simulation results. ....	89
Figure 5.19: Shear strain in a layer with coordinate $z = 0.1575\text{ mm}$ .....	90
Figure 5.20: Example of measured angle of wood particle area, (a) DIC axial strain result. (b) One MPM axial strain simulation result. ....	91

## LIST OF FIGURES(Continued)

<u>Figure</u>	<u>Page</u>
Figure 5.21: Relationship between angles of wood particle axial strain area with layer coordinate Z (wood particle property is sample 1). (a). Angle In a layer with coordinate 0mm. (b). Angle In a layer with coordinate 0.1083mm. (c). Angle In a layer with coordinate 0.2166mm. (d). Angle In a layer with coordinate 0.325mm. ....	92
Figure 5.22: Fiber strain angle changes with fiber modulus. The solid circle, solid triangle, broken line, solid squares, and solid line indicate sample 5 (longitudinal modulus 1104MPa), sample 3 (longitudinal modulus 2208MPa), sample 2 (longitudinal modulus 4417MPa), sample 1 (longitudinal modulus 8834MPa), and DIC result. ....	92
Figure 6.1: Visualization result of axial strain on 0 degree study. (a)DIC results (b) one MPM simulation results .....	97
Figure 6.2: Axial strain ( $\epsilon_{xx}$ ) deviation error of Region A in two layers. Layer 1 is indicated with coordinate Z = 0.2334mm; Layer 2 is indicated with coordinate Z = 0.35mm.....	98
Figure 6.3: Transverse strain $\epsilon_{yy}$ deviation error of Region A on layer with coordinate Z = 0.35mm. ....	99
Figure 6.4: Shear strain $\tau_{xy}$ deviation error of Region A on layer with coordinate Z = 0.35mm.	100
Figure 6.5: Visualization result of axial strain on 90 degree study. (a)DIC results (b) one MPM simulation results. ....	100
Figure 6.6: Deviation error for 90 degree MPM simulation results for axial strain with different wood particle yield strength (Layer with coordinate z=0.315mm). Here wood particle modulus is the same as sample 2 to sample 6 in table 6.1 but with different yield strength property (table 6.4). Triangle, square, and circle were indicated with normal yield strength (sample 18), 1/4 yield strength (sample 19), and 1/8 yield strength (sample 20).....	101
Figure 6.7: Deviation error for 90 degree MPM simulation results of axial strain with different wood particle transverse modulus (Layer with coordinate z=0.315mm). Triangle, square, and circle are indicated with normal transverse modulus (samples 2 to 6); 1/2 transverse modulus (samples 8 to 12), and 1/4 transverse modulus (samples 13 to 17). ....	102

## LIST OF FIGURES(Continued)

<u>Figure</u>	<u>Page</u>
Figure 6.8: Deviation error for transverse strain. (Layer with coordinate $z=0.315\text{mm}$ ). (a)	
Deviation error for transverse strain with different wood particle yield strength. (b)	
Deviation error for transverse strain with different wood particle transverse modulus. ....	103
Figure 6.9: Visualization result of axial strain on 45 degree study. (a)DIC results (b) one MPM	
simulation results. ....	104
Figure 6.10: 45 degree axial strain deviation error of Region C in a layer with coordinate $Z =$	
$0.325\text{mm}$ . ....	105
Figure 6.11: 45 degree transverse strain deviation error of Region C in a layer with coordinate $Z$	
$= 0.325\text{mm}$ . ....	105
Figure 6.12: 45 degree shear strain deviation error of Region C in a layer with coordinate $Z =$	
$0.325\text{mm}$ . ....	106

## LIST OF Tables

<u>Table</u>	<u>Page</u>
Table 3.1: Sample and wood particle size.....	28
Table 3.2: Wood particle properties.....	29
Table 5.1: Wood particle modulus on different sample.....	69
Table 5.2: Yield strength used from sample 1 to sample 7.....	69
Table 5.3: Different yield stress with wood particle modulus the same as sample 3 .....	84
Table 5. 4: Different transverse modulus for wood particle .....	86
Table 6 2: Yield strength used from sample 1 to sample 17.....	95
Table 6 1: Wood particle modulus on different sample .....	95
Table 6 3: Modulus of Low transverse modulus sample .....	96
Table 6 4: Different yield stress with wood particle modulus from sample 1 to sample 7 on table 6.1.....	96



## LIST OF APPENDICES

<u>Appendices</u>	<u>Page</u>
Appendix A: Matlab code for qualitative and quantitative analysis.....	115



## CHAPTER 1. INTRODUCTION

### 1.1 DEVELOPMENT OF WOOD PLASTIC COMPOSITE (WPC)

Wood plastic composites are widely used in the U.S. They are wood-based composite materials in the shape of lumber made from thermoplastic polymer, wood particles as fines or flour, and additives such as coupling agents, stabilizers, and dyes. Wood fibers have potential for reinforcing plastics due to their relative high strength and stiffness, low cost, low density, low  $CO_2$  emission, biodegradability and renewability. In addition, WPCs have some advantages over traditional timber products. WPCs are environmentally friendly because they use waste wood and recycled plastic material and they do not need to be treated with preservatives. They have insect resistance, improved water resistance, require less maintenance, and have longer service life than wood. WPCs have somewhat improved stiffness compared to plastic. Compared to solid wood, they have lower stiffness and strength, but may have higher toughness.

Compared to the long history of traditional wood composites such as particleboard or fiberboard, wood plastic composites are relatively new products. Although wood flour has been used as a filler in plastics (primarily thermosetting polymers) for decades, the use of wood in thermoplastics is a relatively recent phenomenon spurred by improvements in processing technology and other factors. It was first developed several decades ago as a way to make use of recycled plastics such as polyethylene jugs and polyethylene bags, and wood wastes, such as sawdust, generated by furniture factories and lumber mills.

WPCs were initially used in automobile and secondary building applications that had relatively low structural requirements, such as tables, decking, flooring, window frames, and some other products. Since treated lumber products have some disadvantages, such as long-term maintenance, surface characteristics, and straightness, WPC decking gained some relative success. In addition, WPCs were believed to be resistant to biodegradation, which raised hopes for the development of a material that could replace increasingly scrutinized treated wood in structures exposed to the nature (Clemons 2002; Wolcott and Smith 2004).

The importance and growing potential of wood plastic composites were evidenced in 1991 by the advent of the international conference on wood fiber-plastic composites, which is a forum on the science and technology for the processing and development of these materials (Smith 2001).

Though WPCs have developed very fast in recent years, the mechanics of WPCs are not well understood. Here are some unsolved problems:

- a. What are the properties of the flour particle within the WPC?
- b. Why do flour particles not reinforce stiffness and strength more?
- c. How can WPC products be improved?

This thesis addresses these questions by numerical modeling of wood flour/plastic specimens. The modeling is compared to experimentally determined strain fields around isolated particles. The goal is to understand the mechanics of reinforcement in WPCs.

### **WPC market**

In general, high density polyethylene (HDPE) is the most widely used plastic for making commercial WPC products. Low density polyethylene (LDPE), poly (vinyl chloride) (PVC) and polypropylene (PP) also have a share in the global market. Finally, a small amount of thermosetting plastics, such as phenol-formaldehyde or diphenyl methane diisocyanate, are sometimes used in composites with a high wood content (Clemons 2002).

As replacements for more traditional materials, such as natural wood, WPCs have a large world wide market. The demand for wood-plastic composites and plastic lumber in the US is projected to advance 9.2 percent per year to \$5.3 billion in 2013, creating a market for 3.3 billion pounds of plastic (The Freedonia Group 2009).

The application of WPCs in China is more extensive. Chinese production includes WPC products such as windows, doors, thermal insulating systems, park benches, garden sheds and sun screens for tower buildings. The growth of WPCs in China is at a level of 30 percent per year. Chinese WPC production is predicted to increase 10 billion pounds per year between now and 2015 (Michael Carus 2010).



**Figure 1.1: Extruder**

(Source: Figure 1.1 is from [www.clima.org.cn](http://www.clima.org.cn))

### **Manufacturing of WPC**

Manufacturing of WPCs is a two-step process. The first step is compounding to mix wood flour and thermoplastic. The second step is called forming.

There are three common forming methods for WPC forming - Extrusion method, Injection molding method, and compression molding method (Clemons 2002). Most WPCs are manufactured by extrusion. The extrusion process uses a variety of extruder types such as single screw or double screw to form final shape of the material. An extrusion line is a set of equipment intended for extruding WPC products in the plant. The primary unit of an extrusion line is the extruder machine. Downstream parts include modules located after the extrusion die: cooling section, take-off unit, cutter, and a handling table. To achieve required extrudate the compound is fed into the extruder through a gravity filling bunker. It is heated and melted to uniform flow mass inside the cylinder of the extruder (Clemons 2002). The melt flow is then transferred and pressed through the slit of the die shape to provide final cross section geometry. This is done by screw rotation inside the extruder cylinder. The next stage is the cooling section. Cooling systems are a very important factor of the extrusion process. Usually, uniform cooling is around or along the outlet of the extrusion die. The extrudate is pulled through water and cooled. While passing under water along the cooling tank the extruded profile is subjected to shrinkage due to a temperature drop. However the size of the product depends not only on cooling but also on the speed of traction ([www.asian-sources.com.hk](http://www.asian-sources.com.hk) 2006).



(a)



(b)



(c)



(d)

**Figure 1.2: Extruder equipment: (a) cooling section, (b) Tractor, (c) Cutter, (d) Handling table**

(Source: Figure 1.2 a is from [www.centuryextrusion.com](http://www.centuryextrusion.com), Figure 1.2 b is from [www.tradenote.net](http://www.tradenote.net), Figure 1.2 c is from [www.toreuse.com](http://www.toreuse.com), Figure 1.2 d is from [www.asian-sources.com](http://www.asian-sources.com))

Traction is applied by a caterpillar-type tractor machine, which pulls the extruded blank through the water tank, pushing it further on downstream to the cutter and handling table. The tractor pulls the extruded profile with uniform speed, without allowing it to slip. This process is closely related to final dimensions of the finished product. The cutter is a device that fixes the extruded profile and cuts it to desired length by means of a thermal knife. To cut the profile to desired length the blank is placed along the handling table, following the cutter. Cut pieces are delivered to the finished profile collector ([www.asian-sources.com.hk](http://www.asian-sources.com.hk) 2006).

## 1.2 Effects of Wood Particle Characteristics on WPC Properties

WPCs are composed of wood particles and polymer in different proportions. Mechanical properties of wood plastic composites generally depend on the properties of their components and the ratio of these components. Usually, wood particle has grain size ranging from 20 to 60 mesh (1 $\mu$ m = 12500 mesh), and the polymer mass content of WPC is higher than the wood particle content, therefore, WPCs are morphologically closer to short-fiber reinforced composites than conventional wood fiberboard or particleboard. The wood particles play an important role in the properties of the resulting composites. Many studies show significant effects related to variables such as coupling agents, types of thermoplastic matrix and additives. However, WPC properties are also significantly affected by wood particle quality and characteristics. Usually, size and species of wood particles are two of the most important factors (Berger and Stark 1997).

Wood species have an important influence on the properties of wood plastic composites. The main reason is that the wood structure controls the flow direction of the thermoplastic movement in cell lumens. The location where the wood material is collected from the log can affect mechanical properties of the wood particles. Berger and Stark (1997) described the mechanical properties of PP filled with wood particles of different species (ponderosa pine, loblolly pine, maple and oak). They measured properties including tensile strength and MOE, flexural strength and MOP, tensile elongation, mold shrinkage, and impact energy. They compared performances of composites to find the species' effect and conclude that hardwood particles provide an improvement in tensile properties over soft wood particles but the best overall mechanical property enhancements were with ponderosa pine particles.

Another important factor affecting properties of the wood component in a WPC is wood particle size. The effect of this factor on WPC mechanical properties was evaluated for typical WPCs containing small wood particles or short fibers (Manas Chanda et al. 2008). Much work has been done to study the effects of wood particle size on the properties of WPCs. However, different effects of particle sizes were observed by different researchers. Stark and Rowlands (2003) studied the influence of wood flour particle size on mechanical properties of the resulting composites, and compared mechanical properties of wood-flour

filled and wood-fiber-reinforced composites in relationship to aspect ratio. They found the use of wood fiber instead of wood flour resulted in higher strengths and higher modulus. Furthermore, It is generally accepted that aspect ratio, not particle size, has the greatest effect on strength and stiffness on the composites. Kim et al. (2005) studied mechanical properties of rice husk flour (RHF) and wood flour (WF) filled polybutylene succinate (PBS) biocomposites. A general conclusion is that as the particle size decreased, the tensile strength of the biocomposites slightly increased because of good particle dispersion in the matrix polymer, although the impact strength decreased. Marek Kociszewski (2007) investigated the Effect of industrial wood particle size on mechanical properties of wood-polyvinyl chloride (PVC) composites. They studied the effect of particle size (0.25-0.5, 0.5-1, 1-2, and 2-4 mm) and the effect of cross-section size of composite pieces made by an injection molding method on the mechanical properties of the composites. It was concluded that the small size particles used for manufacturing a face particleboard layers provide better WPC mechanical properties than large size particles. Furthermore, the mechanical properties of WPCs with particles having a larger cross section area are in general lower.

Though many researchers have reported favorable effects of fine wood particles on composite properties, the opposite effects of wood particle size were observed in some other studies. Ichazo et al. (2006) observed the influence of two different wood particle size ranges (250–300  $\mu\text{m}$ ) and (300–425  $\mu\text{m}$ ) on the properties of the composites. They found that the particle size range of 300–425  $\mu\text{m}$  was found to offer the best overall balance of mechanical and dynamic properties, as well as a higher degree of cross-linking density of particles.

### **1.3 Durability of wood plastic composites**

WPCs are expensive compared to solid wood options but they do not require painting or other finishes, nor will they warp or rot like wood. Furthermore, WPCs are often advertised as a durable building product that resists cracking and warping. However, WPCs are not maintenance free and they can be degraded in outdoor environments. The wood in the WPCs can still be attacked by rot and mold fungi, and sunlight can discolor and break down



the plastic component. Many researchers are working on understanding the fundamental mechanisms of degradation and on ways to improve WPCs (Roger M. Rowell. 2004).

### **Moisture and Decay**

Moisture is required for biological decay of wood. For solid wood, moisture alone reduces the strength and stiffness and moisture content is intimately related to appearance and dimensions of wood productions. In contrast, the polymers in WPC may protect wood from moisture because they are hydrophobic. Generally, the overall uptake of moisture in WPC is slow compared to solid wood, and the amount of moisture absorbed by WPCs can vary widely as a result of influences of the wood flour content, wood particle size, processing methods, and additives. Anke Schirp and Michael P. Wolcott (2004) studied the contributions of moisture and wood decay fungi to WPC damage. They compared changes in flexural strength (MOR), modulus (MOE), and weight of two extruded wood-polyethylene composite (WPC) formulations incubated with wood decay fungi. Their results indicate that the stiffness of WPC was reduced due to moisture absorption but not due to incubation with decay fungi. S. -H. Huang et al (2006) studied the influence of moisture on the mechanical properties of wood polymer composites. They found that the presence of moisture precipitated a reduction in the compressive strength of the composite and the properties of composites degrade more rapidly in samples containing more than three percent water.

There are four basic growth requirements of fungi: food (wood, which contains hemicellulose, cellulose, and lignin), moisture (above the fiber saturation point; about 30% moisture content), proper temperature [10-35 °C, optimum: 24-32 °C], and oxygen (from the air). Since WPCs contains wood fiber or flour, they can be attacked by fungi like solid wood. Extensive research has been conducted to examine the effects of fungal attack on WPCs. Morris and Cooper (1998) proved the presence of fungal decay and discoloration in WPC decking material in service. Anke Schirp and Michael P. Wolcott (2004) found that WPCs can be designed to provide high fungal durability by controlling the formulation composition. WPCs exposed to weathering by ultraviolet light, oxidation, and rain water may experience color change as well as loss of mechanical properties. The color change affects the aesthetic quality, whereas the mechanical loss affects the performance. Johnson et al (1999) tested

visual and mechanical characteristics of the plastics after accelerated weathering (ultraviolet and humidity at elevated temperatures). They found that the wood particles are effective sensitizers and their incorporation into the polymer promotes and/or accelerates photodegradation of the polymer matrix. Thomas Lundin et al. (2004) studied the resistance of natural fiber-filled high-density polyethylene composite specimens to ultraviolet- (UV) and moisture-induced degradation. They observed that the flexural modulus and strength decreased significantly with increased exposure. Schauwecker et al. (2006) examined the physical and chemical changes of wood-plastic composites after 10 years in the field (stake and ground proximity) at a tropical site. It was concluded that WPC exposed both in soil and above/ground experienced microbial and physical damage as well as substantial chemical changes.

#### **1.4 Applications of WPCS**

Wood plastic composites (WPC) are promising and sustainable green materials to achieve durability without using toxic chemicals. Their most widespread use is in outdoor deck floors, but they are also used for railings, fences, landscaping timbers, cladding and siding, park benches, molding and trim, window and door frames, and indoor furniture (see Figure 1.3). The decking market is one of most important markets for WPCs. The decking market includes deck boards, railing systems (consisting of a top rail, balusters, bottom rail, and posts), and accessories, such as stairs and built-in benches. WPC decking was widely available and popular when it was first introduced. In general, WPC decking has a production cost of about 15% more than that of pressure-treated lumber, but requires a lower maintenance cost (Smith, P. 1999). According to one report, composite decking sales alone in North America in 2004 was \$670 million. U.S demand for decking (wood and WPC) in 2005 reached \$5.1 billion, or approximately 4.0 billion board feet, and is projected to grow to \$5.5 billion and 4.2 billion lineal feet in 2006. The market share of WPC decking grew by 22% in 2006 (Anatole et al. 2007). The majority of WPC decks, manufactured and sold today, are based on polyethylene (PE), polypropylene (PP), or polyvinyl chloride (PVC), Figure 1.4 shows an example of WPC decking.

Recently, WPCs have found extensive use in the automotive markets. In the US, recycling of automotive interior parts is still difficult because most of them are petrobased polymer materials with mixed composite structures (Chen et al., 2005). Research has demonstrated that the use of wood fibers for automotive composite applications has many advantages such as enhancing mechanical strength and acoustic performance, reducing material weight and fuel consumption, lower production costs, improved passenger safety and shatterproof performance under extreme temperature changes, and improved biodegradability for the



(a)



(b)



(c)



(d)

**Figure 1.3: Application of wood plastic composite: (a) bench, (b) garbage bin, (c) Flooring, (d) French**

(Source: Figure 1.3 (a) and (b) are from [www.china-wpc-product.com](http://www.china-wpc-product.com); Figure 1.3 (c) is from [www.bambayharbor.com](http://www.bambayharbor.com); Figure 1.3 (d) is from [www.yeskey.com](http://www.yeskey.com))



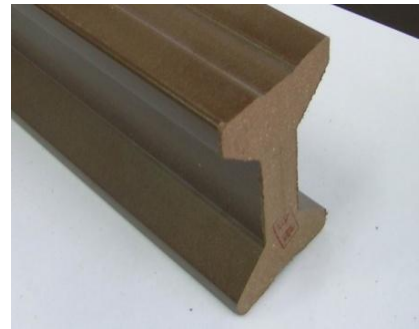
**Figure 1.4: WPC decking**

(Source: Figure 1.4 is from [www.china-wpc-product.com](http://www.china-wpc-product.com))

auto interior parts. A major market identified for the application of green WPCs, as replacement of fiber glass and steels, is for automotive components (Alireza Ashori. 2008).



**(a)**



**(b)**



**(c)**



**(d)**

**Figure 1.5: WPC products (a) WPC panels, (b) WPC Joist, (c) WPC pipe, (d) WPC siding**

(Source: Figure 1.5 (a) and (b) are from [www.yeskey.com](http://www.yeskey.com); Figure 1.5 (c) is from [www.ventmaster.com](http://www.ventmaster.com); Figure 1.5 (d) is from [www.tradew.com](http://www.tradew.com))

They are used as trim parts in dashboards, door panels, parcel shelves, seat cushions, backrests and cabin linings. Although many interior automotive parts can be made from WPCs, few exterior parts can only be made from plant fiber composites (Bismarck et al., 2006; Jacob and Thomas, in press). Automotive components made from WPCs are currently being used by many vehicle manufactures such as: Audi, Opel, Daimler-Chrysler, Fiat, Ford, Mercedes Benz, Peugeot, Renault, Volvo, VW, Volkswagen and BMW (Bismarck et al., 2006). Another rapidly growing application for WPCs is in extruded sections for residential building markets. WPCs are becoming common for replacement panels, flooring, joists, siding and pipe (see Figure 1.5).

### **1.5 Characterization of WPCs and Wood/Polymer Interface**

In general, an interface in composites is defined as an imaginary surface forming a common boundary between the phases (e.g., a wood particle and the surrounding polymer matrix). Many of the physical and mechanical properties of WPCs depend on the interaction between wood particles and the thermoplastic. Using coupling agent can improve this interaction property. Materials with strong interfaces show good composite action between the matrix and the fiber. In contrast, a weak interface would reduce the efficiency of stress transfer from the matrix to the fiber, which acts merely as a filler and as a result the strength and stiffness are lowered (Jacob et al. 2005).

In WPCs, the wood particles are hydrophilic, which is incompatible with hydrophobic thermoplastic polymers. This incompatibility between wood and the polymer matrix becomes a major problem for their interfacial properties, which greatly affects the mechanical properties of WPCs (Jiang and Kamdem 2004). A lot of research has been done to understand the nature of the interfacial characterization and several methods have been developed to measure the interfacial properties of fibers. For example, interfacial shear strength is an important factor which controls the toughness, mechanical properties, and inter-laminate shear strength of composite materials. The interfacial bonding can be evaluated by measuring the interfacial shear strength. Below are some micro-mechanical techniques used to obtain interfacial shear strength.

### **Single Fiber Pull-out Test**

The interfacial shear bond strength can be measured by single-fiber pull-out testing, which involves embedding one end of a single fiber in the matrix and pulling the fiber out of the matrix during the test (XULI FU et al. 1997). Research in the area of single fiber pull-out has considered the fracture mechanics and shear stresses of fiber-matrix failure and this model has been implemented to compare various fiber surface treatments and embedding matrices (Marshall, P. and Leonard, J. 1992). However, for WPCs, since the wood particles embedded in the polymer matrix are generally composed of large amount of fibers and have different geometrical features, the single fiber pull-out test is not suitable for the characterization of WPCs. Also the particles are too short for pull out tests

### **Micro-bead debond Test**

The micro-bead debond (MBD) is a recent modification of the single fiber pull-out technique and it is shown that there are some advantages in sample preparation of small contact area beads on small diameter fibers (Sauer B. B and Dipaolo. N. V 1995). In this test, a droplet of matrix is deposited onto the fiber and allowed to solidify. The top end of the fiber is attached to a load-sensing device, and the matrix is contacted by load points affixed to the crosshead of a load frame or another tensioning apparatus. When the load points are made to move downward, the interface experiences a shear stress that ultimately causes debonding of the fiber from the matrix. The interfacial shear strength can be calculated from the measured force. The Micro-debond test is a modification of the single fiber pull-out test, but it works best for fibers with very large aspect ratios. The aspect ratio of wood flour ranges from 3 to 5. Therefore this test is not well suitable for wood flour plastic composite characterization (Nicholas P. Cheremisinoff).

### **Single Fiber Fragmentation Test**

The single fiber fragmentation test is one of the most popular methods for evaluating the interfacial properties of fiber-matrix composites. The method has been used extensively (Kim and Nairn. 2002; Zhou et al.1999) to determine the bonding characteristics between fibers and matrices on the microscale. The single fiber fragmentation Test developed from

the early work of Kelly and Tyson (1965). In the test, each specimen consists of one fiber encapsulated in a polymer matrix. The specimen normally has a dog-bone shape. The specimen is then elongated along the fiber axis resulting in fiber breakage. This experiment is done under a light microscope so that the fragmentation process can be observed in-situ. The interfacial shear strength can be calculated by using the critical fragment length of the fiber and the stress needed to obtain this minimum length (Stefanie Feih and Karen Wonsyld 2004):

$$\tau = \frac{\sigma_f(l_c)d}{2l_c}$$

where  $\sigma_f$  is the fiber strength at the critical length,  $d$  is the fiber diameter and  $l_c$  is the critical fragment length of the fiber. The critical fragment length of the fiber normally is the minimum length of the fractured fiber fragments at the end of the test.

Because of the wood particles' geometrical feature (aspect ratio is much smaller compared to other fibers), this method cannot be used for wood plastic composites, either.

### **Numerical modeling method for fiber/matrix research**

Because common experimental methods such as the micro-bond test and single-fiber, pull-out test do not work well for studying properties of the fiber/matrix interface in WPCs, there is need for a new method. One alternative is to use numerical modeling of detailed experimental results. This idea is explored in this thesis. In brief, one would compare numerical modeling of strain fields around wood particle inclusions to experimental results for strain fields around an isolated wood-flour particle. The numerical modeling can model interfaces between the fiber and the matrix.

### **1.6 Introduction of Material Point Method (MPM)**

In this thesis, we varied properties of wood particle and matrix in numerical modeling to find best match of simulated strain fields around wood particles with experimental results. The numerical modeling will use the material point method (MPM).

The Material Point Method (MPM) is a particle-based numerical method. Like the finite element method (FEM), MPM is a numerical technique for finding approximate solutions to solid mechanics equations. In computational solid mechanics FEM (Johnson. 1987) has been

very successfully applied to a wide range of problems with good results. MPM is an alternative that has some advantages for discretizing of complex materials like WPCs. The Material Point Method combines the strengths of Eulerian and Lagrangian descriptions of the material. In the Material Point method, the Lagrangian description is provided by discretizing each body by a collection of material points, and Euler's method are numerically used in a background mesh to solve the partial differential equations (PDE). Information carried by the material points is projected onto the background mesh where equations of motion are solved. The mesh solution is then used to update the material points (Bardenhagen et al. 2000).

Former research clarified that a weak formulation of the MPM algorithm for solid mechanics is given and the method is framed in terms of finite elements (Sulsky et al.1994.1995). The momentum equation is:

$$\rho \frac{dv}{dt} = \nabla \cdot \sigma$$

where  $\rho$  is the mass density,  $v$  is the velocity, and  $\sigma$  is the stress tensor. It is solved in a Lagrangian frame on a finite element back ground mesh.

### **History and Application of MPM**

The Material Point Method (MPM) is an extension of the Particle-in-cell (PIC) Method, which was originally conceived to solve problems in fluid dynamics. PIC methods were already in use as early as 1955 (F.H. Harlow. 1955), and then developed by Harlow at Los Alamos National Laboratory in 1957 (Johnson. 1996).

The PIC method was used primarily in fluid dynamics, and it has also been applied to problems in solid dynamics and plasma physics. Fundamental aspects of PIC methods include the interpolation of information between a grid and particles, and precisely which solution variables are ascribed to the grid, and which to the particles. The general trend has been toward keeping more properties on particles (Bardenhagen et al. 2004). This trend has been continued in the development of MPM.

The Material Point Method was introduced by Sulsky, Chen, and Schreyer (1994), who reformulated the PIC method and develop the MPM for better simulations of penetration problems in solid dynamics. In 1998, Bardenhagen extended the original MPM to include



frictional contact. Nairn (2003) further extended MPM to include explicit cracks and crack propagation in 2003. Recently, MPM has been used in many fields such as fluid dynamics, plasma physics, magnetohydrodynamics, and multiphase applications. Furthermore, Coetzee (2004) used MPM to simulate high-shear granular flow, such as silo discharge, Beuth (2007) provides numerically stable analyses of large-deformation problems in Soil mechanics with the recent development of quasistatic methods. Bardenhagen and Kober (2004) generalized the development that gives rise to MPM and showed that MPM can be considered a subset of their “Generalized Interpolation Material Point” (GIMP) method. GIMP solved many issues caused by particles crossing background element boundaries.

### **1.7 Objectives**

Wood as an anisotropic material has complex structures. It is hard to model wood or WPCs with many numerical methods. Nairn (2004) used Material point method (MPM) to analyze realistic wood structures. MPM simulated details of wood anatomy and variations in structure within wood specimens. Edward Le (Thesis) used numerical MPM modeling to study mechanics of oriented strand board. He used MPM to calculate the mechanical properties of OSB as a function of realistic strand undulation geometries and of the properties of the glue lines.

The purpose of this thesis was to combine imaging tools with MPM numerical modeling methods for an integrated characterization of bio-based reinforcements and their composites. The imaging tool used is the Digital Image Correlation (DIC) method, which is an optical method that employs tracking & image registration techniques for accurate 2D and 3D measurements of changes in images ([http://en.wikipedia.org/wiki/Digital\\_image\\_correlation](http://en.wikipedia.org/wiki/Digital_image_correlation)). It can be used to measure deformation and strain on the surface of WPCs. The numerical modeling method used here is the MPM method. These two methods were applied to copper/polymer composite and to WPCs.

In accomplishing this goal, the following specific objectives were met:

- (1) Measured full-field strain using Digital Image Correlation (DIC) on model WPCs  
(Collaboration with Matthew Schwarzkopf and Lech Muszynski)

- (2) Modeling of the wood-based composite: Simulated same structure of sample WPCs using the Material Point Method (MPM). The analyzed area was a small area around an isolated wood particle, using both 2D and 3D MPM models.
- (3) Qualitative analysis – compared strain fields in DIC and MPM results. The whole experimental area in DIC results was used to compare with MPM results, Matlab software was used as a tool to visualize strain field results in DIC and MPM. Strain fields in the fiber area and stress concentration areas were investigated.
- (4) Quantitative error analysis – compared calculated strains (by MPM) to measured strains (by DIC) in the small strain field around the fiber. Used Matlab to extract strain data from DIC and MPM results. These data were compared using a deviation error method.
- (5) Find the best match to evaluate particle and interface properties – both visual analysis and quantitative error analysis results were used to evaluate particle and interface properties of sample WPCs.

### **1.8 Outline of thesis**

This thesis contains 7 chapters. Chapter 1 is a general introduction to this thesis in which development of history of WPC, development of MPM, and objectives are presented. In chapter 2, the results of an MPM resolution study was used to guide subsequent modeling. In chapter 3, an interface study was applied to WPC by a MPM model. In chapter 4, a copper wire validation study is described containing both qualitative and quantitative comparisons. In chapter 5, we used wood particles instead of copper wire to do qualitative comparisons. Chapter 6 has quantitative error comparisons between DIC and MPM for WPC specimens. Chapter 7 is general summary of the thesis. The appendix lists the Matlab codes for importing MPM results and DIC results to enable qualitative and quantitative analyses of the results.

## CHAPTER 2: MATERIAL POINT METHOD (MPM) RESOLUTION STUDY

### 2.1 Introduction

The Material Point Method (MPM) is similar to Finite element method (FEM), but it is a particle –based method. They share one essential characteristic: mesh discretization of a continuous domain into a set of discrete elements. In MPM simulations, domains are divided into a regular grid of elements of equal size. The object being simulated is then divided into particles on top of the grid. All simulation here used up to four particles per background grid element for 2D or 8 particles for 3D. These choices for number of particles per element follow prior experience in MPM research. Some prior worked used 1 particle per cell, but most have settled on 4 (for 2D) or 8 (for 3D). The reason 4 or 8 are sufficient and there is no benefit to using more is likely that the element shape functions are linear in each direction; two particles per direction is therefore sufficient. The process for 2D is illustrated in Figure 2.1. The solid line is an outline of the body analyzed. The black dots are material points within the boundary with up to four particles per cell. The dashed lines here

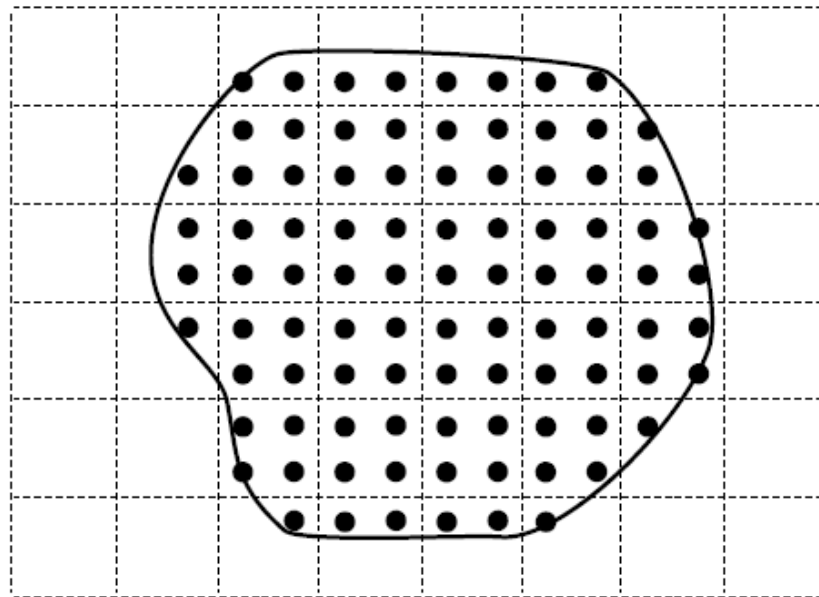


Figure 2.1: A schematic view of a two-dimensional MPM calculation

show the regular, background grid.

This thesis simulated a composite material by using the MPM method. Because composites have complex structure, one cannot simulate it with very low element resolution. Thus we needed to know how many particles are required to resolve phases. Simulations in this chapter were for a simple copper fiber embedded in a polyethylene matrix. We varied size of elements and thus varied number of particles across the embedded fiber. Next we checked output of MPM simulations for convergence and the resulting resolution and mesh size would be a guide for the future simulations.

## 2.2 Material and Method

This simulation was for copper wire embedded in polyethylene matrix. Because we focused on copper inclusion and polymer matrix is less important in the study, polyethylene was assumed to be as Von Mises plastic with modulus 450MPa, density  $1 \text{ kg/m}^3$ , and Poisson's ratio 0.33. The copper wire was set as linear elastic with modulus 120GPa, density  $8.94 \text{ kg/m}^3$ , and Poisson's ratio 0.34. Copper wire was modeled with its actual structure as recorded in a micrograph (Figure 2.2a).

The simulation includes a couple of steps. First is digitizing an image of the inclusion into a 2D MPM simulation. Figure 2.2a shows a micrograph for part of copper/polymer composite surface. The resolution of the image (Figure 2.2a), as obtained, was  $909 \times 646$  pixels and it images an area of  $2.25 \times 1.6 \text{ mm}$ . Because there are too many speckles around the copper wire in Figure 2.2a, which is hard to segment by MPM code, it was necessary to convert the

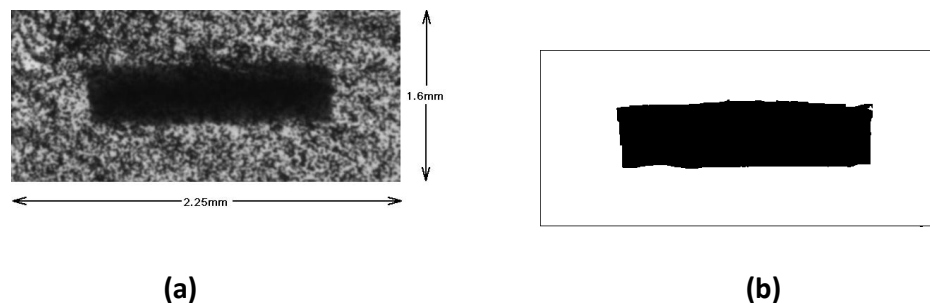


**Figure 2.2: Visualization of specimen surface and converted image. a. micrograph of copper/polymer composite surface. b. converted 256 level grayscale (black and white) bitmap image**

original image to a simpler one. Here we used “ImageJ” program to treat Figure 2.2a. First, we drew a contour line around the inclusion. Next, copper and polymer parts were filled with color. For the image in Figure 2.2b, polymer material was identified with intensity 255 (or white within a gray scale from 0 for black to 255 for white) and copper wire was identified with intensity 0 (black).

For simulations, an MPM background mesh was defined with any number of regular, quadrilateral elements covering an area greater than or equal to the image area. Our 2D MPM code divided the object into particles on top of the background grid (Nairn J.A 2005) based on gray scale colors in a BMP image file. The next step was to vary the number of particles until convergence. In order to obtain suitable MPM element resolution, the size of the elements was varied from small to large, thus the number of elements and particles in the entire model increased gradually. All convergence studies were done in 2D simulations. Figure 2.3 shows example of different elements sizes and particles number in the same area. The size of sample area is  $0.05 \times 0.05$  mm. Figure 2.3a has element size the same as area size and four particles; Figure 2.3b has element size  $0.025 \times 0.025$ mm and  $4 \times 4 = 16$  particles; Figure 2.3c has element size  $0.0125 \times 0.0125$ mm and  $4 \times 16 = 64$  particles; Figure 2.3d has element size  $0.00625 \times 0.00625$ mm and  $4 \times 64 = 256$  particles.

The results for global stress and global strain energy with time were plotted to find convergence. Here global means average stress over all particles or total strain energy.

The MPM simulation for copper wire specimens at the four different resolutions in Figure 2.3 are shown in Figure 2.4. Because the size of the image in Figure 2.2 is  $2.25 \times 1.6$ mm and

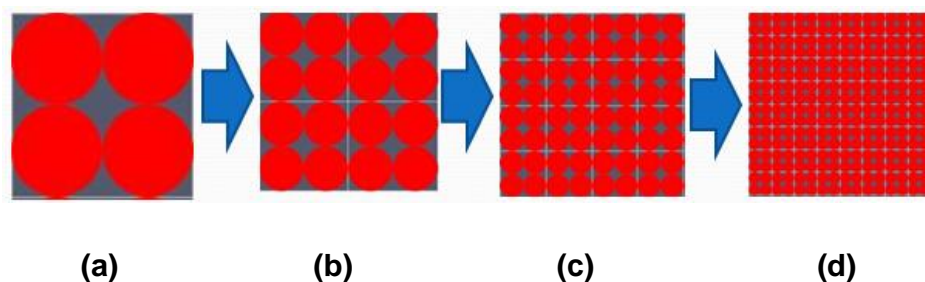


**Figure 2.3: Four different element sizes, from left to right are 0.05 by 0.05mm, 0.025 by 0.025mm, 0.0125 by 0.0125mm, and 0.00625 by 0.00625mm.**

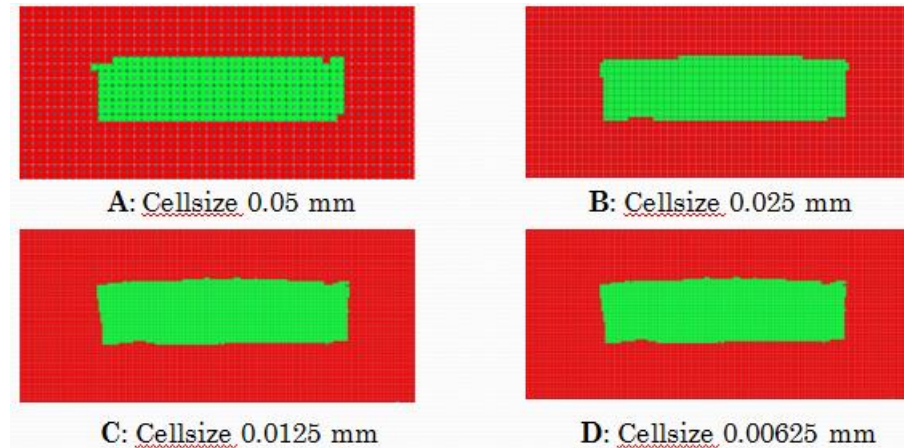


**Figure 2.4: Different resolution on Copper-PE Composite. A has cellsize 0.05 by 0.05mm, B has cellsize 0.025 by 0.025mm, C has cellsize 0.0125 by 0.0125mm, and D has cellsize 0.00625 by 0.00625mm.**

the size of copper fiber in the image is about  $1.702 \times 0.396$  mm. Figure 2.4a has  $90 \times 64 = 5760$  particles and provide  $68 \times 16 = 1088$  particles for copper; Figure 2.4b has  $180 \times 128 = 23040$  particles and provide  $136 \times 32 = 4352$  particles for copper; Figure 2.4c has  $360 \times 156 = 56160$  particles and provide  $272 \times 64 = 17408$  particles for copper; Figure 2.4d has  $720 \times 312 = 224640$  particles and provide  $544 \times 128 = 69632$  particles for copper. When you consider the width of the fiber, these meshes corresponded to 16, 32, 64, and 128 particles within the fiber across the thinner width dimension of the fiber. It is this number of particles relative to particle size that is more important for resolving phases than the absolute element size.

As seen in Figure 2.4, the one with large element size (A) has rough digitization of the interface between copper and polymer. In contrast, C and D are smoother on the interface because of higher MPM resolution and smaller elements. Higher resolution represents the geometry best, but one cannot simply pick highest resolution for simulations because higher resolution leads to longer computational time, which means both accuracy and experimental periods need to be considered. Because this is 2D simulation, each time the cell size is cut in half, the calculation time goes up 8 times. The number of the particle goes up 4 times and the number of time steps required doubles because the time step must be cut in half for dynamic convergence. The rule for dynamic convergence is that the time step

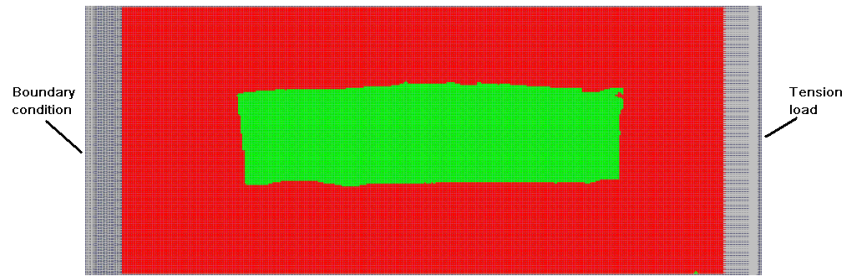


**Figure 2.5: Tension experiment for 2D MPM model, the red part is polymer, green part is copper, and arrow represents applied load**

must be less than the time it takes a stress wave to cross one element. Thus if the element is made smaller while the material is the same, the time step has to be made smaller too.

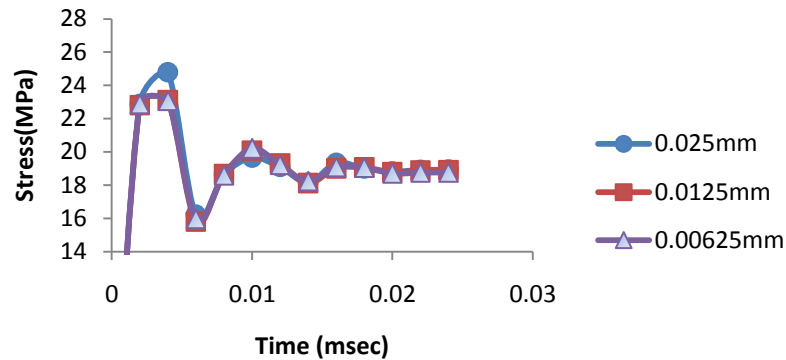
Tension experiments in the MPM simulations are illustrated in Figure 2.5. To monitor axial stress, a zero-displacement boundary condition was set on the left edge. The right side of the specimen was drawn by a tension load. The constant load was  $F = 8.487$  (N).

Here  $F$  is loading force at the one edge of sample in Newtons (N). The thickness of the model was set as 0.75mm. Moreover, a “damping” property was set in the MPM code to allow stress and kinetic energy damping out after vibrations. All calculations were done using two dimensional, explicit MPM code.

### **2.3 Results and discussion**

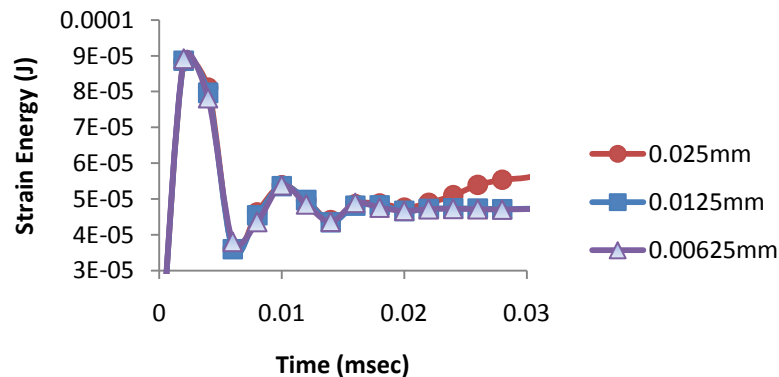
First, we needed to select an appropriate damping parameter to avoid vibrations caused by application of load at time zero. The goal was to damp to a static result by using a kinetic energy “thermostat” (see NairnMPM). The “thermostat” is controlled by a feedback damping gain factor in units of  $1/mm^2$ . Figure 2.6 shows global stress change with time for element size  $0.0125 \times 0.0125mm$ . Squares indicate results without damping; triangles indicate results with “feedback damping = 1000 ( $1/mm^2$ )”, and circles indicate results with

### Time-Stress plot



(a)

### Time-Strain Energy plot



(b)

**Figure 2.7: (a) Time-Stress plot (b) Time-Strain Energy plot. Circle indicates elements size 0.25 by 0.25mm, square indicates elements size 0.0125 by 0.0125mm, and triangle indicates elements size 0.00625 by 0.00625mm**



“feedback damping =  $5000 (1/mm^2)$ ”. One can observe that square line has large oscillation compared to triangle and circle line. Therefore we needed “feedback damping” to avoid dynamic oscillation. As Figure 2.6 shows, the circle line has less vibration than triangle line and became straight after 0.02 msec. Therefore, we used “feedback damping =  $5000(1/mm^2)$ ” in this chapter and took it as a guide for later studies. Figure 2.7 shows global stress and strain energy change with time for three type element size. The reason element size  $0.5 \times 0.5mm$  is not shown here is because the visual MPM result (see Figure 2.4a) shows this size is too large to do simulation (the number of inclusion particles across the thinner dimension is too low). Based on damping study results, here we only took the front part from 0 to 0.03 ms to do analysis. The large vibration of stress and strain energy in Figure 2.7a and b before 0.01ms is due to instant load application. In Figures 2.7a and b, both stress and strain energy became stable after 0.02ms (showing straight lines on the plot). The curves for square line (element size  $0.0125mm \times 0.0125mm$ ) and triangle line (element size  $0.00625mm \times 0.00625mm$ ) look similar on both Figures 2.7 a and b. In other works this calculation converged for  $0.0125mm \times 0.0125mm$  elements. The results of  $0.025mm \times 0.025mm$  elements were slightly different, but may be satisfactory. The computational time of element size  $0.00625mm \times 0.00625mm$  is much longer, but normally not needed. In this experiment, the MPM resolution of element size  $0.0125mm \times 0.0125mm$  is high enough to get appropriate accuracy.

## 2.4 Conclusion

First of all, damping property has effect on the accuracy of MPM simulation results, finding appropriate damping value is important. Here we used “feedback damping =  $5000(1/mm^2)$ ” is enough for this problem and this damping would be a guide for future modeling.

Furthermore, for simulating composites, the element resolution of MPM has crucial effect on accuracy of simulation results. Higher MPM resolution (small element size) can get more accurate result but also takes more computational time. This study showed samples with element size  $0.0125mm \times 0.0125mm$  or smaller are good enough for accuracy. This mesh had 64 particles across the thinner dimension of the copper wire. Therefore, all subsequent

simulation in this thesis used this element resolution as a guide to obtaining results as quick as possible without harming the accuracy of the simulations.

## CHAPTER 3: VIRTUAL INTERFACE STUDY

### 3.1 Introduction

There are two roles for Interfacial properties, one is “stiffness” and the other is “strength”. Both of these interfacial properties are important for composite mechanical properties. The “strength” property is to hold elements of the composite together, and the “stiffness” is used as a generic term for stress transfer between components of a composite. Prior to interfacial damage, the role of the interface is solely characterized by its stiffness properties while its strength properties are irrelevant.

This chapter describes numerical modeling on the effect of interfacial stiffness properties and uses the concept of an “imperfect” interface to lump complexities of a three dimensional interphase zone into a two dimensional interface model. This study looked at a wood particle inclusion in an elastic matrix and at the effect of interfacial properties on the strain field around the particle. The interface was modeled as an imperfect interface which is equivalent to the effect of a thin elastic interphase as derived by a Taylor expansion method in terms of interface displacement and traction jumps (Hashin. Z 2002). The matrix was set as an elastic material and the wood particle was set as an anisotropic material. All simulations were in 2D. In this chapter, the interface property was varied and its effect on effective modulus of the specimen was observed. In addition, we looked at 2D MPM results for effect of interface on the strain field. These virtual experiments showed how to put interfaces into the model and showed the effects of interfacial properties on strains. Because calculations in later chapters are 3D and the current code cannot do 3D interfaces, interface work here was limited to these 2D virtual experiments.

### 3.2 Materials and Method

Interfaces in composite are complex three dimensional structures with a transition in properties between two bonded materials. Modeling such structures is difficult and depends on many unknown properties. In order to reduce the unknown properties to a few measurable interface parameters, one approach is to replace the 3D structure with a 2D

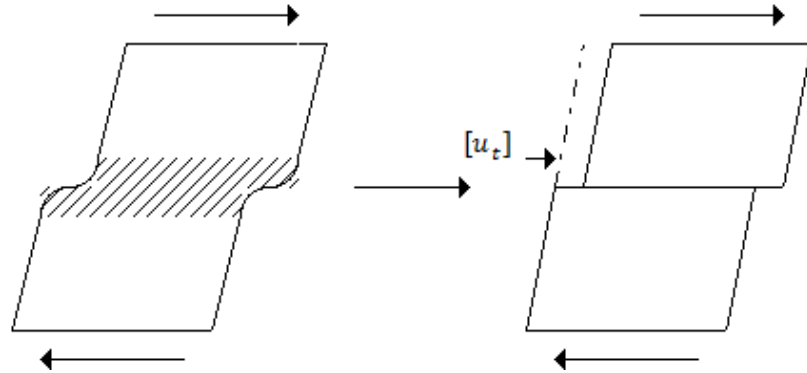


**Figure 3.1: View for three dimensional interphase and two dimensional interface**

interface having two properties. Such a method has been proposed by Hashin (2002) and is illustrated in Figure 3.1.

In Figure 3.1, the left side shows a 3D interphase zone with a gradient in properties between two materials and complex shear deformations. The right side shows a simplified composite where macroscopic deformations are the same, but the interphase has been replaced by a 2D interface zone. The effect of the interface is reduced to an interfacial slippage by a displacement discontinuity  $[u_t]$ .

According to Hashin's imperfect interface theory, the displacement discontinuity magnitude should be a function of the traction vector in the direction of the discontinuity and of stiffness properties of the imperfect interface (Hashin 1990, 1991, 1992 and Martin 1992).

The simplest assumption is to assume the traction is proportional to displacement

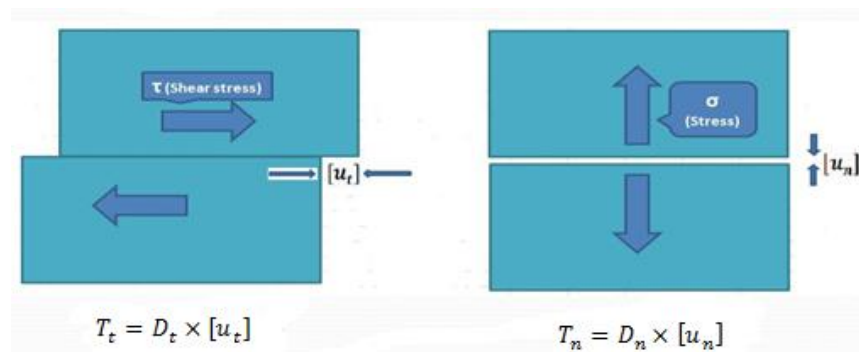


**Figure 3.2: A schematic view of shear sliding displacement and normal displacement,  $[u_n]$  and  $[u_t]$  are the normal and tangential discontinuities displacement;  $D_n$  and  $D_t$  are the interface parameters**

discontinuity as follows (Hashin 1990, 1991, 1992):

$$T_n = D_n \times [u_n] \quad T_t = D_t \times [u_t]$$

In Figure 3.2, for a 2D interface, the traction vector has been divided into components normal to the interface,  $T_n$ , and components parallel to the interface,  $T_t$  (Nairn J.A 2008), and  $[u_n]$  is the normal displacement discontinuity and  $[u_t]$  is the tangential displacement discontinuity;  $D_n$  and  $D_t$  are the interface parameters that reduce properties of the 3D interphase to two interface stiffness properties. A value of  $D_t$  or  $D_n = \infty$  means  $[u_t]$  or  $[u_n] = 0$  and is characterized as a “perfect interface”. A value of  $D_t$  or  $D_n = 0$  means  $T_n$  or  $T_t = 0$  and is characterized as a debonded interfaces. All values in between describe an “imperfect” interface.

In this study, we used the material point method (MPM) to model WPC with imperfect interfaces. The goal of this study is use this 2D interface model that describes stress transfer across the real 3D interface and to determine the effect of Interface parameters. Their effect on modulus and an overall strain fields was studied.

To model imperfect interfaces, we assumed a rectangular block for the wood particle and the tangential section is the interface as in Figure 3.3. In MPM 2D model, tangential section was

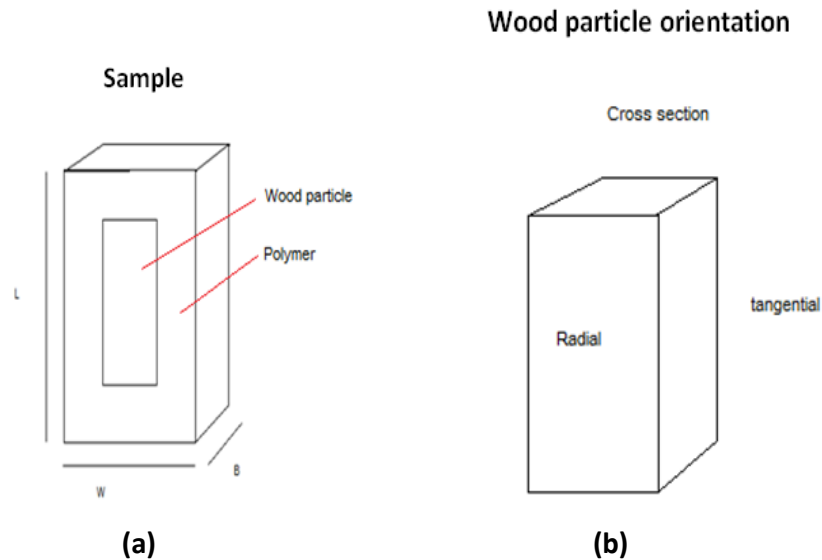


**Figure 3.3: Sample for numerical model. (a). left is 3D sample drawing. (b) right is simplified wood particle model**

Simulation image

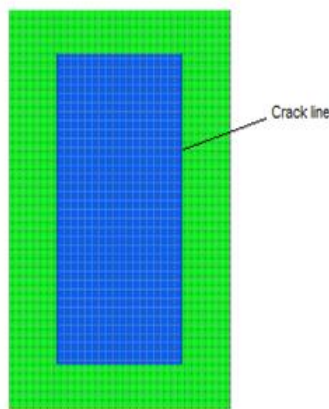


**Figure 3.4: 2D Material point method model for sample composite, the rectangular in the center of sample represents wood particle, material around it is polymer matrix, and there are two crack line(imperfect interface) between wood particle and polymer matrix.**

shown as crack line as in Figure 3.4. In the 2D model, the thickness of wood particle would be the same as the sample.

Figure 3.4 shows a visualization of the MPM model for Figure 3.3. Because it is a 2D model, Figure 3.4 shows the top surface of sample composite. According to prior experimental results (Chapter 2), the element size was set as  $0.025 \times 0.025\text{mm}$  and damping property was set to  $5000 \text{ 1/m}^2$ .

Table 3.1 shows sample size and particle size used in the MPM simulations. Because wood is

**Table 3.1: Sample and wood particle size**

	Width(mm)	Thickness(mm)	Length(mm)	Volume(mm <sup>3</sup> )
X-loading sample	1.6	0.19	2.25	0.684
Y-loading sample 1	1.6	0.19	2.25	0.684
Y-loading sample 2	2	0.19	3.05	1.159
Wood particle	0.9	0.19	1.75	0.299

**Table 3.2: Wood particle properties**

	Exx	Eyy	Ezz	Gxy	Gxz	Gyz
	(Mpa)	(Mpa)	(Mpa)	(Mpa)	(Mpa)	(Mpa)
Modulus	630	12600	860	983	88	806

anisotropic material, the modulus property of wood particle is shown in Table 3.2. The density of wood particle was  $0.5 \text{ kg/m}^3$ . Exx is normal modulus in longitudinal direction of the wood particle, Eyy is normal modulus in radial direction of the wood particle, and Ezz is normal modulus in tangential direction of the wood particle. Gxy, Gxz, and Gyz are shear moduli. The polymer was set as isotropic material with modulus 1200MPa, density  $1 \text{ kg/m}^3$ , and Poisson's ratio 0.33.

As shown in the Figure 3.5, to simulate interfacial opening in radial direction or sliding in longitudinal direction, a layer of rigid particles was inserted on the left edge and right edge or on the top edge and bottom edge, respectively. Next, the right side or top side of the specimen was drawn at a constant rate ( $0.28 \text{ m/s}$ ) as a rigid piston. Figure 3.5a is X loading model which primarily simulates radial opening. Figure 3.5b is Y loading model 1 and Figure 3.5c is Y loading model 2, both of which primarily simulate longitudinal sliding. The interface is shown as crack line between wood particles and the polymer matrix. There are two crack lines along y axis on the edge of particle in Figure 3.5a and b. In Figure 3.5c, we set four crack lines (two on tangential plane and two on cross section).

Two interface stiffness properties,  $D_n$  and  $D_t$ , were applied to loading models in Figure 3.5. These interfacial stiffness attributes can specify an imperfect interface for this crack (in which case it is not a crack but rather a bond line in the specimen). In order to find the effect of these interface stiffness properties, some experimental conditions were assumed. First,  $D_n$  was set to infinity, while  $D_t$  was varied to find effective modulus change in loading direction. Alternatively,  $D_t$  was set to infinity,  $D_n$  was varied to find effective modulus change in loading direction. When both  $D_n$  and  $D_t$  approach infinity, the interface approaches a perfect interface.

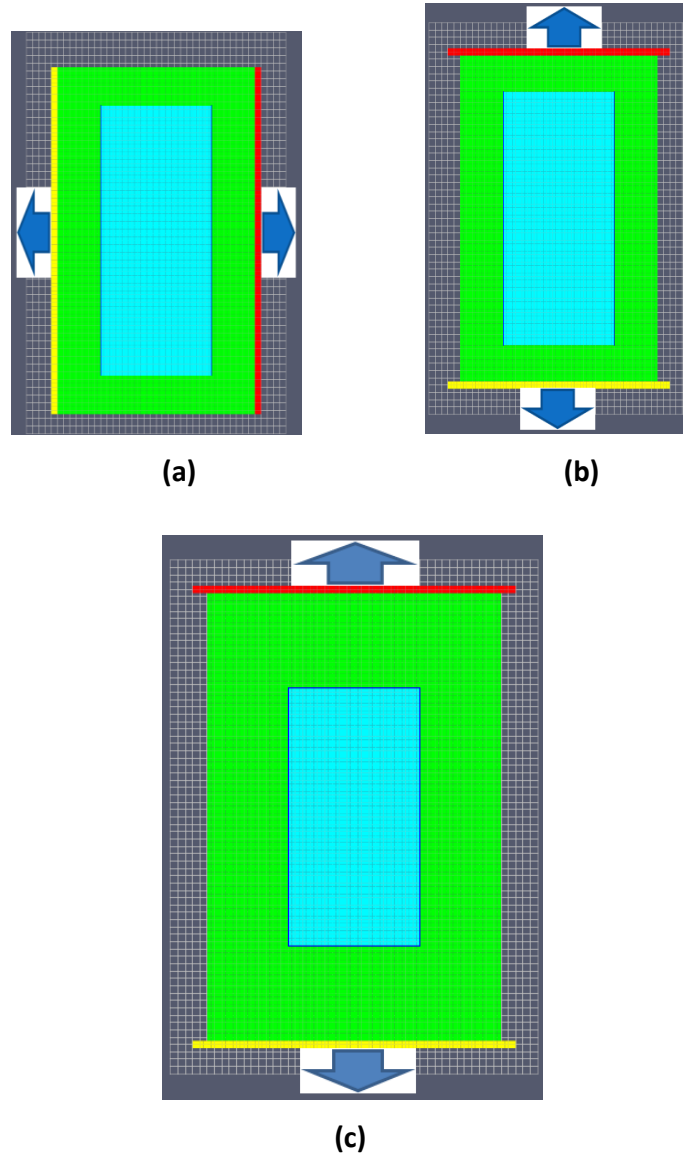


**Figure 3.5: radial opening (X loading) and tangential sliding (Y loading) on MPM simulation. (a). Radial opening with crack interface on tangential plane. (b). Longitudinal sliding with crack interface on tangential plane. (c). Longitudinal sliding with crack interface on tangential plane and cross section.**

In order to get effective modulus of the specimen, total energy was used in equation below:

$$U_t = \frac{1}{2} E_{ef} \varepsilon^2 V \rightarrow E_{ef} = \frac{KU_t}{t^2}$$

Where  $E_{ef}$  is effective modulus (MPa);  $\varepsilon$  is strain;  $t$  is loading time (here is 0.14 s);  $V$  is volume of sample;  $U_t$  is Total energy (J);  $K$  is a constant.

$$U_t = U_s + U_I$$



Here Total energy is comprised of two parts - Strain Energy (J) and Interface Energy (J). One can get Strain Energy  $U_s$  and Interface Energy  $U_I$  from MPM output. The constant K is:

$$K = \frac{2L}{WTv^2}$$

where W is sample width (here is 0.0016m for x-loading model and 0.002m for y-loading); L is sample length (here is 0.00225m for x-loading and 0.00305m for y-loading); T is sample thickness (here is 0.00019 m);  $v$  is loading rate (here is 0.28 m/s and therefore  $\varepsilon = vt/L$ )

### 3.3 Results and Discussion

#### 3.3.1 Radial opening (X direction loading)

For radial opening (X loading model), the relationship between effective modulus and parameters  $D_n$  and  $D_t$  are shown in Figures 3.6 and 3.7.

In X-loading model (Figures 3.6 and Figure 3.7), when  $D_n$  is close to 0 with  $D_t$  infinity, the effective modulus of the specimen is only 350MPa, and when  $D_n$  is above 20000, the effective modulus of the specimen is 890MPa. The effective modulus increased with increasing  $D_n$ , when another parameter approach to infinity. Eventually, effective modulus of the specimen would get close to the sample with perfect interface. When  $D_n = \infty$ , the

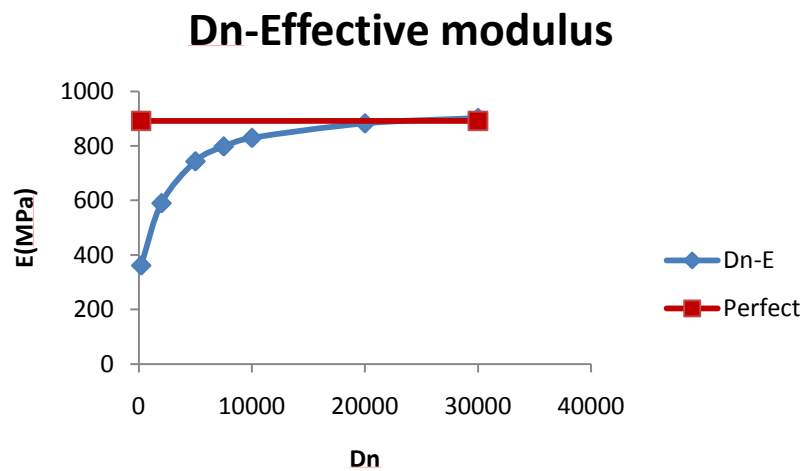
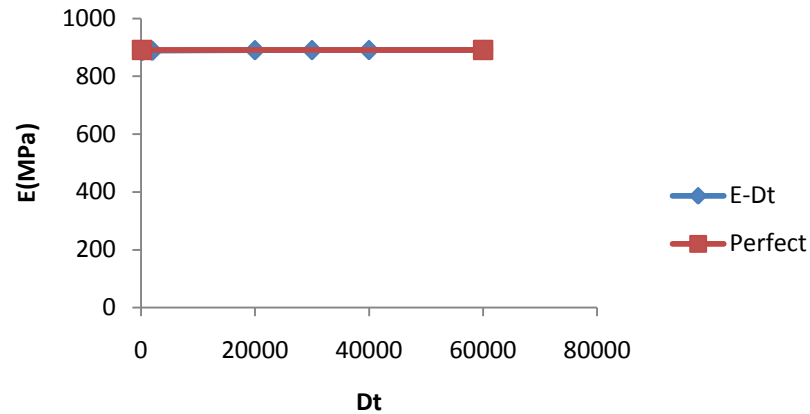


Figure 3.6: X-loading (radial opening), For  $D_t = \infty$ , vary  $D_n$



**Figure 3.7: X-loading (radial opening), For  $D_n = \infty$ , vary  $D_t$**

modulus is close to perfect for all value of  $D_t$ . In other words  $D_t$  has little effect of opening mode modulus.

### 3.3.2 Longitudinal sliding (Y direction loading)

For Y loading model, the relationship between effective modulus and parameter  $D_n$  and  $D_t$  is shown below. Figures 3.8 and 3.9 shows Y loading model with two crack interfaces on the tangential plane. There is no effect of  $D_n$  and  $D_t$  on effective modulus for this model because of the perfect interface at the fiber ends. Because the loading direction is parallel

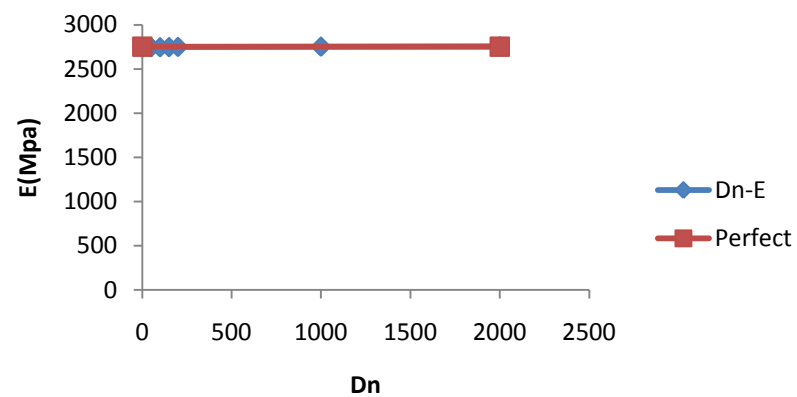


**Figure 3.8: Y-loading model 1 (longitudinal sliding), For  $= \infty$ , vary**

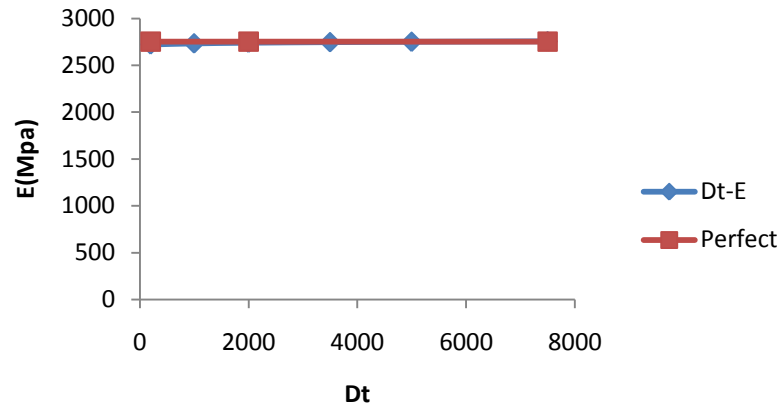


**Figure 3.10: Y-loading model 1 (longitudinal sliding). For  $D_n = \infty$ , vary  $D_t$**

to tangential section, the interface connection on the cross section of particle may control the stiffness. Therefore two debonded cracked interfaces were applied on the cross section of the wood particle to allow debonding and to see interface effects.

Figures 3.10 and 3.11 shows Y loading model with four crack lines. Here we only varied interface properties on tangential interface and kept them zero on cross section interface. Therefore, the side cracks were interfaces. The end cracks created debonds so no tensile

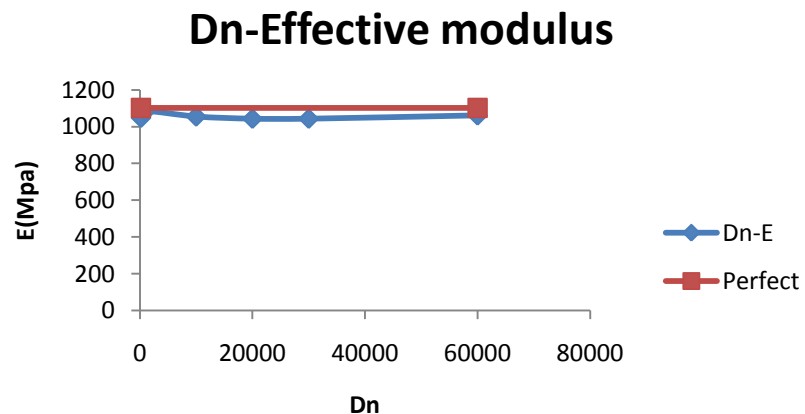


**Figure 3.9: Y-loading model 2 (longitudinal sliding). For  $D_t = \infty$ , vary  $D_n$**

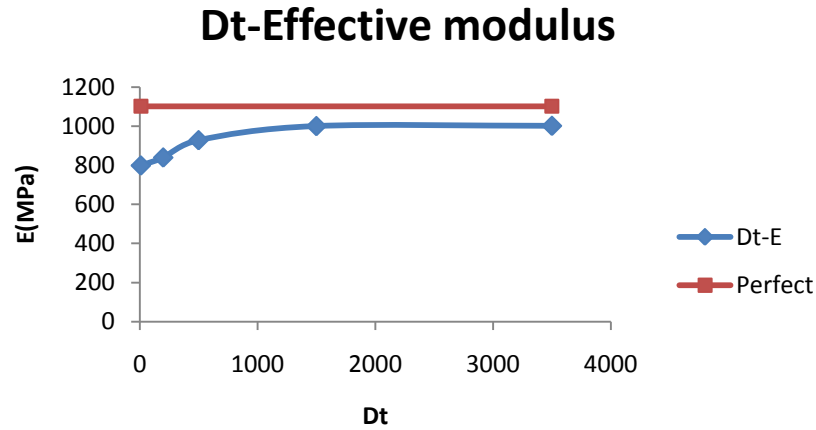


**Figure 3.11: Y-loading model 2 (longitudinal sliding), For  $D_n = \infty$ , vary  $D_t$**

stress transmits into the fiber end. For the interface on the tangential plane, as  $D_n$  and  $D_t$  approach zero, tractions approach zero and the interface is debonded. As  $D_n$  and  $D_t$  approach infinity, displacement discontinuities ( $[u_n]$  and  $[u_t]$ ) approach zero and the interface is perfect.

In Figure 3.11, the effective modulus increases as  $D_t$  increased with  $D_n$  infinity. Eventually, effective modulus of sample would get close to the sample with perfect interface. The reason for smaller effect of  $D_t$  (Figure 3.11, from 800 to 1100MPa compared to Figure 3.6) is because the new model has more matrix compared to fiber.

However, in Figure 3.10, varying  $D_n$  has few effects on the effective modulus of the sample. Therefore,  $D_t$  is more important on the effective modulus in longitudinal sliding (Y-loading) model.

### 3.4 Visual results from strain field

Figure 3.12 shows visual results of axial strain after 0.14ms loading with constant loading rate of 0.28m/s, Figure 3.12a has perfect interface on tangential surface with  $D_n = D_t = \infty$  and Figure 3.12b has  $D_t = \infty$  and  $D_n = 200$ . Figure 3.12a has relatively high strain in the wood particle area because wood particle is stiffer than polymer matrix. When interface

property was applied, stress concentration area around interface has very low strain (see Figure 3.12b), and this interface property also affects stress transfer between particle and polymer which was shown as low strain in particle area (see Figure 3.12b).

Figure 3.13 shows visual results of y direction strain after 0.14ms loading with constant load rate 0.28m/s, Figure 3.13a has perfect interface on tangential surface with  $D_n = D_t = \infty$ , Figure 3.13b has  $D_t = 1000$  and  $D_n = \infty$ , and Figure 3.13c has  $D_t = 10$  and  $D_n = \infty$ . Figure 3.13a has an elliptical strain contour around the particle, Figure 3.13b has smaller ellipse contour, and there are no stress concentration area and very low fiber strain in Figure 3.13c. The conclusion is the interface becomes stiffer when gradually increase  $D_t$  with  $D_n = \infty$ , when  $D_t$  is high enough, the visual results would be close to Figure 3.13a.

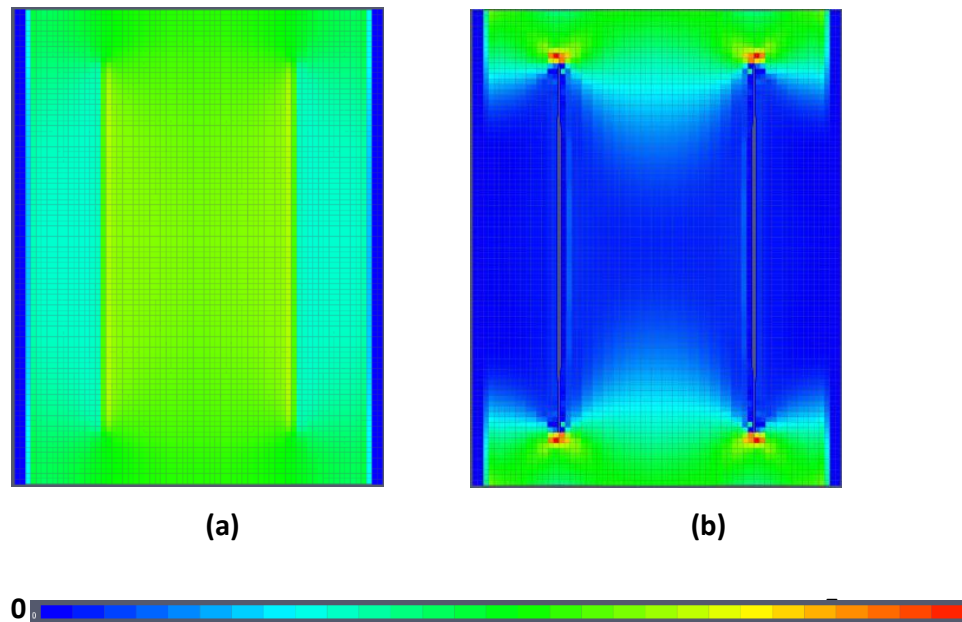


Figure 3.12: MPM Visual results of axial (x direction) strain for radial opening (X loading) model. (a). Perfect interface model. (b). Interfacial properties  $D_t = \infty$  and  $D_n = 200$

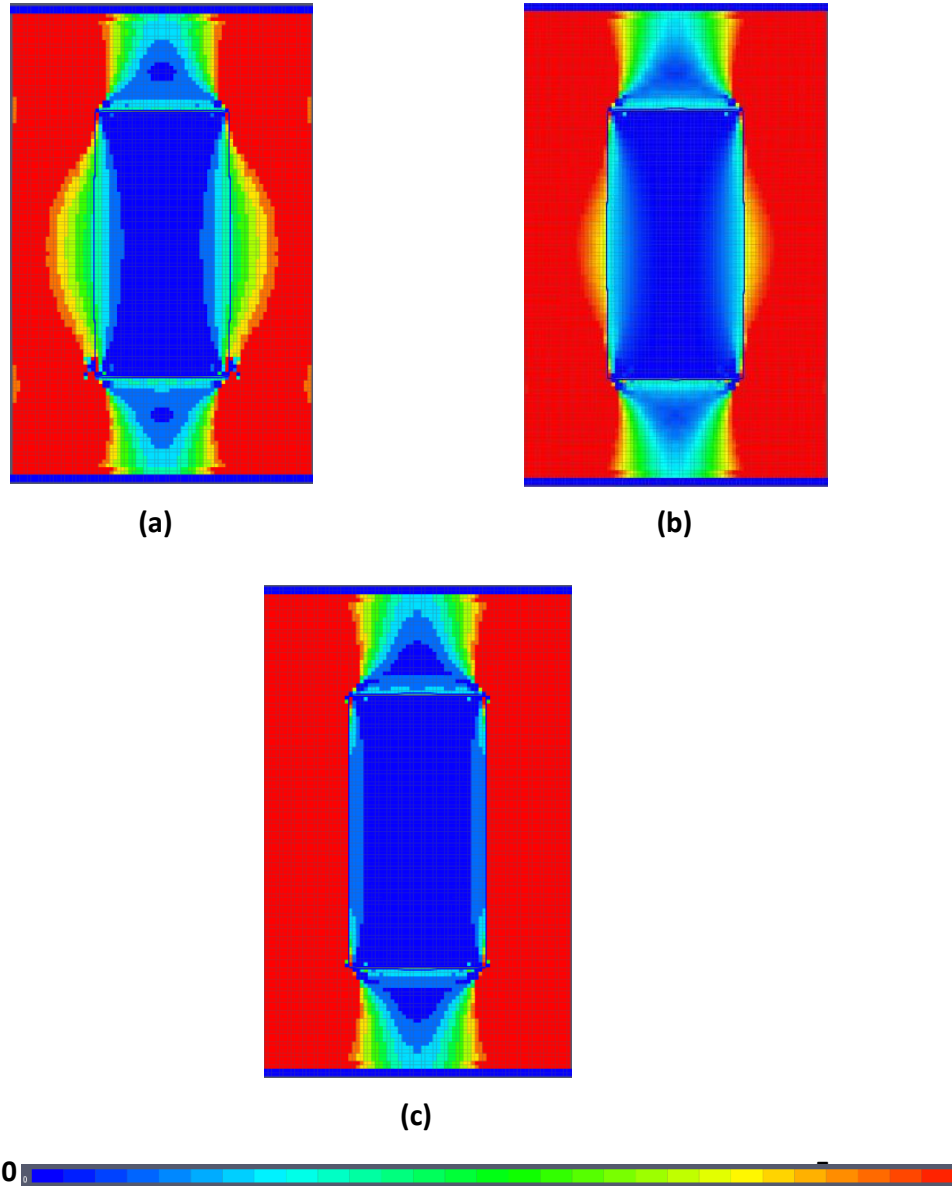


Figure 3.13: MPM Visual results of transverse (Y direction) strain for longitudinal sliding (Y loading) model 2 (four crack lines). (a). Interfacial properties  $D_n = D_t = \infty$ . (b). Interfacial properties  $D_t = 1000$  and  $D_n = \infty$ . (c). Interfacial properties  $D_t = 10$  and  $D_n = \infty$ .

### 3.5 Conclusion

From the results of interface experiment, we concluded that interface effects can be modeled in MPM 2D simulations. One can simulate different interface effects by defining  $D_n$  and  $D_t$  with appropriate values in MPM models. The result showed that  $D_t$  is more important on effective modulus in longitudinal sliding (Y-loading) model and  $D_n$  is more important in effective modulus in radial opening (X-loading) model. The visualization experiment result shows that interface stiffness affects stress transfer between phase in MPM 2D simulation, the visualized strain field has also been changed by varying  $D_n$  and  $D_t$  values.

## CHAPTER 4: COPPER WIRE VALIDATION STUDY

### 4.1 Introduction

One goal of this research is to deduce the properties of inclusions by numerical modeling of strain fields measured by DIC. In brief, we will vary the input mechanical properties of the inclusion until the calculated strain field best matches the experimental strain field. But, when the properties of the inclusion, such as wood particles are unknown, it is difficult to validate that the method works. In an attempt to validate the method, we did experiments and modeling on an inclusion with known properties. We choose copper wire which is isotropic and elastic material (at the loads used here) and available in a size similar to wood particles. It's modulus is 120GPa. The modulus is much greater than expected for wood particles, but it was hoped it could still validate the process.

The copper wire was embedded in a polyethylene matrix. The first simulations used 2D calculations (like those in Chapter 2). The results, however, did not agree with experiments. We therefore turned to 3D calculations, which worked better. Using 3D simulations, we did qualitative and quantitative comparisons between models and experiments for axial strain ( $\epsilon_{xx}$ ), transverse strain ( $\epsilon_{yy}$ ), and shear strain ( $\tau_{xy}$ ). For qualitative analysis, strain fields were plotted and compared by visual inspection. For quantitative analysis, experimental data were interpolated to MPM coordinates and least squares residuals were calculated between model and experiment over various regions.

### 4.2 Materials and methods

#### 4.2.1 Sample property and dimension

In this study, copper wire and polyethylene were used to make sample composites. Differential Image Correlation (DIC) was used for surface strain characterization of the polymer matrix composites with an embedded copper wire. The digital image correlation (DIC) method obtains the incremental displacement and strain field on the surface of a planar specimen by comparing a pair of digital images taken before and after the deformation (Su. C and Anand. L 2003). DIC images were collected along with average strain



vs. total strain curves. At selected applied loads, the DIC images were analyzed using Vic-2D 2009 (developed by Correlated Solutions) to determine experimental strain fields. In addition, conventional 2D microscopic techniques (regular light microscopy) were used to provide visual supporting information on the morphology of the copper fiber. The sample preparation and DIC experiments were done by Matthew J. Schwarzkopf.

In the experiments, the specimen width was 4.8mm, length was 29.3 mm, and thickness was 0.75mm. The measured copper wire length was 0.846mm and its diameter was 0.207mm. A load was applied to the specimen in the x direction at constant displacement rate of 0.5mm/s.

In the simulations, copper wire was set as linear elastic with modulus = 120GPa, density =  $8.94\text{kg/m}^3$ , and Poisson's ratio = 0.33. The copper wire was modeled with its actual structure as recorded in the microphotograph (see Figure 4.1). To determine the polymer properties, we simulated a pure polymer cube in an MPM 2D model with tension load applied to one edge of the sample. The output of stress-strain relationship for this simulation was plotted and then compared with DIC stress-strain plot for copper wire sample, when the simulation results and DIC experimental results got close, the property of the polymer used in the simulations was selected for copper wire validation study.

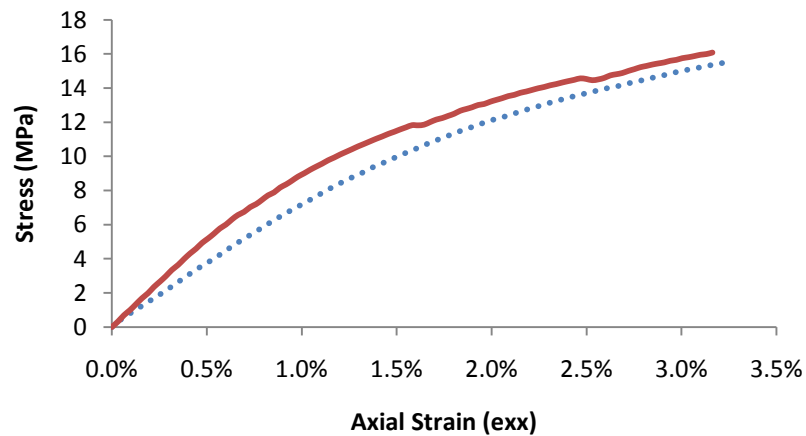


**Figure 4.1: Stress-strain relationship for copper wire experiment (DIC) and pure polymer MPM 2D simulation, solid line represents pure polymer MPM 2D simulation results and broken line represents copper wire experiment results.**

Figure 4.1 shows stress-strain relationship for copper wire experiment (DIC) and pure polymer MPM 2D simulation. Broken line indicates the copper wire experimental results. The solid line indicates the pure polymer MPM 2D simulation results. When polymer property was set as above, solid line and broken line were close so that these polymer properties were assumed to be close to the polyethylene properties used in the experiment. The experiment varied from one to another, an overall average was used in MPM simulations.

The fit was obtained using a Von Mises plastic with modulus = 450MPa, density = 1 kg/m<sup>3</sup>, and Poisson's ratio = 0.33. The modulus was determined from initial slope of experimental stress-strain data. For nonlinear response the yield stress was given by hardening law:

$$\sigma_{Y0} = \sigma_Y(1 + K\alpha)^n$$

where  $\sigma_{Y0}$  is the initial yield stress,  $K$  and  $n$  are dimensionless hardening parameters, and  $\alpha$  is an internal variable that tracks cumulative, equivalent plastic strain. Here the initial yield stress was 6.75MPa. “K” and “n” for the fit were  $K = 5300$  and  $n = 0.2$ , which were estimated by comparison of several stress strain curves by experiment to MPM calculations with the pure matrix.

#### 4.2.2 2D modeling

The first simulations used 2D MPM calculations. This section explains how MPM simulated the sample structure in a 2D model and compares x direction strain of MPM simulation

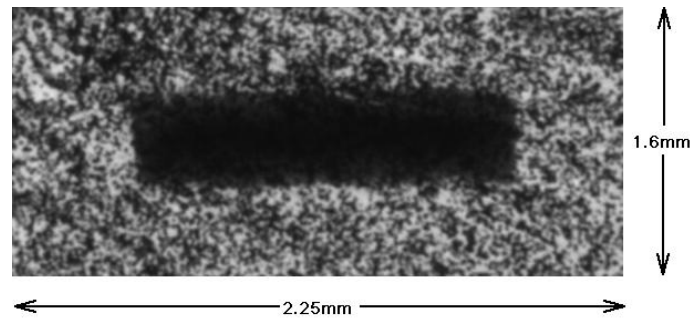


**Figure 4.2: Visualization of a part of specimen surface. This micrograph images area of 2.25 × 1.6 mm.**

results to experimental results. The compared strain results showed that 2D MPM simulation is not sufficient and therefore 3D MPM simulations were used instead.

For MPM 2D simulations, only a part of specimen was modeled. The width of MPM model was 1.6mm, the length was 2.25mm, and the thickness was 0.75mm (see Figure 4.2). The copper wire was modeled using its actual structure as recorded in the DIC image (Figure 4.2).

Figure 4.3a shows a micrograph of part of a copper/polymer composite surface. Figure 4.3a shows original image of the sample surface. Because there are too many speckles around copper wire, which is hard to identify by MPM simulation, it was necessary to convert the original image to a simple mask image. Here we used “ImageJ” program to process Figure 4.3a. The first step was to draw a contour line around inclusion. The next step was to fill copper part and polymer part with colors. For the image in Figure 4.3b, the polymer material was identified with intensity 255 (white within a gray scale from 0 for black to 255 for white) and copper wire was identified with intensity 0.

The mask image was converted to BMP file and used for 2D MPM simulations. The process to import the BMP image (Figure 4.3b) into MPM was as follows: An MPM background mesh was defined with a number of regular, quadrilateral elements covering an area greater than the image area. Each element in the mesh was assigned to have four possible locations for material points each representing one quarter of the element volume. The 2D MPM code then maps the BMP image to the mesh and evaluates the intensity of the image corresponding to each potential material point location. Based on the average image intensity, each location was either assigned to have a material point representing copper

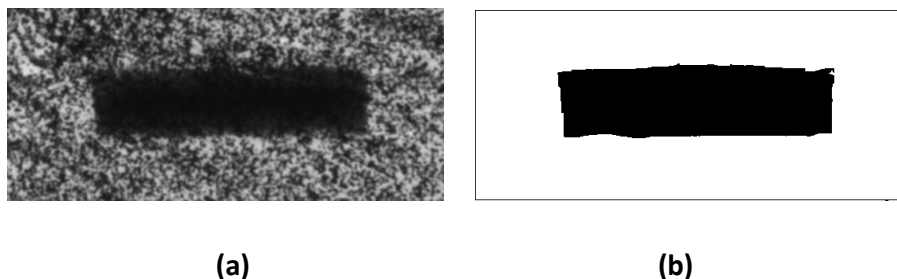


**Figure 4.3: Visualization of specimen surface and converted image. a. micrograph of copper composite. b. converted 256 level grayscale bitmap image**

wire material or representing polymer material. The resolution of the MPM discretization could be adjusted arbitrarily to vary accuracy for digitizing the image. For these copper wire samples, the MPM model used a background grid for the image of  $90 \times 64$  elements. This background grid provides for  $180 \times 128 = 5,760$  potential locations for particles. The element size was  $0.025\text{mm} \times 0.025\text{mm}$ . The image resolution was  $910 \times 647$  pixels, the size of pixels was  $0.00247(\text{mm}/\text{Pixels})$ .

A tension experiment in an MPM 2D simulation is illustrated in Figure 4.4. To monitor axial stress on the specimen, the left side of the specimen was restrained with zero-displacement boundary conditions. A tension load “F” was applied on the right edge of specimen. The loading function was:

$$\sigma = \frac{428.75 \times t}{b \times h};$$

$$F = \sigma \times b \times h = 428.25 \times t$$

where F is loading force at the one edge of sample with units of Newtons (N); t is loading time with units of millisecond (ms);  $\sigma$  is stress with units of MPa;  $h = 1.6\text{mm}$  is the analyzed width and  $b = 0.75\text{mm}$  is the specimen thickness.. All calculations were done using explicit MPM code. After loading, MPM would generate a series of simulation results at certain times. Here time step was  $0.002\text{msec}$ , which was determined automatically by MPM. Finally we compared global strain from MPM results at each step with global strain in DIC results

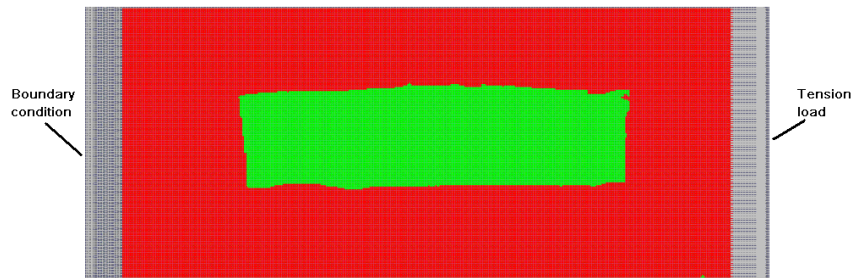
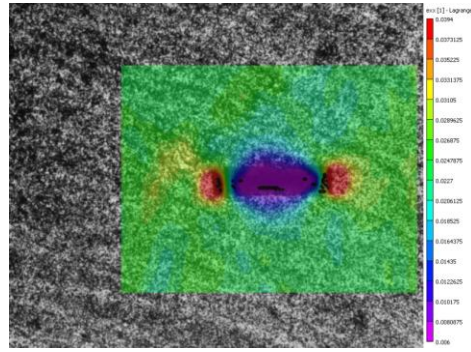
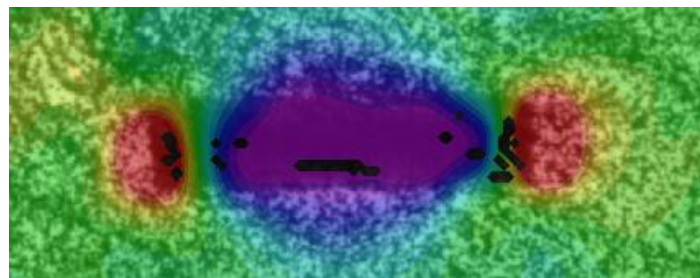


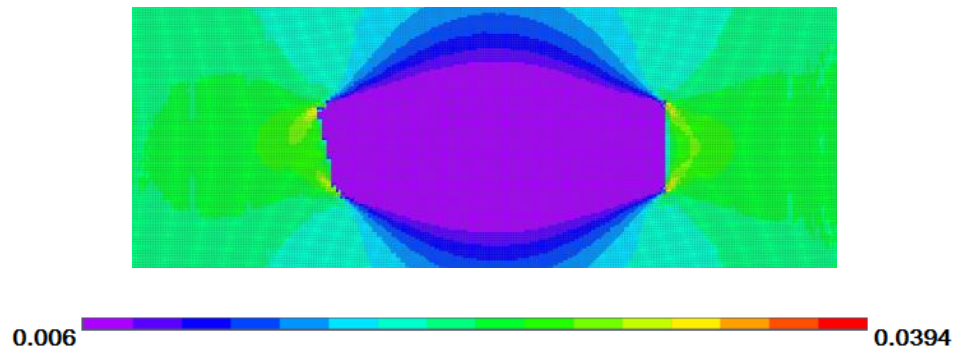
**Figure 4.4: Tension experiment on 2D MPM simulation, the red part is polymer, green part is copper wire, and arrow on the right represents applied load**



(a)



(b)



(c)

**Figure 4.5: Visual axial strain results. (a) DIC axial strain results for copper wire specimen. (b) Magnification of DIC results (c) MPM 2D simulation of axial strain result for copper wire sample.**

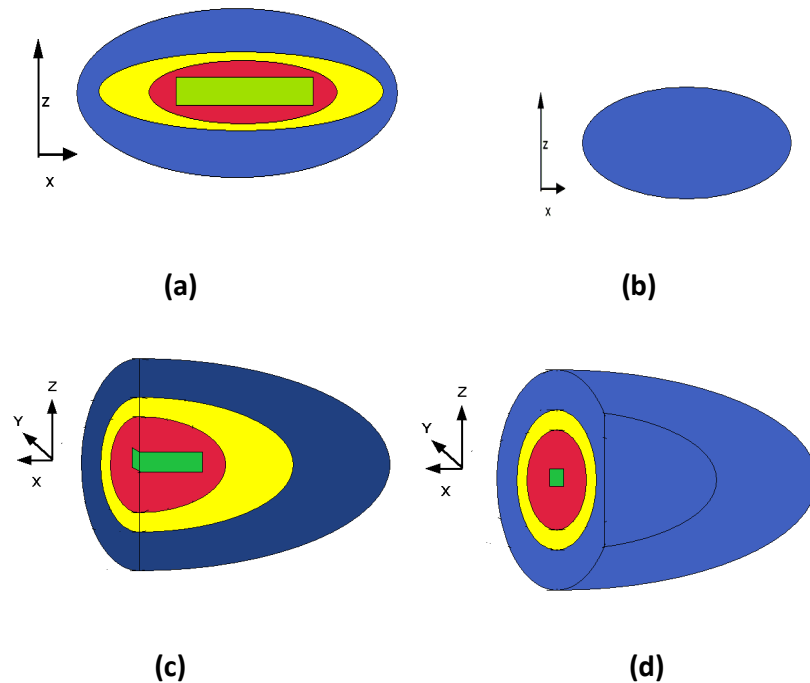
the closest one to MPM results was selected for qualitative comparisons.

Figure 4.5 shows axial ( $\varepsilon_{xx}$ ) strain in DIC results and in MPM 2D simulation results.

Comparing Figures 4.5b and c, the position of stress concentration area is different, and the

strain around the copper wire is also different. In 2D MPM simulation, the layer analyzed contains the copper wire but for DIC experiments the analyzed layer is on the surface of specimen, which is above the copper wire and may explain why the results differ.

To explain, fig 4.6 shows a sample strain distribution for a 3D structure with an inclusion embedded in a matrix. This sample is an ellipsoid with a cuboid inclusion in the centre. After tension load in the x direction, sample would show strain changes. The green rectangular represents a fiber inclusion. Ellipses around inclusion indicate matrix strain distributions. The different color areas in the ellipsoid means different strain levels. Here we assumed the highest strain was indicated with red color, the lowest strain was indicated with blue color, and yellow is in the middle. Figures 4.6a and c show the strain in a layer close to the fiber. Figure 4.6a shows strain on the layer (x-y plane) in the centre of sample; Figure 4.6c shows 3D structure for strain distribution in Figure 4.6a. But if layer is far away from fiber, such as Figures 4.6b and d, the strain fields are totally different. Figure 4.6b shows strain in a layer



**Figure 4.6: 3D strain distribution. (a). 2D visualization of strain on centre layer (x-y plane). (b). 2D visualization of strain on layer far away from inclusion(x-y plane). (c). 3D visualization of strain on centre layer (x-y plane). (d). 2D visualization of strain on layer far away from inclusion(x-y plane).**

(x-y plane) far away from sample and Figure 4.6d shows 3D structure for the strain distribution in Figure 4.6b. The x-y layer strain distribution changes as the layer moves away from the fiber.

The 2D simulations did not agree well with DIC experiments (Figure 4.5). The reason is because sample is 3D and DIC measured strains on the surface of sample away from the inclusion, but 2D simulation can only model strains in a layer containing the inclusion. As illustrated in Figure 4.6, the stress disturbance around the particle will fade away as you move away from the inclusion. These sample 2D simulations showed that modeling has to account for this affect and therefore has to use 3D simulations.

#### 4.2.3 3D modeling

Because 2D simulations were not adequate, 3D MPM simulations were done on the copper wire sample. This section explains how MPM simulates this sample structure in 3D. In 3D simulations, we set the thickness of the copper wire and adjusted position of copper wire

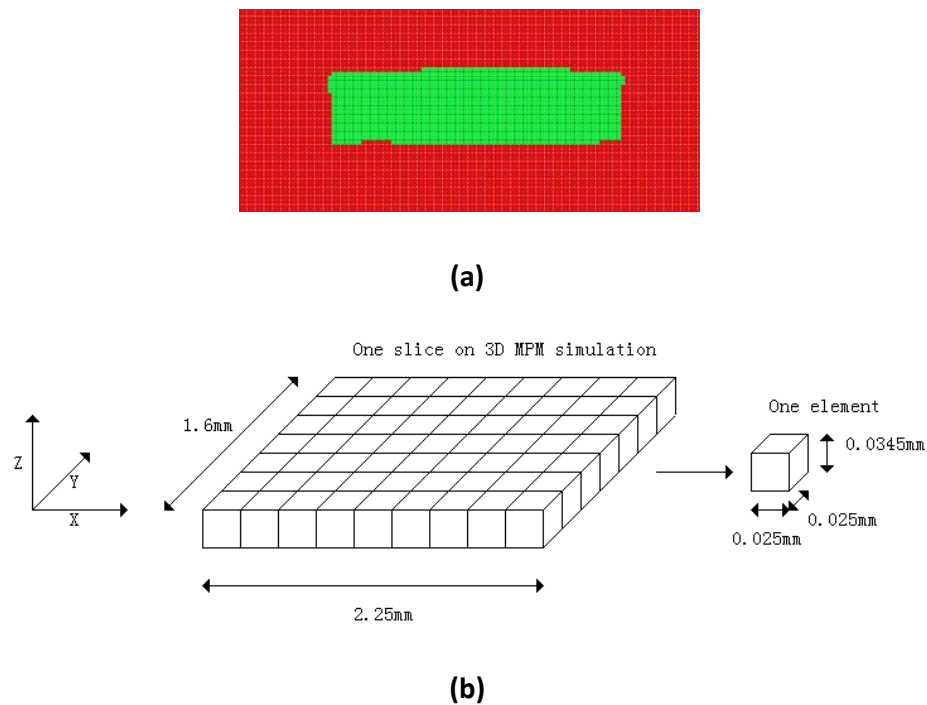


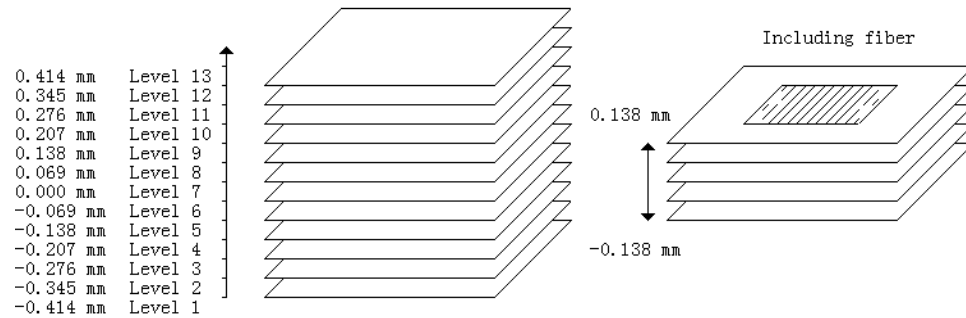
**Figure 4.7: Layer containing copper fiber. (a) Visualization of MPM on a layer contain fiber. (b) Structure of one layer on 3D MPM simulation**

within the thickness (z) direction.

Figure 4.7a shows MPM visual image of the copper wire specimen. This image is a projection of the inclusion. This copper wire was cylindrical, but we did not have enough information to model that shape accurately. We decided to use 3D calculations to account for change in strain field as function of distance away from the inclusion, but to assume the details of the cross section of the inclusion are less important. The model was thus constructed as follows:

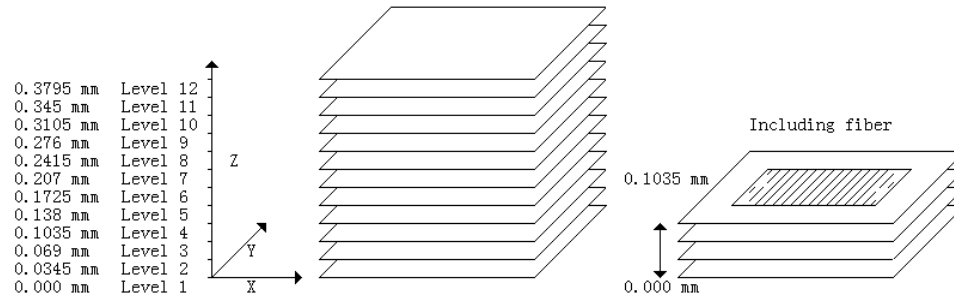
- The thickness direction was divided into 13 layers, each layer had thickness 0.0345mm (Figure 4.7b).
- The image (Figure 4.3b) was used to discretize several layers of matrix and inclusion (Figure 4.6b). The layer resolution was  $90 \times 64$  elements (element size is  $0.025 \times 0.025$ mm). Central five layers were set to contain the copper wire, and layers above and below the inclusion were filled with pure matrix. To reduce computational time, we assumed the sample detail in z direction was less important and therefore element size in the z direction could be larger than in the x-y plane.
- We compared strain field within various layers above the copper wire to experimental results.

Figure 4.8 shows the entire structure of a sample for a 3D MPM simulation. It is composed of 13 layers with 5 middle layers containing the fiber. For the entire sample, z coordinate is from -0.414 to 0.414 mm. It is a 3D simulation and computational time was much longer



**Figure 4.8: 3D MPM simulation structure for copper wire specimen, the coordinate of each layer is on thickness (Z) direction. Gap between layers is 0.069 mm**





**Figure 4.9: 3D symmetric simulation on MPM for Copper-Polymer Composite, the coordinate of each slice is on thickness (Z) direction. Interval is 0.0345 mm.**

than for 2D simulations. The gap between layers was set as 0.069mm. However, because this simulation has large gaps in z direction, it was difficult to identify which layer is close to the real sample surface. Moreover, the thickness of the fiber on Figure 4.8 is not close to the real sample (fiber in specimen has diameter 0.207mm but fiber thickness in Figure 4.8 is 0.276mm, i.e. larger and forced to be multiple of larger size). To improve resolution in the z direction, we made use of symmetry as shown in Figure 4.9. The larger z gap is now 0.0345mm. Any smaller gap would cause simulations to take too long.

In Figure 4.9, the size of elements for this simulation was  $0.025\text{mm} \times 0.025\text{mm} \times 0.0345\text{mm}$  so that the thickness of each layer is 0.0345 mm. Symmetric coordinate system was defined, coordinate zero is the bottom of specimen and is at the center layer of the specimen. Because the thickness of specimen is 0.75mm, half composite was set from

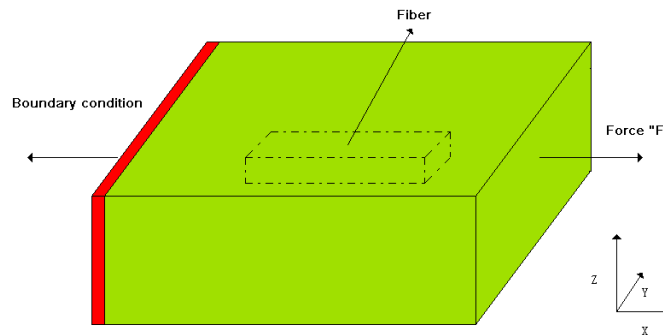


**Figure 4.10: Tension experiment for MPM model, the red part is boundary condition, green part is polymer matrix, and black dashed line represents copper wire inside matrix**

coordinate 0 mm to 0.3795 mm. The copper fiber was set from coordinate 0 mm to 0.1035 mm (This is half wire, for total wire, actual wire thickness is 0.207mm).

Figure 4.10 shows tension load on the 3D MPM model. The red part represents boundary condition so that the specimen was immovable on the left edge. A force was applied to the right edge of specimen in the x direction. The green part represent matrix and dot-dashed line indicates the inclusion within polymer.

#### 4.2.4 Matlab analysis

Qualitative analysis was done use Matlab software. First, the MPM simulation results were extracted as data (during simulations, MPM would generate a series of data files with suffix “.VTK”, each file contains strain and stress data at a certain time). The VTK file is a Simple Legacy file Format that is easy to read and write either by hand or programmatically (VTK User’s Guide). A subroutine was written to read standard VTK files and load data into a Matlab table.

To select the appropriate VTK file to compare to selected experimental results, we compared global axial strain of each VTK file with DIC global axial strain and chose the one closest to experimental global axial strain.

For experimental results, DIC data were extracted as “.csv” files (comma-separated-values file). The “.csv” files recorded experiment results including normal and shear strain on an analysis grid and can be read by Matlab and then directly compared to strains in MPM VTK files.

Figure 4.11 shows an example of transferred DIC data and VTK data from one layer of MPM analysis. In MPM simulations and DIC experimental results, the nodes record information such as normal strain, shear strain, etc. In MPM 3D models, extracted data would form a  $M \times N \times D$  3D matrix and each layer (x-y plane) is composed of  $M \times N$  2D matrix. In DIC results, because we can only measure strains on the surface, the DIC results were transferred to a  $m \times n$  matrix. This example shows a layer (Figure 4.11a, element resolution is  $2 \times 2$ ) composed of a  $3 \times 3$  data matrix (Figure 4.11b).

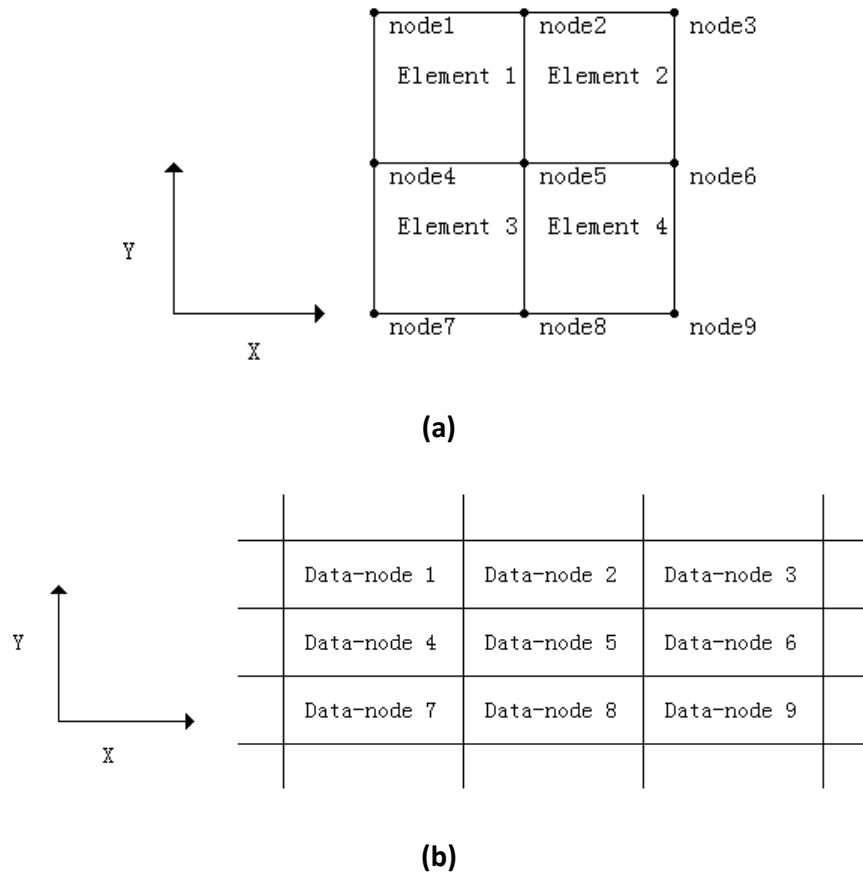


**Figure 4.11: Illustration of transferred data form from DIC and MPM results**

In general, the VTK file had different spatial coordinates than the csv file. In this study, MPM results had element size (x-y plane)  $0.025 \times 0.025mm$ , but DIC results had element size  $0.01237 \times 0.01237mm$ . To compare experimental and simulation results, it was necessary transform DIC coordinates to the VTK coordinate system. In Matlab code the function “interp2” handles interpolation. The detail of this function is that  $ZI = \text{interp2}(X,Y,Z,XI,YI)$  returns matrix ZI containing elements corresponding to coordinates in XI and YI and determined by interpolation within the two-dimensional function specified by matrices X, Y, and Z. X and Y must be monotonic, and have the same format as if they were produced by meshgrid command. Matrices X and Y specify the points at which the data Z is given. After interpolations, both DIC and MPM have same (x-y plane) element resolution  $90 \times 64$  and same element size  $0.025 \times 0.025mm$  for copper wire study, so it can be used to do both qualitative and quantitative comparisons.

#### 4.2.5 Qualitative Comparisons

Because DIC strain data was obtained from the surface of samples and we did not know the exact location of the copper wire, we considered several layers in the analysis. In Matlab code, we used level number instead of coordinate. As shown in Figure 4.8, the symmetric model had 12 layers and each layer corresponds to a coordinate Z. Here we took layers close to sample model surface ( $z = 0.3795\text{mm}$ ), close to the inclusion ( $z = 0.138\text{mm}$ ) and one layer within the inclusion ( $z = 0.0345\text{mm}$ ) for analysis.

Because VTK and csv files include axial strain ( $\varepsilon_{xx}$ ), transverse strain ( $\varepsilon_{yy}$ ), and shear strain ( $\tau_{xy}$ ), we compared each one in separate calculations. Qualitative comparisons were based on visual comparisons. We used Matlab code to transfer the selected strain data to a contour plot:

```
figure(1); contourf(Ve);
```

The function “figure” creates a graphics objects. The function “contourf” gives a filled contour plot that displays isolines calculated from matrix “Ve” and fills the areas between the isolines using constant colors corresponding to the current figure’s colormap. “Ve” is the strain data matrix for one layer of the sample. The visual results of DIC and a certain layer of MPM simulation were then compared with each other, and interpreted based on observed differences.

#### 4.2.5 Quantitative Comparisons

Because simulation results and experimental results were transferred to the same coordinates on an x-y plane, it was possible to do quantitative comparisons. The important step in quantitative comparisons is an error calculation method. We selected a region from visual plots to do quantitative comparisons. The selected region was composed of 2D data

matrix (see Figure 4.11), where each node corresponds to a strain value. The normalized deviation error equation used was:

$$dev \mathcal{E}1 = devError1(\%) = 100 \times \sqrt{\frac{\sum_{i,j=0}^n (D_{ij} - M_{ij})^2}{\sum_{i,j=0}^n D_{ij}^2}}$$

where  $D_{ij}$  is DIC strain data on each grid point,  $M_{ij}$  is MPM strain data on each grid point, and  $dev\mathcal{E}1$  is deviation error 1. The above function gives an error which corresponds to the difference between DIC strain data and MPM strain data. For transverse strain ( $\varepsilon_{yy}$ ) and shear strain ( $\tau_{xy}$ ) the average strain should be zero (because there was no applied transverse or shear load. This zero average did hold for MPM results but it did not hold for experimental results (especially for  $\tau_{xy}$ ). To correct for non-zero means in experiments (which may be an artifact) a new error method was used:

$$dev \mathcal{E}2 = devError2(\%) = 100 \times \sqrt{\frac{\sum_{i,j=0}^n ((D_{ij} - \bar{D}_{ij}) - (M_{ij} - \bar{M}_{ij}))^2}{\sum_{i,j=0}^n D_{ij}^2}}$$

$$= 100 \times \sqrt{\frac{\sum_{i,j=0}^n ((D_{ij} - M_{ij}) - (\bar{D}_{ij} - \bar{M}_{ij}))^2}{\sum_{i,j=0}^n D_{ij}^2}}$$

$$D = DIC \text{ strain Data} \quad M = MPM \text{ strain Data}$$

where  $\bar{D}_{ij}$  is mean value of DIC strain data in the region selected,  $\bar{M}_{ij}$  is mean value of MPM strain data in the region selected, and  $dev\mathcal{E}2$  is deviation error 2. When  $\bar{D}_{ij} = \bar{M}_{ij}$ , as it was for  $\varepsilon_{xx}$ , the two error methods are the same, but for  $\varepsilon_{yy}$ , and especially  $\tau_{xy}$ , error measure 2 allowed us to get results that are less affected by DIC artifacts.

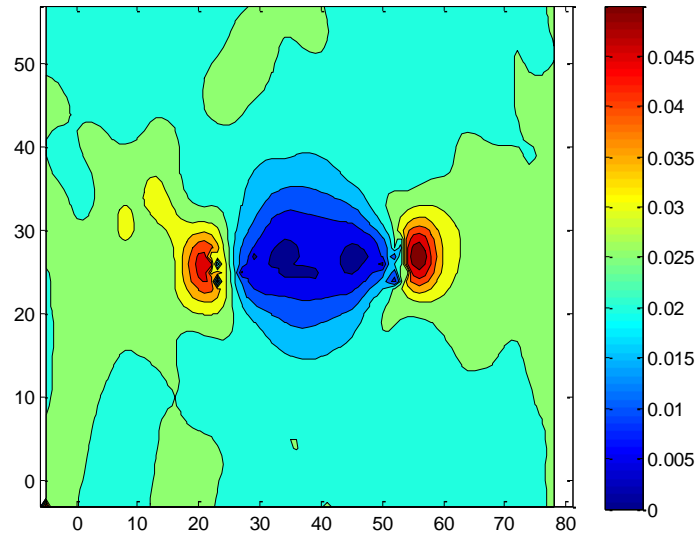


**Figure 4.12: Visual image of DIC axial strain**

### **4. 3 Results and Discussion**

#### **4.3.1.1 Qualitative comparisons for axial Strain ( $\epsilon_{xx}$ )**

Figure 4.12 shows visual axial strain ( $\epsilon_{xx}$ ) results by DIC experiment (The mean strain for this Figure is 2.3%). The copper fiber is in the center of image. The strain inside fiber is from 0 to 1%. The matrix strain away from fiber has axial strain around 2.3%. The high strains (from 3% to 5%) near the ends of the fiber indicate areas of strain concentration.

For MPM 3D simulations, we assumed copper wire is exactly in the middle of the z direction of the composite. The real location of copper wire was not known. We compared DIC to MPM for three layers (z coordinate 0.0345 mm, 0.138mm, and 0.3795 mm). The layer with coordinate  $z = 0.0345$  contained the copper wire, the layer with coordinate  $z = 0.138$  was just above the wire, and layer with coordinate  $z = 0.3795$  was at the surface of the MPM model (see Figure 4.8). The object here was to see if we can determine the known copper modulus (120GPa) by comparison to modeling as a function of its modulus. The following results compared DIC to MPM for moduli of 1000MPa, 30000MPa, and 120000MPa.

Figure 4.13 shows MPM results for axial strain in layer with coordinate  $z = 0.0345$  mm (layer containing copper wire). Figure 4.13a has similar strain in fiber region and matrix region is

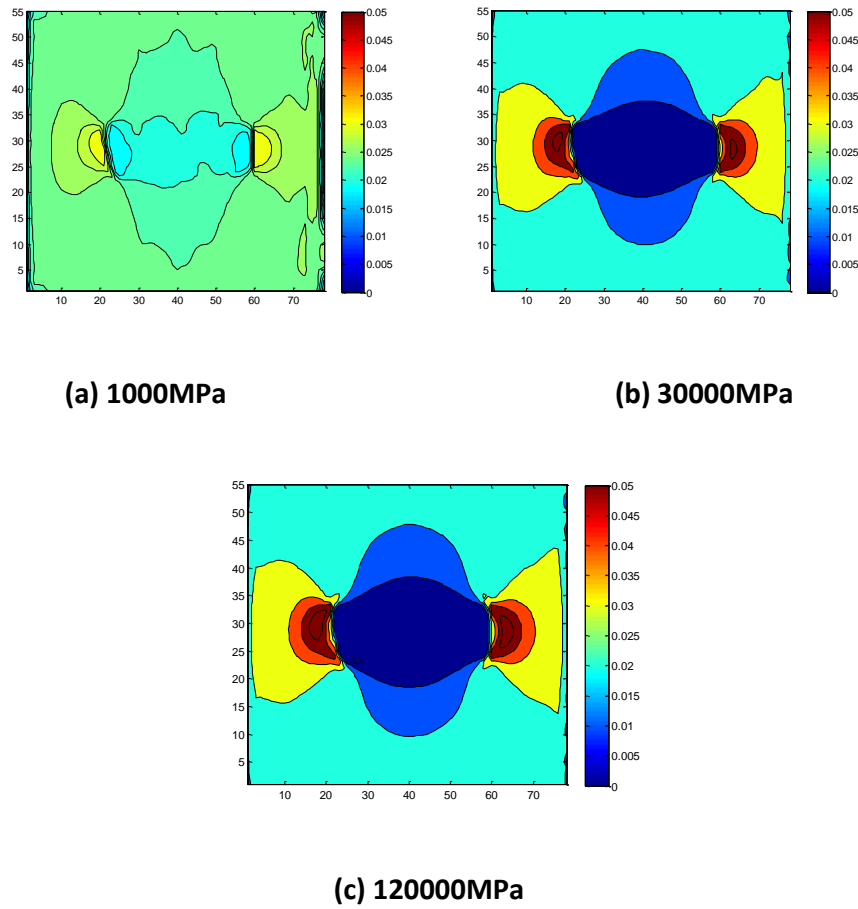


**Figure 4.13: Effect of different fiber modulus on axial strain for layer with coordinate 0.0345 mm**

because fiber modulus is close to matrix modulus. Figure 4.13b and c have very low strain ( $< 5\%$ ) in fiber region is because fiber modulus is much higher than matrix. The visual differences between 30000MPa and 120000MPa are small because fiber modulus is much higher than matrix modulus ( $E_{fiber} \gg E_{matrix}$ ). The increase in  $E_{fiber}$  did not change overall strain field much. Compared to DIC results, the low strain region (blue) in MPM is much larger and the stress concentration areas (red) of MPM are larger than that of DIC and in different positions. These effects are a consequence of selected layer being in the fiber for MPM, but on the surface for DIC.

Figure 4.14 shows MPM results for axial strain in a layer with coordinate  $z = 0.138$  mm (layer just above the copper wire). All three images have strain level around 2% in matrix part, which is close to DIC results. In Figure 4.14a, the fiber is barely seen because its modulus is

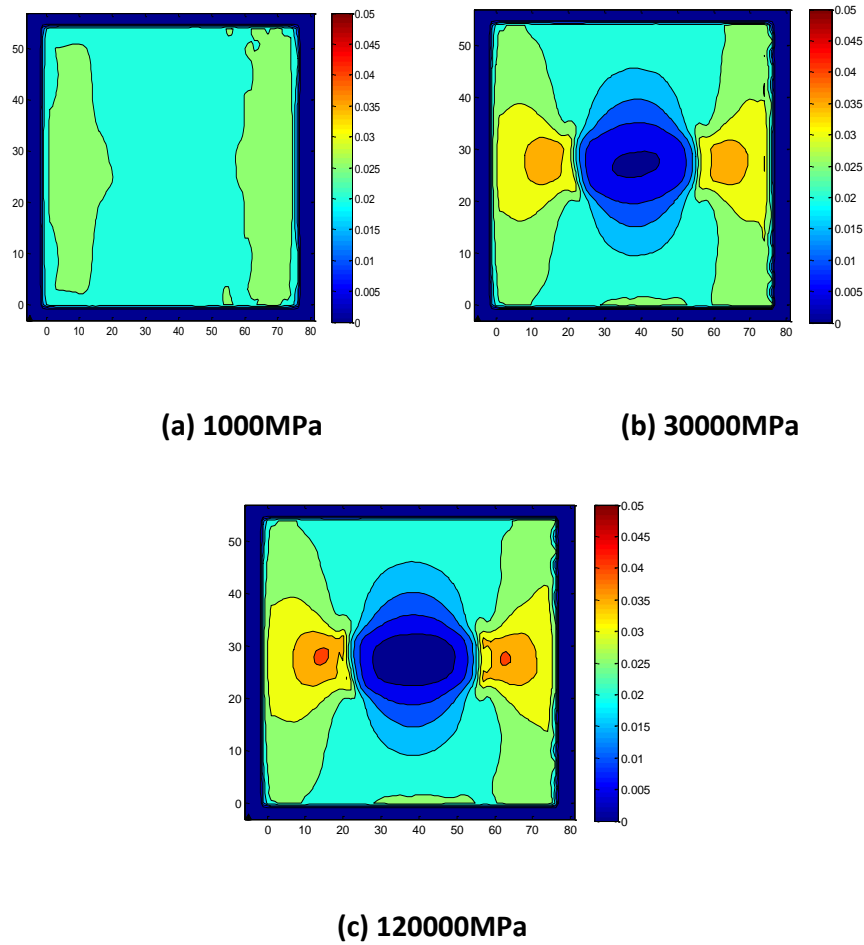


**Figure 4.14: Effect of different fiber modulus on axial strain for layer with coordinate 0.138mm**

close to that of the matrix. Figure 4.14b and c are similar to the layer in the fiber in that the fiber is clearly seen and the difference between 30000MPa and 120000MPa are small because fiber modulus is much higher than matrix modulus ( $E_{fiber} \gg E_{matrix}$ ). Compared to layer in the fiber, these stress concentration zone are closer to DIC results, but still slightly larger. It suggests that actual specimen surface was at a higher layer than this one ( $z = 0.138\text{mm}$ ).

Figure 4.15 shows MPM simulation results for axial strain in a layer with coordinate  $z = 0.3795\text{ mm}$ . This layer is far away from inclusion and close to surface of the MPM model. In the Figure 4.15b and c, the low strain zone (blue) are similar to DIC (Figure 4.12), but stress concentration region (red) was not present which indicated this layer is far away from



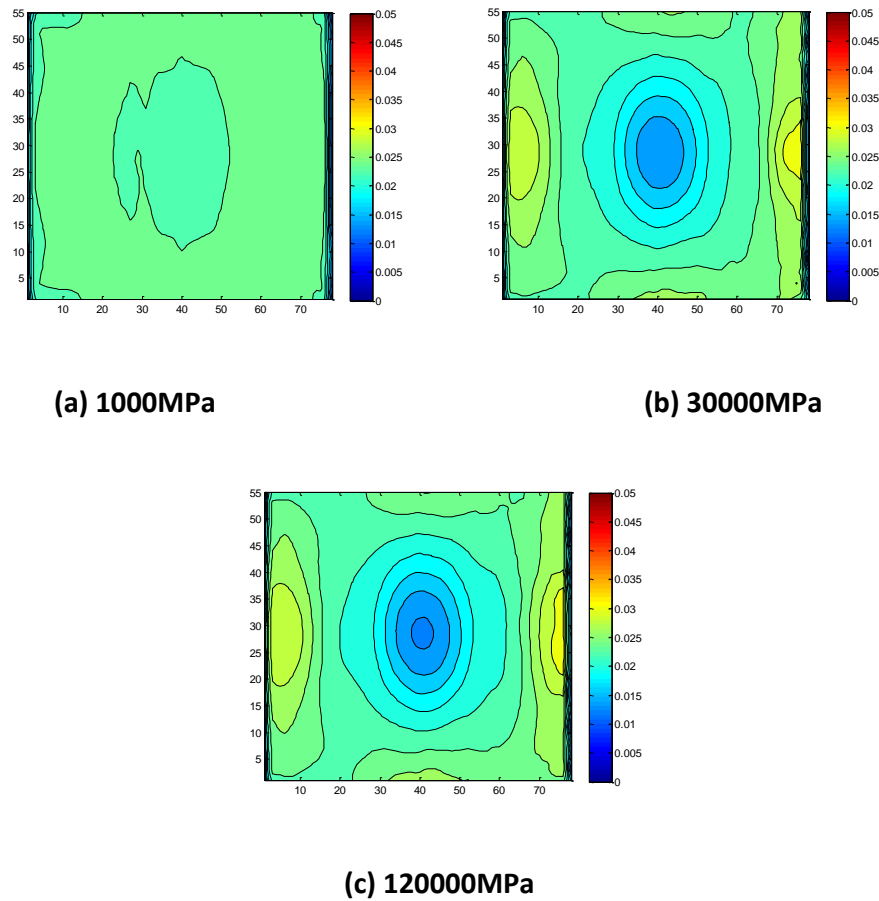


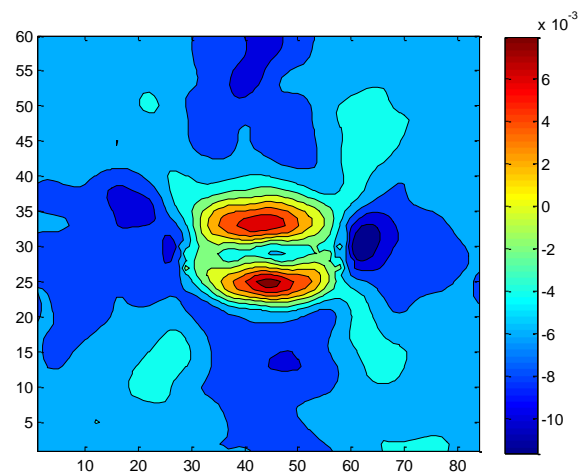
**Figure 4.15: Effect of different fiber modulus on axial strain for layer with coordinate 0.3795 mm**

copper wire so that effect of wire modulus is small. The axial strain distributions in Figures 4.14 and 4.15 suggest actual specimen surface was between  $z = 0.138$  at  $z = 0.3795$  relative to the fiber.

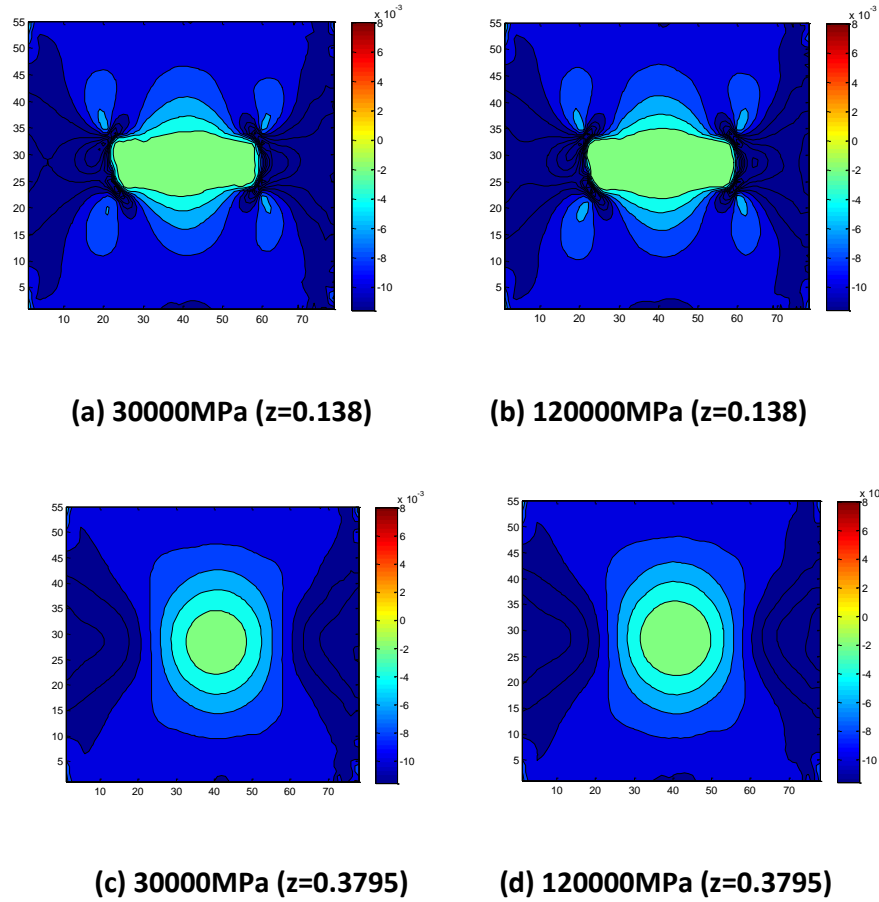
#### 4.3.1.2 Qualitative comparisons for transverse Strain ( $\epsilon_{yy}$ )

Figure 4.16 shows visual transverse strain results of DIC experiment. The strain in the matrix area is around -0.4% (light blue). There are large tensile stress concentration areas (red and yellow) above and below the fiber. This effect was unexpected for well bonded fiber (Based on MPM modeling) and may indicate interfacial debonding with the crack causing stress concentrations.

Figure 4.17 has the MPM simulation results for transverse strain in a layer with coordinate  $z = 0.138$  mm and  $z = 0.3795$  and with fiber modulus  $E = 30$  GPa and  $E = 120$  GPa. As with  $\varepsilon_{xx}$  strain, the effect of inclusion modulus (for high moduli  $> 30$  GPa) is small (little difference between Figure 4.17a and b or Figure 4.17c and d) and the strain concentration area is larger in the layer near the fiber (Figure 4.17a and b) than that at the surface (Figure 4.16c and d). However, the strain in the fiber area differs from DIC results (Figure 4.17). The MPM simulation results did not show the two stress concentration areas as Figure 4.16. The reason may be that MPM assumed a well bonded interface (Interfacial debonding was not available in 3D NairnMPM) in the model. We speculated that if MPM could modeled debonds in 3D model that stress concentrations (see Figure 4.16) would appear. In other words, perhaps debonding is occurring and future work should modify the 3D MPM code to all imperfect interface and debonding using the methods already implemented for 2D interfaces (Nairn 2007).



**Figure 4.16: Visual image of DIC transverse ( $\varepsilon_{yy}$ ) strain**



**Figure 4.17: Effect of different fiber modulus on transverse strain. (a) Wire modulus 30000MPa ( coordinate z=0.138). (b) Wire modulus 120000MPa ( coordinate z=0.138). (c) Wire modulus 30000MPa (coordinate z=0.3795). (d) Wire modulus 120000MPa (coordinate z=0.3795).**

#### 4.3.1.3 Qualitative comparisons for Shear Strain ( $\tau_{xy}$ )

Figure 4.18 shows the shear strain results from DIC experiments. Because the fiber is in the center of sample and loading direction is along the x axis, the shear strain, as expected, is antisymmetric about the middle point of the fiber. The four corners of the fiber have alternating positive and negative shear strain concentrations (The upper left and bottom right have negative strain while upper right and bottom left have positive strain). The stress concentration area has highest absolute value of shear strain 1.2% and most of matrix area has shear strain around 0%.

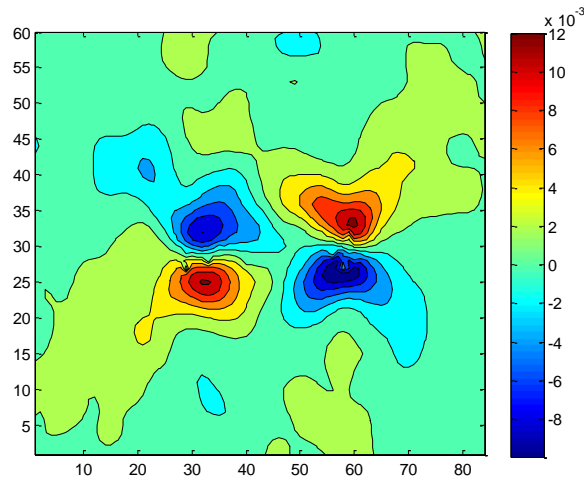


**Figure 4.18: Visual image of DIC shear strain**

Figure 4.19 shows MPM simulation results for shear strain in a layer with coordinate  $z = 0.138 \text{ mm}$  and  $0.3795 \text{ mm}$  and with fiber modulus  $E = 30 \text{ GPa}$  and  $E = 120 \text{ GPa}$ .

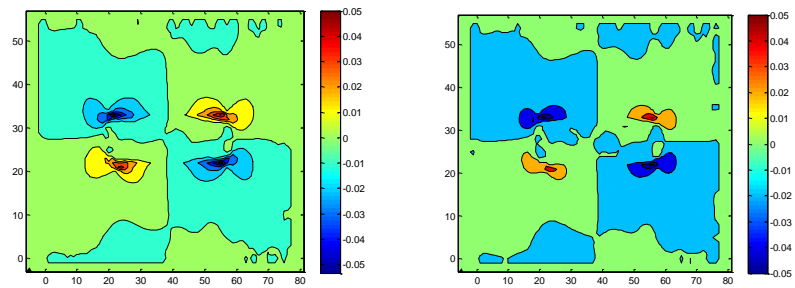
Because MPM results and DIC results had different strain range (MPM strain range  $\ll$  DIC strain), we had to use a small shear strain range for plotting MPM results. Although strain ranges are different between DIC result and MPM, the MPM simulations also show similar antisymmetric shape as in the DIC plots. There is little difference in plots between inclusion modulus  $30 \text{ GPa}$  and modulus  $120 \text{ GPa}$  on the same layer (Compare Figure 4.19a to b or c to d). When the layer was far away from inclusion, the copper wire modulus has less effect than matrix modulus on the strain value (See Figure 4.19c and d).

#### 4.3.1.4 Conclusion for qualitative comparisons

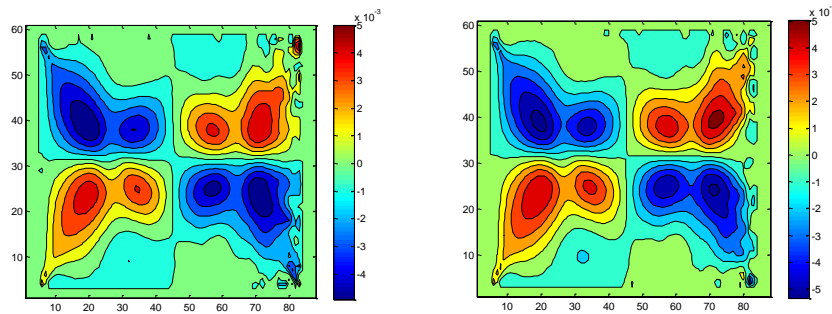
Conclusion for qualitative comparisons:

- a. Higher inclusion modulus is giving results close to experiments, but once it is much higher ( $30000 \text{ MPa}$ ) than the matrix ( $450 \text{ MPa}$ ), all simulation results are about the same. Therefore it is hard to tell the difference between DIC and MPM results because the copper wire is too stiff compared to matrix. Although we could not validate the method of determining modulus, we speculated that using relatively lower modulus wood may work better.

- b. The inclusion modulus is very important for strain within the inclusion, but within the matrix, its influence decreases. For example, in Figure 4.14, 4.17c, d, and 4.19c, d the influence of inclusion modulus is very low. In Figure 4.13, when layer contains the inclusion, the inclusion modulus has a large effect on axial strain within the inclusion. One can conclude that when the layer is far away from the inclusion, the matrix strain will return to global strain which is independent of the modulus of the inclusion. The best way to work around this problem is for the experiment to use thin specimens with the inclusion as close to surface as possible.



(a) 30000MPa ( $z = 0.138\text{mm}$ )      (b) 120000MPa ( $z = 0.138\text{mm}$ )



(c) 30000MPa ( $z = 0.3795\text{mm}$ )      (d) 120000MPa ( $z = 0.3795\text{mm}$ )

**Figure 4.19: Effect of different fiber modulus on shear strain**

- (a) Copper wire modulus 30000MPa ( coordinate  $z=0.138$ ). (b) Wire modulus 120000MPa ( coordinate  $z=0.138$ ). (c) Wire modulus 30000MPa (coordinate  $z=0.3795$ ). (d) Wire modulus 120000MPa (coordinate  $z=0.3795$ ).

### 4.3.2 Quantitative comparisons

#### 4.3.2.1 Quantitative comparisons for different regions

Because simulation results and experimental results could be transferred to the same coordinates on x-y plane in Matlab, it was possible to do quantitative comparisons on a point by point basis.

Because most of the inclusion effect were near the fiber based on the qualitative comparisons, we compared DIC to simulation over various areas all centered on the fiber. For the copper wire specimen, we took four regions from small to large to do comparisons. Figure 4.20 shows the four regions on DIC axial strain image. The size of these regions are A = 22×9 elements, B = 34×21 elements, C = 46×34 elements, and D = 62×50 elements (element size is  $0.025 \times 0.025\text{mm}$ ).

Figure 4.21 shows results of axial strain deviation error 2 for each regions (see Figure 4.20) with coordinates  $z = 0.3795\text{mm}$  (i.e., near the surface). On the whole, the error for each region decreased as modulus of inclusion increased. One of objectives for quantitative comparisons is to find the modulus by locating a minimum in the error as a function of modulus. The minimum error did not occur. The reason is that the surface strain becomes independent of modulus for high modulus, which causes the error to become constant as well. In other words, the observation of surface strain cannot be used to determine modulus of the inclusions. We can tell from the decreasing error at low modulus, however,

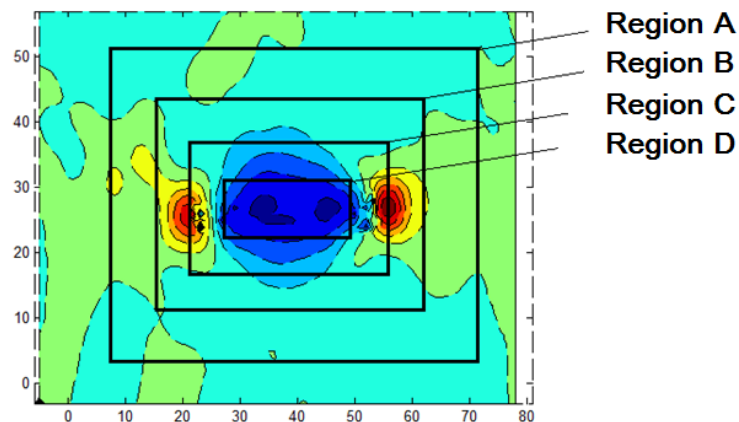


**Figure 4.20: Four selected regions on DIC axial strain field**

the inclusion modulus must be greater than 30,000 MPa.

Although we hoped to find a minimum at error curve, the error for each regions shows decreasing trend (Inclusion modulus up to  $10^{4.5} = 31000\text{MPa}$ ) and a plateau at high modulus (Inclusion modulus greater than  $10^{4.5} = 31000\text{MPa}$ ). These quantitative results are similar to the qualitative comparison result where the plots were independent of inclusion is when its modulus was much greater than the matrix modulus. In Figure 4.21, the error is smaller for larger regions (Region A, B, and C) which is because we selected MPM strain data (VTK file) based on global matrix strain. For large regions, the error calculation included more matrix, which is known to be correct (on the average), and therefore the error was lower. On the contrary, if we selected small region (Region D) to do quantitative analysis, most of strain area is close to inclusion, the errors were larger, but the error also was more sensitive to the inclusion modulus. One conclusion is that small regions inside the fiber area are more suitable than large regions for quantitative analysis. Based on this conclusion, all subsequent calculations for copper and WPC specimen used small regions (Region D) inside the inclusion area to do quantitative comparisons.

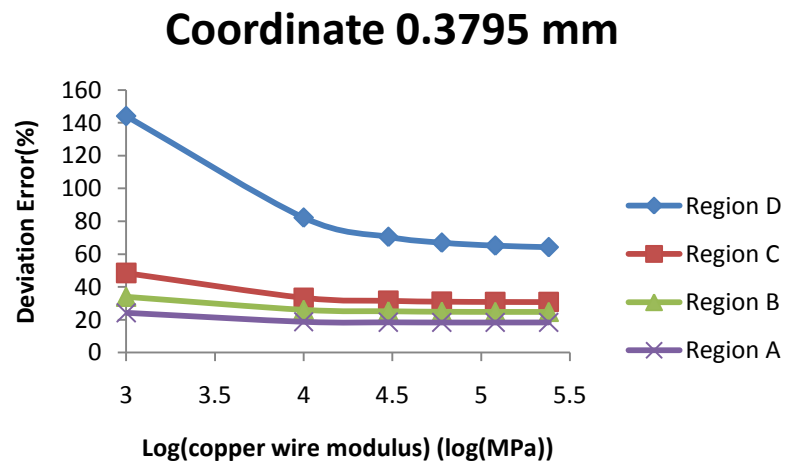


**Figure 4.21: Deviation error for selected regions in a layer with coordinate  $z = 0.3795\text{mm}$**

#### 4.3.2.2 Quantitative comparisons on axial strain ( $\epsilon_{xx}$ )

Figure 4.22 shows deviation error for axial strain in a layer with coordinate 0.3795 (surface layer). As we mentioned, the object of quantitative comparison was to find best match surface layer position and inclusion modulus in the simulation to experiment. However, one cannot find lowest error in this because and the surface axial strain is nearly independent of inclusion stiffness as long as inclusion is much stiffer than the matrix (450MPa). As modulus of inclusion increased from  $10^3$  to  $10^{4.5}$ MPa in the axis (See dashed line in the plot), one can observe distinct decreasing of error from 140% to 80%. When copper wire modulus is higher than  $10^{4.5}$ MPa (dashed line), its effect becomes very low.

To explain these results, we did a sensitivity analysis for axial strain. For sensitivity analysis, we took average strain on the region (Region D on Figure 4.20) in the centre of copper wire to do comparisons. Figure 4.23 shows sensitivity analysis for axial strain on small region inside inclusion. Triangle was indicated with average strain of region D in a layer with coordinate 0.3795mm (Surface layer). Square was indicated with average strain of region D in a layer with coordinate 0.0345mm (Layer contains copper wire).

One goal of sensitivity analysis is to find the reason of no minimum error in the quantitative comparison. For surface layer, the average strain decreased fast over the first part (Inclusion modulus from 3 to 4.5 log(MPa)) but then reached a plateau. For layer including copper, the

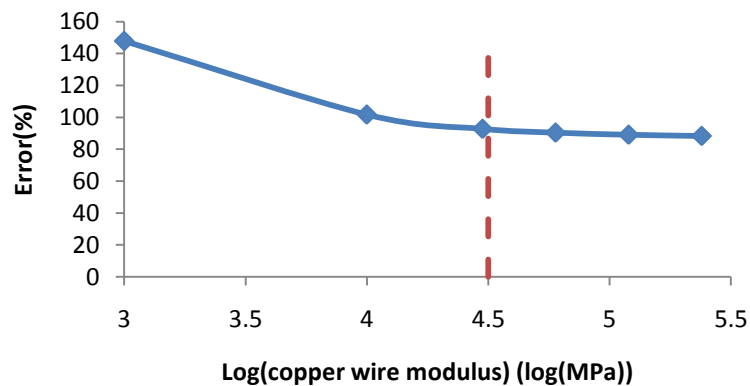


**Figure 4.22: Deviation error for axial strain in a layer with coordinate  $z = 0.3795$ mm.**



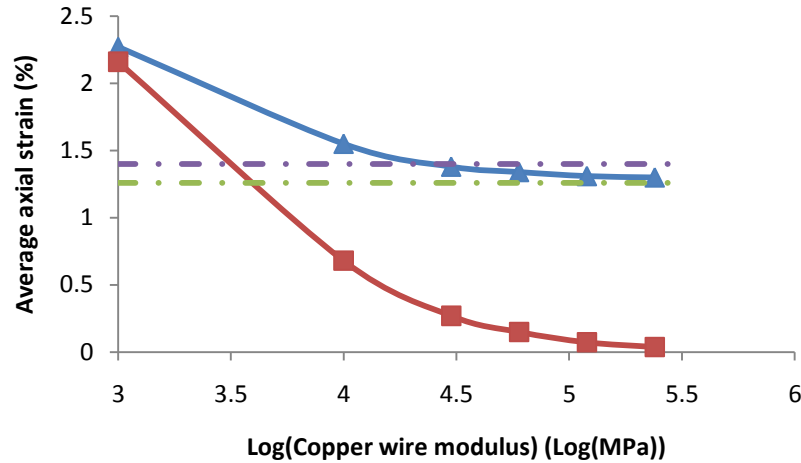


**Figure 4.23: Sensitivity analysis for MPM simulations**

average axial strain kept decreasing from inclusion modulus  $10^3$  to  $10^{5.5}$  MPa. The task of inverse modeling is to determine the copper modulus from the measured average strain. Figure 4.23 shows that in the surface region (triangles) if the measured strain is around 1.3%, the copper modulus could have any value about  $10^{4.5}$  MPa and the modulus could not be determined at all if the measured strains had come uncertainty (e.g., the distance between the two dash-dot line in Figure 4.23). On the other hand, if we could measure the strain in the fiber (squares), any measure strain would translate into a unique copper modulus.

Combining quantitative analysis (Figure 4.22) and sensitivity analysis (Figure 4.23), the conclusion is that the copper wire is too stiff to determine its modulus by observing polymer surface strain. In the next chapter, we used lower modulus wood particle instead of stiff copper, the longitudinal modulus of solid wood is around 10GPa and wood particle modulus is lower. Figure 4.23 shows that in this region the strain is affected by modulus so maybe the methods will work with wood particles.

#### 4.3.2.3 Quantitative comparisons on transverse strain ( $\epsilon_{yy}$ )

Figure 4.24 shows deviation error for transverse strain in the surface layer. It has similar results compared to axial strain results (See Figure 4.22). The error changed fast from inclusion modulus 1GPa to 30GPa ( $\log 1000 = 3$  and  $\log 30000 = 4.48$  dashed line), and then goes to a plateau when modulus of copper wire is high. Therefore we get the same

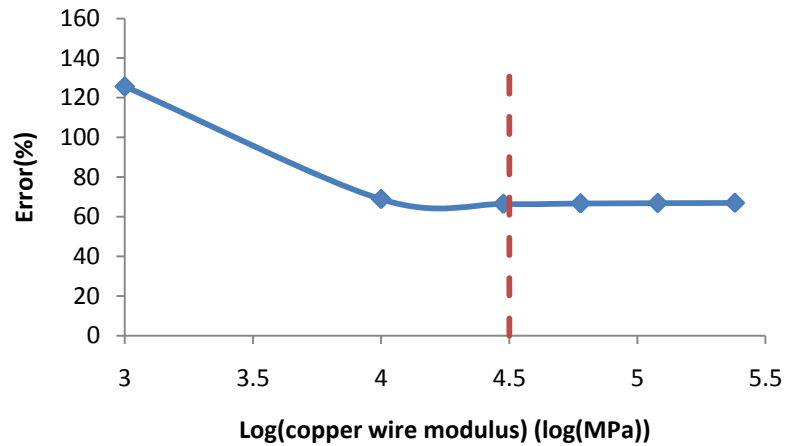


**Figure 4.24: Deviation error for transverse strain. Layer with coordinate  $z = 0.3795\text{mm}$ .**

conclusion as from the axial strain analysis (Figure 4.22) that copper wire is too stiff to determine its modulus by observing polymer surface except to determine that its modulus is greater than 30GPa.

#### 4.3.2.4 Quantitative comparisons on Shear strain ( $\tau_{xy}$ )

Figure 4.25 shows deviation error for shear strain in the surface layer. One can hardly find useful information from Figure 4.25 because little change of error from inclusion modulus 1000MPa to 240000MPa ( $\log 240000 = 5.38$ ). It is because calculation of shear strain from

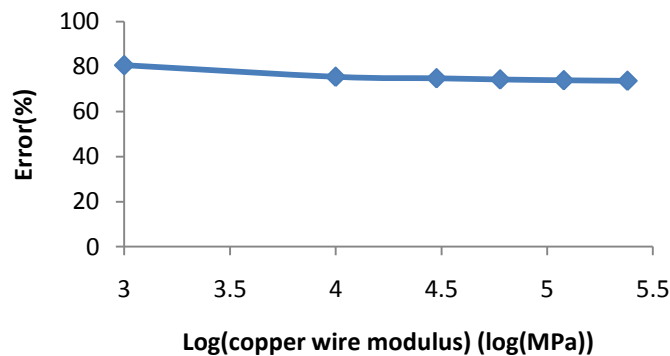


**Figure 4.25: Deviation error for shear strain. Layer with coordinate  $z = 0.3795\text{mm}$ .**

DIC software has wrong sign (which we corrected) but may have other artifacts as well. Therefore, we did not consider quantitative shear strain analysis in the conclusion.

#### 4.4 Conclusions

The copper wire study shows that MPM simulation works well for simulating 3D composite structures and that using Matlab software, it is possible to do both qualitative and quantitative comparisons between DIC and MPM. However, we did not get good validation for determination of modulus. Both qualitative and quantitative comparisons show that once copper wire modulus is much higher than matrix ( $30\text{GPa} \gg 450\text{MPa}$ ), the effect of inclusion on surface strains is small. Numerical modeling shows that the effect remains within the fiber (see Figure 4.23), but DIC cannot measure that strain; it can only measure surface strain. Combining qualitative, quantitative and sensitivity analysis, the conclusion is that copper wire is too stiff compared to polymer or specimen is so thick that inclusion modulus has low effect on the surface of sample (DIC experimental results) to get good validation. Although copper did not work, the error variations at low modulus hope that the methods will be adequate for wood particles experiments, as explained in the next chapter. The situation with wood particle might be better because modulus of wood is much lower than copper (10 to 15GPa vs. 120GPa). The modulus of wood flour particle is probably also lower than wood (Due to damage  $< 10\text{GPa}$ ). Their moduli are in the range (1GPa to 10GPa) where errors are changing and therefore we might find a minimum value and be able to do inverse modeling.

## **CHAPTER 5: WPC EXPERIMENTS AND QUALITATIVE ANALYSIS**

### **5.1 Introduction**

3D MPM simulations were demonstrated as feasible in the copper wire validation study, but the copper wire was too stiff to be able to determine its modulus by comparison of DIC experiments to models. In this chapter, wood particles were used instead of copper. The loading model is still tension, but the wood particles had various angles with respect to the loading direction and the angles used were 0 degrees, 45 degrees, and 90 degrees. This chapter describes qualitative comparisons between DIC and simulation as done in the copper wire study. In the 90 degree specimen, plastic collapse of the wood particle was needed for improved comparisons indicating the particle may have debonded or had transverse cracking. In the 45 degree study, we simulated strain changes as a function of distance between the surface and the inclusion and were able to match strain effects seen in the experiments.

### **5.2 Material and method**

#### **5.2.1 Sample dimension**

In this study, wood particles and polyethylene were used to make sample composites. Wood particles in the experiments were selected at different angles with respect to the loading direction (x direction). Differential Image Correlation (DIC) was used for surface strain characterization of wood particles embedded in the polymer matrix composites. The digital image correlation (DIC) method obtains the incremental displacement and strain field on the surface of a planar specimen by comparing a pair of digital images taken before and after the deformation (Su, C and Anand. L 2003). DIC images were collected along with average strain vs. applied load curves. At selected applied loads, the DIC images were analyzed using Vic-2D 2009 (developed by Correlated Solutions) to determine experimental strain fields. In addition, conventional 2D microscopic techniques (regular light microscopy) were used to provide visual supporting information on the morphology of the WPC

specimens. The sample experiments and DIC experiments in tension were done by Matthew J. Schwarzkopf.

The 0 degree wood particle specimen width was 5.1mm, length was 29.45mm, and thickness was 0.7mm. The measured wood particle mean length was 1.162mm and mean diameter was 0.235mm. The 90 degree wood particle specimen width was 5mm, length was 28mm, and thickness was 0.65mm. The measured wood particle mean length was 0.982mm and mean diameter was 0.201mm. The 45 degree wood particle specimen width was 4.35mm, length was 30mm, and thickness was 0.6mm. The measured wood particle mean length was 1.341mm and mean diameter was 0.22mm. All specimens were subject to tensile loading in the x direction with constant displacement rate of 0.5mm/s.

Figure 5.1 show micrographs for part of the wood plastic composite specimen surfaces used

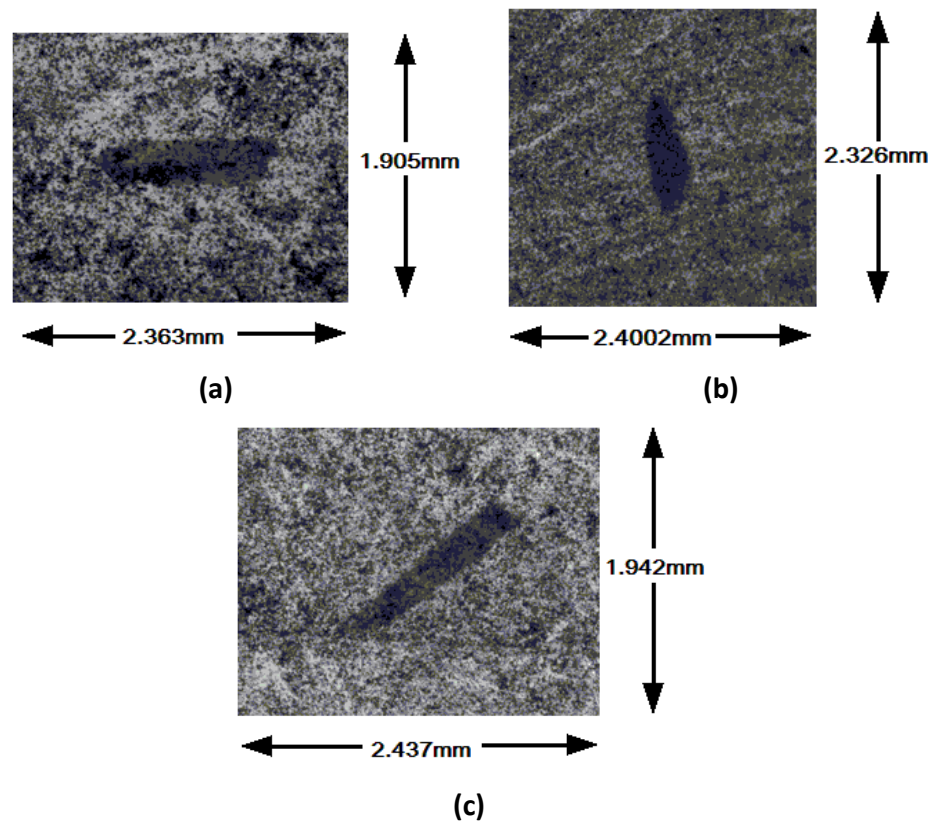


**Figure 5.1: Visualization of a part of WPC sample surface used in the MPM simulations. (a) 0 degree wood particle sample. (b) 90 degree wood particle sample. (c) 45 degree wood particle sample.**

for the MPM simulations. To analyze these WPCs in MPM, the images were converted into a 256 level grayscale bitmap image (a standard, uncompressed, BMP file (Bourke 2004)). The resolution of the Figure 5.1a, as obtained, was  $955 \times 770$  pixels and it images an area of  $2.363 \times 1.905$  mm; the thickness of the 0 degree sample in MPM simulations was set to 0.75mm. The resolution of the Figure 5.1b, as obtained, was  $970 \times 940$  pixels and it images an area of  $2.4002 \times 2.3259$  mm, the thickness of the 90 degree sample in MPM simulations was set to 0.63mm. The resolution of the Figure 5.1c was  $985 \times 785$  pixels and the image covers an area approximately  $2.437 \times 1.942$  mm, the thickness of 45 degree sample on MPM simulations was set as 0.65mm.

### 5.2.2 Sample Properties

The length, width, and aspect ratio of wood particle in the experiments were obtained. However, it is hard to get properties and morphological form of wood particle with such a small scale. Therefore, we made the assumptions below. For the 0 degree wood particle study (Figure 5.1a), we assumed the x direction was the wood longitudinal direction, the y direction was the radial direction, and the z direction was the tangential direction so that the x-y plane was the transverse plane and the x-z plane was the radial plane. For the 45 degree and 90 degree specimens, these axes were rotated 45 or 90 degree about the z axis.

In this chapter, the polymer was set as a Von Mises plastic with modulus 450MPa, density  $1000 \text{ kg/m}^3$ , and Poisson's ratio 0.33. The modulus was determined from initial slope of experiment stress-strain data. For nonlinear hardening the yield strength is given by:

$$\sigma_{Y0} = \sigma_Y(1 + K\alpha)^n$$

where  $\sigma_{Y0}$  is the initial yield strength,  $K$  and  $n$  are dimensionless hardening parameters, and  $\alpha$  is an internal variable that tracks cumulative, equivalent plastic strain. Here the initial yield stress was 6.75MPa. “K” and “n” are dimensionless parameters for nonlinear hardening, here  $K = 5300$  and  $n = 0.2$ , which were determined by fitting to stress-strain curves from the experiments.

For the wood particle properties, we started with Douglas fir's properties in the Wood Handbook as a guide (David W. Green et al. 1999). However, there are several reasons the

modulus of wood particle could be lower. One is that material properties for early wood and late wood are different and the location in the tree that was the source of the sample particle is unknown. Moreover, some special wood structures such as resin canals could be influencing factors. Another one is that we cannot simply set properties of wood particle to be the same as bulk wood because the internal structure of the wood cells could be damaged during machining and hot-pressure processing. In this study, we varied the properties of the wood particle for MPM simulations to find the best matching ones with DIC results. Below are sample models with different properties.

In 3D MPM simulations, the wood particle was defined as a Hill plastic, orthotropic material. This material is elastic plastic, but has an anisotropic criterion to allow yielding at different stresses when loaded in different directions. Table 5.1 shows the orthotropic moduli used

**Table 5.1: Wood particle modulus on different sample**

	Exx	Eyy	Ezz	Gxy	Gxz	Gyz
	(Mpa)	(Mpa)	(Mpa)	(Mpa)	(Mpa)	(Mpa)
Sample 1	8834	913	425	743	686	108
Sample 2	4417	456	212	371	343	54
Sample 3	2208	228	106	185	171	27
Sample 4	1656	171	80	139	128	20
Sample 5	1104	114	53	92.5	85.5	13.5

**Table 5.2: Yield strength used from sample 1 to sample 7**

	yldxx	yldyy	yldzz	yldxy	yldyz	yldxz
	(MPa)	(MPa)	(MPa)	(MPa)	(MPa)	(MPa)
Sample 1-7	$\infty$	5	5	6	2.5	6

for the simulations. Sample 1 is based on bulk wood properties. The other samples scaled each modulus by the same factor. It was not possible to determine the different moduli independently, so we just used scaling as an approach to finding overall mechanical properties. The Poisson ratios were assumed to be the same for all specimens with  $\gamma_{xy} = 0.27595$ ,  $\gamma_{xz} = 0.34858$ ,  $\gamma_{yz} = 0.7089$  and the density of all specimens was set to  $0.39 \times 10^3 \text{ kg/m}^3$ .

Table 5.2 shows yield strength used for sample 1 to 7. Where yldxx is yield strength from a uniaxial tension test in the material's x direction; yldyy is yield strength from a uniaxial tension test in the material's y direction; yldzz is yield strength from uniaxial tension test in the material's z direction; yldxy is yield strength from a pure shear test in the material's x-y plane; yldyz is yield strength from a pure shear test in the material's y-z plane; yldxz is yield strength from pure shear test in the material's x-z plane.

The anisotropic yield criterion is:

$$\left[ F(\sigma_{yy} - \sigma_{zz})^2 + G(\sigma_{xx} - \sigma_{zz})^2 + H(\sigma_{yy} - \sigma_{xx})^2 + 2L\tau_{yz}^2 + 2M\tau_{xz}^2 + 2N\tau_{xy}^2 \right]^{1/2} - (1 + K\varepsilon_p^n) \leq 0$$

where  $\sigma_{xx}$ ,  $\sigma_{yy}$ ,  $\sigma_{zz}$ ,  $\tau_{yz}$ ,  $\tau_{xz}$ , and  $\tau_{xy}$  are stresses in the material axis system after rotation from the analysis coordinates. The constant are determined by the yield strengths:

$$2F = (1/yldyy^2) + (1/yldzz^2) - (1/yldxx^2)$$

$$2G = (1/yldxx^2) + (1/yldzz^2) - (1/yldyy^2)$$

$$2H = (1/yldxx^2) + (1/yldyy^2) - (1/yldzz^2)$$

$$2L = (1/yldyz^2)$$

$$2M = (1/yldxz^2)$$

$$2N = (1/yldxy^2)$$

For plane stress analysis,  $\sigma_{zz} = 0$  and the material property  $\sigma_Y$  corresponds to the yield strength under uniaxial tension (yielding when  $\sigma_{xx} \geq \sigma_Y$ ).

According to former damping study on chapter 2, we used “feedback damping =  $5000(1/\text{mm}^2)$ ” here.



### 5.2.3 3D simulation structure

Figure 5.1 shows the original images of sample surfaces. Because there were too many speckles around wood particles on the Figure 5.1, which made it hard to identify by MPM simulation, it was necessary to convert the original image to a simple color one. Here we used “ImageJ” program to treat Figure 5.1. First, we drew a contour line around the inclusion. The next step was to fill the particle part and polymer part with color. Figure 5.2 shows converted images of wood particle/polymer composite surface. For the image in Figure 5.2c, the gray scale intensity was used to identify both the particle and its angle. Here we chose angles from -90 to 90 degree to correspond linearly to intensities from 0 to 255 so that 45 degree (Figure 5.2c) corresponds to intensity  $y = (45 - (-90)) / 180 * 255 = 191.25$ . For 5.2a and b, the fiber particles were assigned to 0 or 90 degree rotation, respectively. The polymer was taken as 0 degree (Intensity is  $(0 - (-90)) / 180 * 255 = 127.5$ ), although the angle

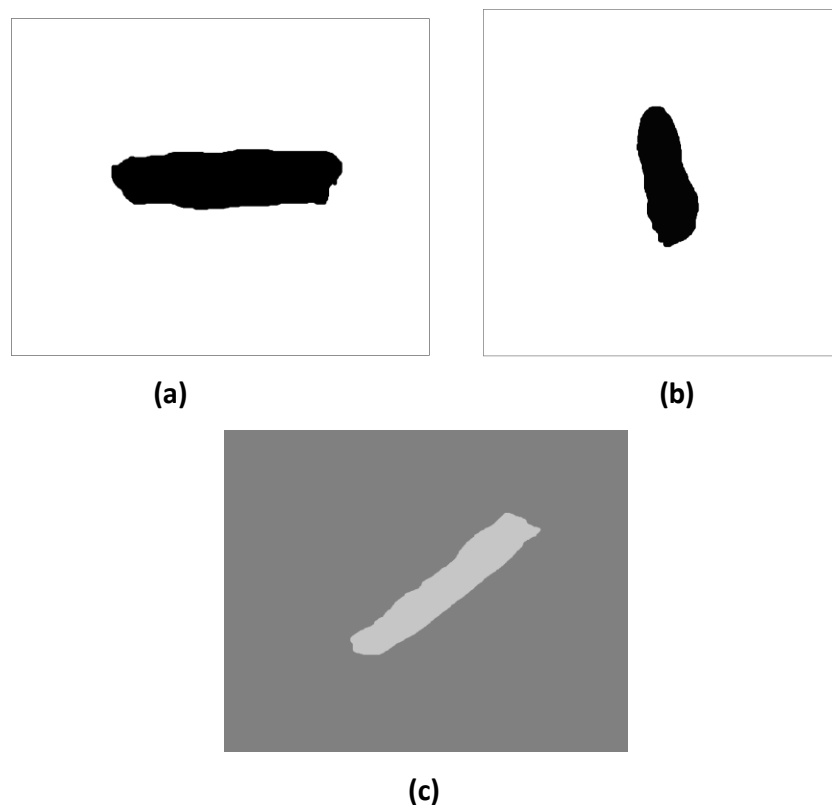


**Figure 5.2: Converted 256 level grayscale bitmap image. (a) 0 degree wood particle sample. (b) 90 degree wood particle sample. (c) 45 degree wood particle sample.**

is irrelevant for isotropic materials.

Next, we imported the final BMP images to MPM simulations. The process to import the BMP image (Figure 5.2) to MPM was as follow: An MPM background mesh was defined with a number of regular, cubical elements covering a volume greater than the image area. Each element in the mesh was assigned to have eight possible locations for material points each representing one eighth of the element volume. The MPM code then maps the BMP image to the mesh slice-by-slice and evaluates the average intensity of the image location corresponding to each potential material point location. Based on the average image intensity, each location was either assigned to have a material point representing wood particle material or representing polymer material. For the 45 degree specimen, the intensity also determine the angle. The resolution of the MPM discretization could be adjusted arbitrarily to vary accuracy of digitizing the image. In these 3D simulations, we assumed details of the cross section of the inclusion are less important. The details of the 3D process were:

- a. For 0 degree particle simulation, MPM model used a background grid for the image of  $105 \times 80$  elements (element size is  $0.025 \times 0.025mm$ ). This background grid provides for  $210 \times 160 = 33,600$  potential locations for particles, in each layer of the 3D model. The thickness direction was divided into 14 layers; each layer has thickness  $0.02917mm$ .
- b. For 90 degree particle simulation, the elements resolution on x-y plane was set as  $106 \times 97$  elements (element size is  $0.025 \times 0.025mm$ ). and the 3D mesh was set as  $106 \times 97 \times 13$  elements. Each layer had thickness of  $0.02625mm$ .
- c. For 45 degree particle simulation, the mesh behind the image had  $107 \times 82$  elements or  $217 \times 164 = 35,588$  particle locations on x-y plane (element size is  $0.025 \times 0.025mm$ ). For 3D analysis, thickness direction was divided into 13 layers, each layer had thickness of  $0.02708mm$ .

Because the DIC strain field is on the surface plane, we took one layer from MPM simulations for comparison. A simple 3D MPM simulation model for 0 degree sample is shown in Figure 5.3, where layers are identified by Z coordinate. To save the computational time, the sample model

is assumed to be symmetric, and only half of the sample was modeled. The entire sample thickness was 0.75834mm, the simulation model was from the center layer of sample to the surface layer of the sample (0 to 0.37917mm). Layers containing half the wood particle were from coordinate  $Z = 0$  to  $Z = 0.11667$ mm. As done for copper wire, all wood particle layers used the same image based on projection of the fiber because we did not have enough structural information to do otherwise. The remaining layers were pure matrix.

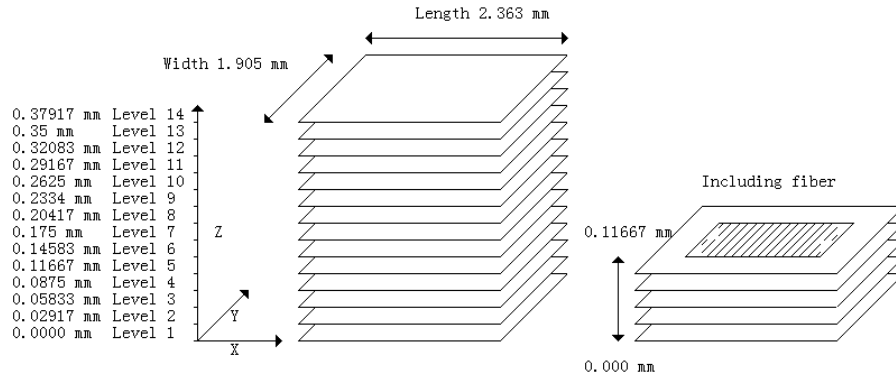


**Figure 5.5: Simple 3D MPM simulation model, half sample is from coordinate  $Z = 0$  to 0.37917mm; half wood particle is from coordinate  $Z = 0$  to 0.11667mm**

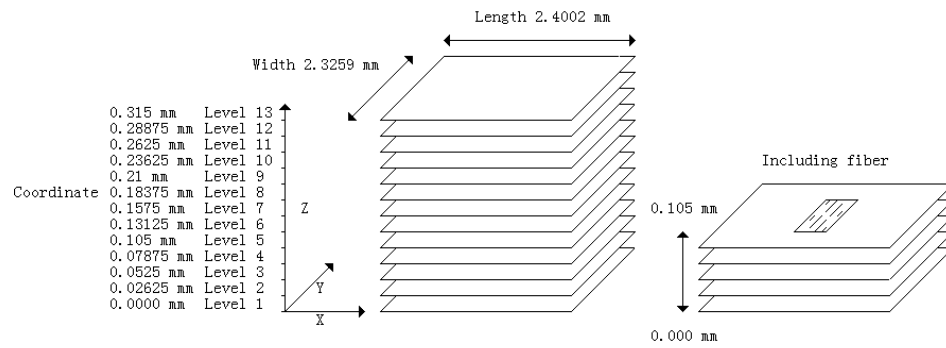


**Figure 5.4: Simple 3D MPM simulation model, half sample is from coordinate  $Z = 0$  to 0.315mm; half wood particle is from coordinate  $Z = 0$  to 0.105mm**

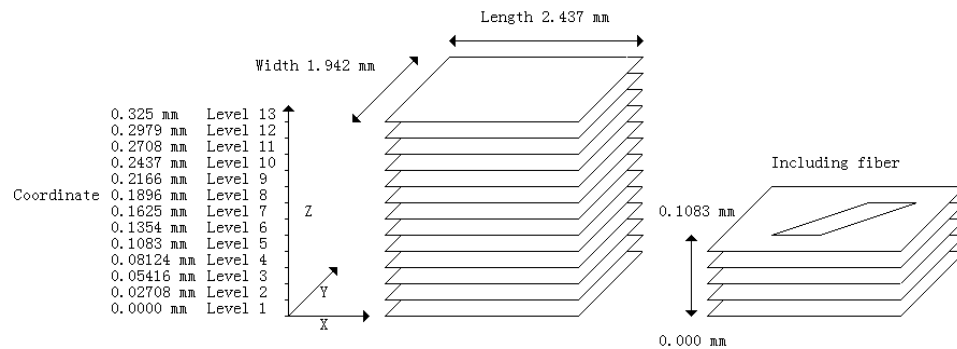


**Figure 5.3: Simple 3D MPM simulation model, assumed half sample is from coordinate  $Z = 0$  to 0.325mm and assumed half wood particle is from  $Z$  coordinate 0 to 0.1083mm**

A sample 3D MPM simulation model for the 90 degree sample is shown in Figure 5.4, where each layer is identified by Z coordinate. The sample model was assumed to be symmetric. The whole modeled sample thickness was 0.63mm, the simulation model was from the center layer of sample to the top layer of sample (0 to 0.315mm). Layers contain wood particle were from coordinate  $Z = 0$  to  $Z = 0.105$ mm. The remaining layers were pure matrix.

A sample 3D MPM simulation model for the 45 degree sample is shown in Figure 5.5, where each plane was identified by Z coordinate. The model was assumed to be symmetric, and only half of sample was modeled. The whole sample thickness was 0.65mm, the simulation model was from the center layer of sample to the top layer of sample (0 to 0.325mm). Layers contain wood particles were from coordinate  $Z = 0$  to  $Z = 0.1083$ mm. The remaining layers were pure matrix.

Tension experiments are illustrated in Figure 5.6. The right side of the specimen was drawn by a tension force “F”. The left edge of the specimen was restrained by a boundary condition to confine tension to the x direction. The loading function was:

$$F = 150.735 \times t$$

Here F is loading force at the one edge of sample with unit Newtons (N); t is loading time in units of millisecond (ms). All calculations were done using three dimensional, explicit MPM methods. After loading, MPM would generate a series of results at selected times. Here the

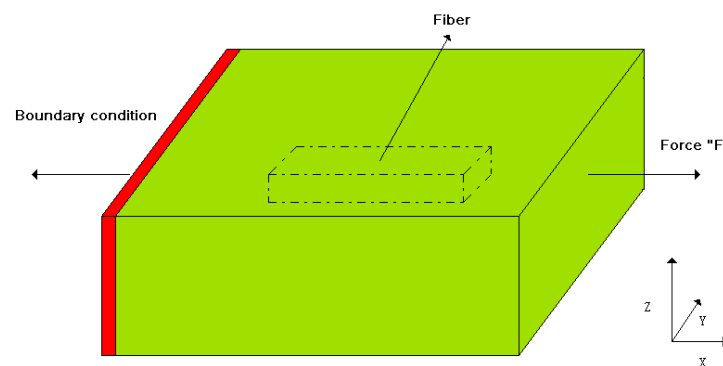


**Figure 5.6: Tension experiment for MPM model, the red part is boundary condition, green part is polymer matrix, and black dashed line represents wood particle inside matrix**

time step is 2.7500689e-06ms, which was determined automatically by MPM. Finally, we compared global strain of MPM results at each step with global strain of DIC results; the closest one of the MPM results was selected to do qualitative comparisons.

#### 5.2.4 Matlab analysis

The Matlab analysis for qualitative comparisons used in this study was the same one described in section 4.2.4 in chapter 4.

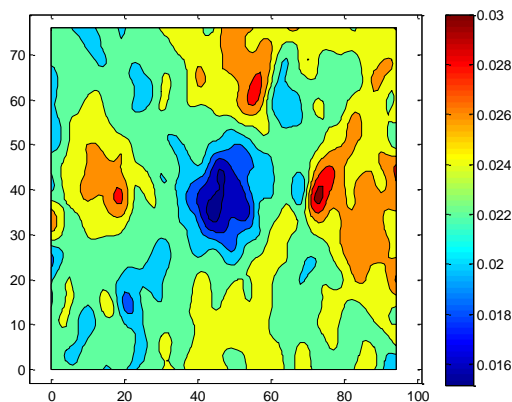
### 5.3 Results and Discussion

#### 5.3.1 0 degree sample

This section is the qualitative study for the 0 degree wood particle specimen. We looked at  $\epsilon_{xx}$ ,  $\epsilon_{yy}$ , and  $\gamma_{xy}$  strains.

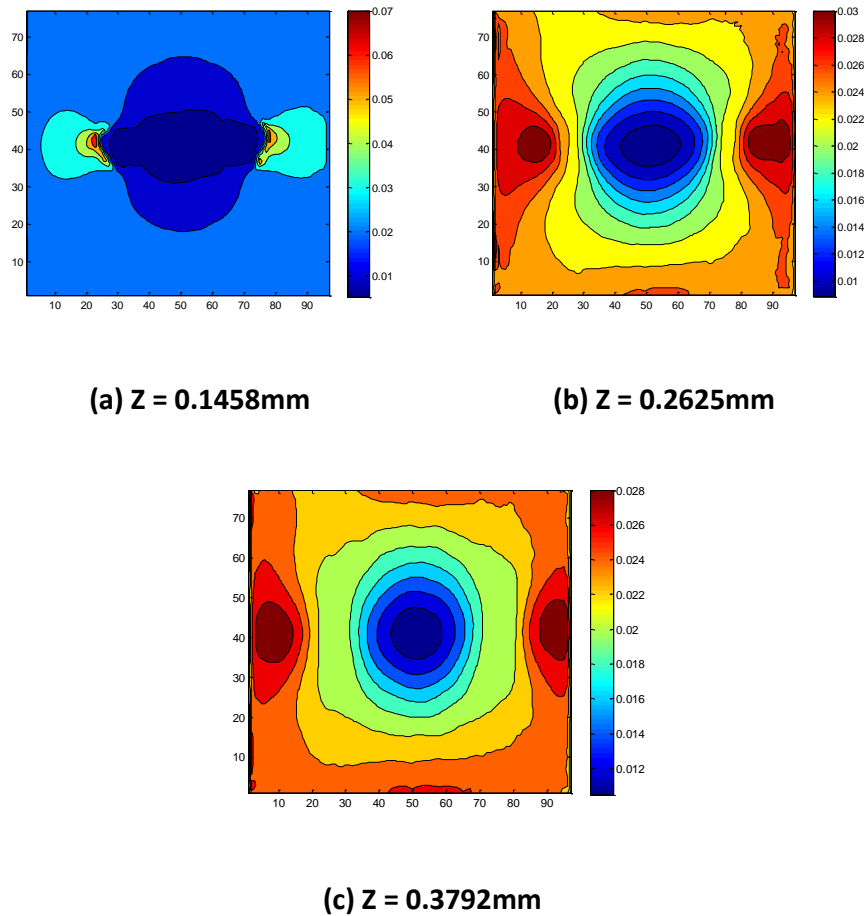
##### 5.3.1.1 Axial strain ( $\epsilon_{xx}$ ) for 0 degree sample

Figure 5.7 shows DIC strain results. The axial strain in fiber area is around 1.7% and in the strain concentration areas (red near fiber ends) is around 2.8%. The strain concentration area is away from low strain area inside fiber, which indicates this surface layer is above the inclusion in the specimen.



**Figure 5.7: DIC result for axial strain**

In Figure 5.8, the input wood particle properties for normal bulk wood (sample 1, modulus 8834MPa on longitudinal direction) were used and three layers are plotted from simulation results: The coordinate  $Z = 0.14583\text{mm}$  (close to inclusion),  $0.2625\text{mm}$ , and  $0.37917\text{mm}$  (close to sample surface). According to results, the axial strain in the fiber area is increasing as the coordinate increases because polymer modulus is relatively lower than the inclusion modulus. Because layer with coordinate  $z = 0.37917\text{mm}$  is close to sample surface and layer with coordinate  $z = 0.1458\text{mm}$  is close to inclusion, strain on stress concentration area is lower in the Figure 5.8c than Figure 5.8a. The strain concentration area is close to fiber ends in Figure 5.8a but away from fiber end in Figure 5.8c, which indicates layer with coordinate  $0.3792\text{mm}$  is closer to actual experimental sample surface. However, strain value in the



**Figure 5.8: Tension results of MPM simulation for axial strain with wood particle properties sample 1 (8834MPa). (a) Layer with coordinate 0.1458mm. (b) Layer with coordinate 0.2605mm. (c) Layer with coordinate 0.3792mm**

fiber area on the surface layer (coordinate 0.37917mm) is around 1.2%, which is lower than DIC strain value of 1.7%. This result suggests the inclusion modulus is lower than assumed here. The next plots try reducing the wood particle modulus and focus on surface plots.

Figure 5.9 shows axial strain simulation results using wood particle modulus sample 2 (longitudinal modulus 4417MPa), sample 3 (longitudinal modulus 2208MPa), and sample 5 (longitudinal modulus 1104MPa) in a layer with coordinate 0.3792mm. 1.8% to 2% axial strain was observed in the fiber area in Figure 5.9c. This is higher than DIC results which means properties of wood particle in the experiment are higher than sample 5.

Regardless of irregular contour lines of DIC result, both Figures 5.9a and b have similar

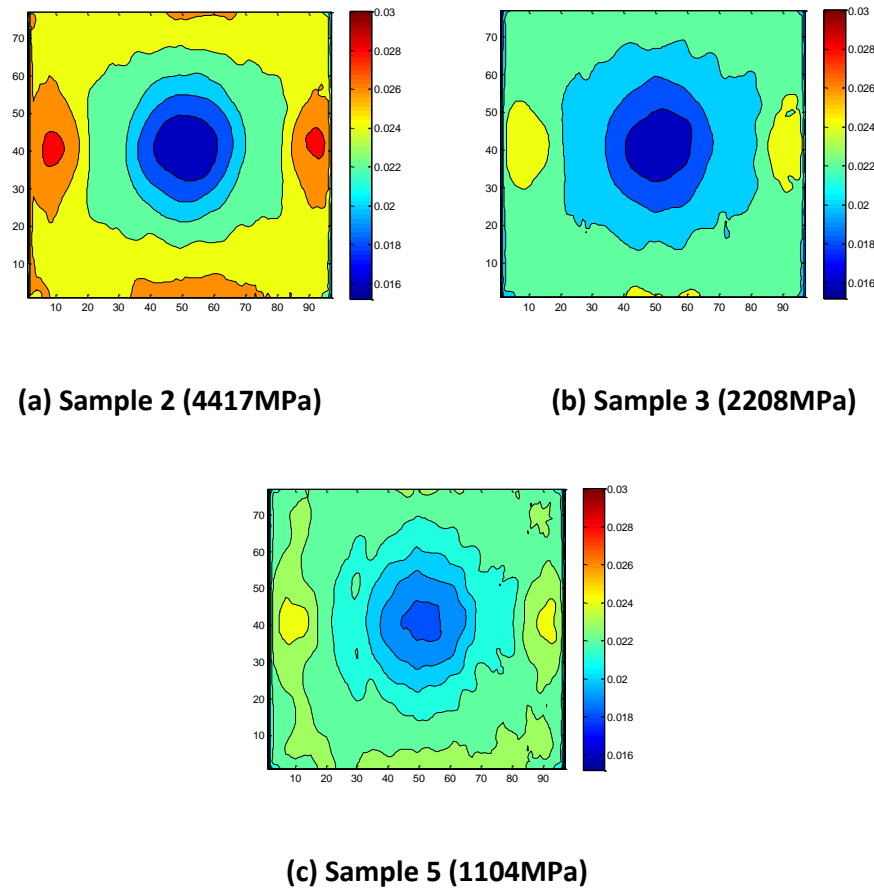


**Figure 5.9: Tension results of MPM simulation for axial strain in a layer with coordinate 0.3792mm (a) Inclusion property is sample 2. (b) Inclusion property is sample 3. (c) Inclusion property is sample 5.**



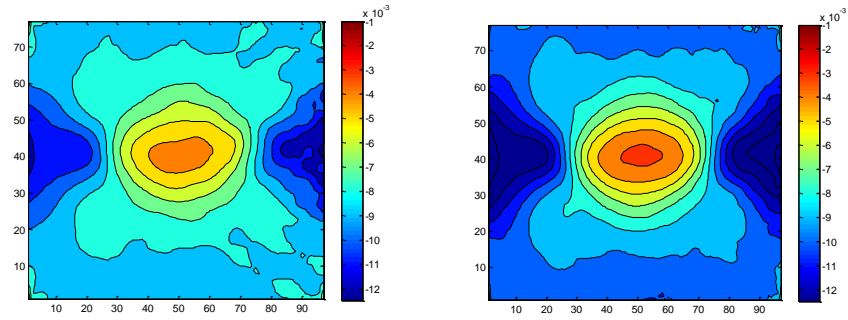
strain with DIC results in the fiber area, and the matrix strain in Figures 5.9a and b is around 2.3% which is close to 2% in the DIC result. Despite inaccurate location of strain concentration areas, we concluded the wood particle properties in samples 2 and 3 in the layer with coordinate  $z = 0.3792$  are the best matching to the DIC results. Differences in strain concentration area could be the effect of interface cracks in the experiment and MPM simulations lack interfacial crack methods in 3D models so far.

#### **5.3.1.2 Transverse strain ( $\epsilon_{yy}$ ) for 0 degree sample**

Figure 5.10 shows visual results for transverse strain for tangential tension using wood particle modulus sample 2 and sample 3 (longitudinal modulus 4417MPa and 2208MPa) in the layer with coordinate  $Z = 0.3792$ mm (Far away from inclusion). Both Figure 5.10a and Figure 5.10b show similar strain range with DIC (Figure 5.10c) result in the wood particle area. However, the distribution of strain is different, MPM simulation results show longer strain area in the x direction in the particle. The reason may be the absence of interfacial debonding in 3D MPM simulations. Another possibility is wood particle may not be parallel with the surface plane in the experiment which conflicts with assumptions of the MPM simulations.

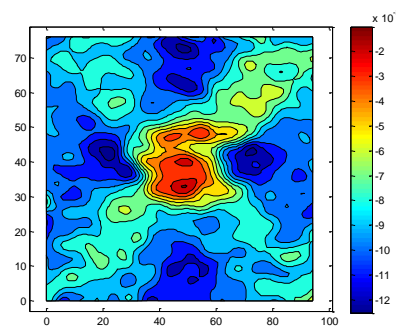
#### **5.3.1.3 Shear strain ( $\tau_{xy}$ ) for 0 degree sample**

Figure 5.11 shows results for shear strain using wood particle modulus from sample 2 and sample 3 (longitudinal modulus 4417MPa and 2208MPa) on layer with coordinate  $Z = 0.3792$  mm (far away from inclusion). The distribution of strain on DIC results is disorder, it may be caused by invalid calculations in DIC (Vic-2D 2009 software) or other optical artifacts (Lech Muszynski personal communication). The MPM simulation shows symmetric results for shear strain because the inclusion is in the centre of sample. The DIC and MPM have some features in common such as similar anti-symmetric strain distribution, but it was difficult to draw conclusions.



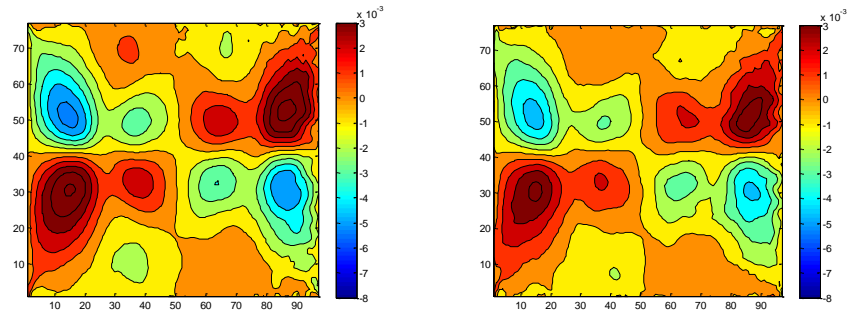
**(a) Sample 2 (4417MPa)**

**(b) Sample 3 (2208MPa)**



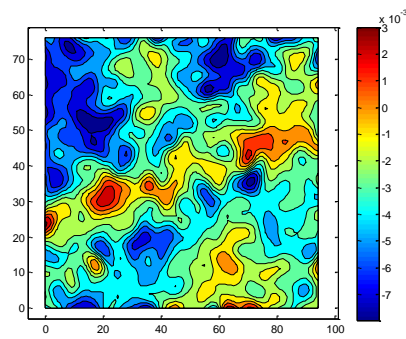
**(c) DIC**

**Figure 5.10: Tension results of MPM simulation for transverse strain with wood particle properties sample 2 and sample 3 (coordinate  $Z = 0.3792\text{mm}$ ). (a). transverse strain with inclusion property sample 2. (b). transverse strain with inclusion property sample 3. (c) DIC results for transverse strain**



(a) Sample 2 (4417MPa)

(b) Sample 3 (2208MPa)



(c) DIC

**Figure 5.11: Tension results of MPM simulation for shear strain in a layer with coordinate  $Z = 0.3792$ . (a). Shear strain with inclusion property sample 2. (b). Shear strain with inclusion property sample 3. (c) DIC results for shear strain**

### 5.3.2 90 degree Sample

This section is qualitative study for the 90 degree wood particle specimen.

#### 5.3.2.1 Axial strain ( $\epsilon_{xx}$ ) for normal mechanical property of inclusion on 90 degree sample

Figure 5.12 has DIC results for axial strain field. Because the wood particle is perpendicular, the modulus of wood particle x direction would be the transverse or radial modulus, which may be lower than the polymer matrix modulus (450MPa in MPM simulations). Therefore, the area in the fiber area shows higher strain than the area in the matrix (see Figure 5.12).

Figure 5.13 show results of transverse strain using wood particle properties for sample 1 (modulus 8834MPa on longitudinal direction of particle) with coordinates of  $Z = 0.1575$  mm (close to inclusion),  $z = 0.21$ mm and  $z = 0.35$ mm (far away from inclusion). Because the real position of wood particle is unknown, it is possible wood particle is closer to the surface in this specimen. Figure 5.13c shows results of layer with coordinate  $z = 0.1575$ mm. This layer is close to the inclusion, and its strain distribution contour is closest to DIC results, but still much less strain effect in the particle. The closest layer ( $Z = 0.1575$ mm) is used in subsequent plots because the effects are largest. It may not be correct, but can still be used to study how changing the particle properties changes the strain fields.

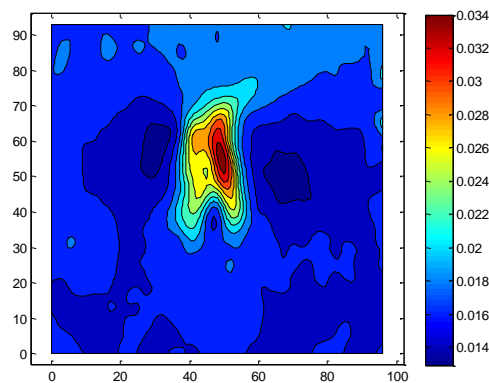
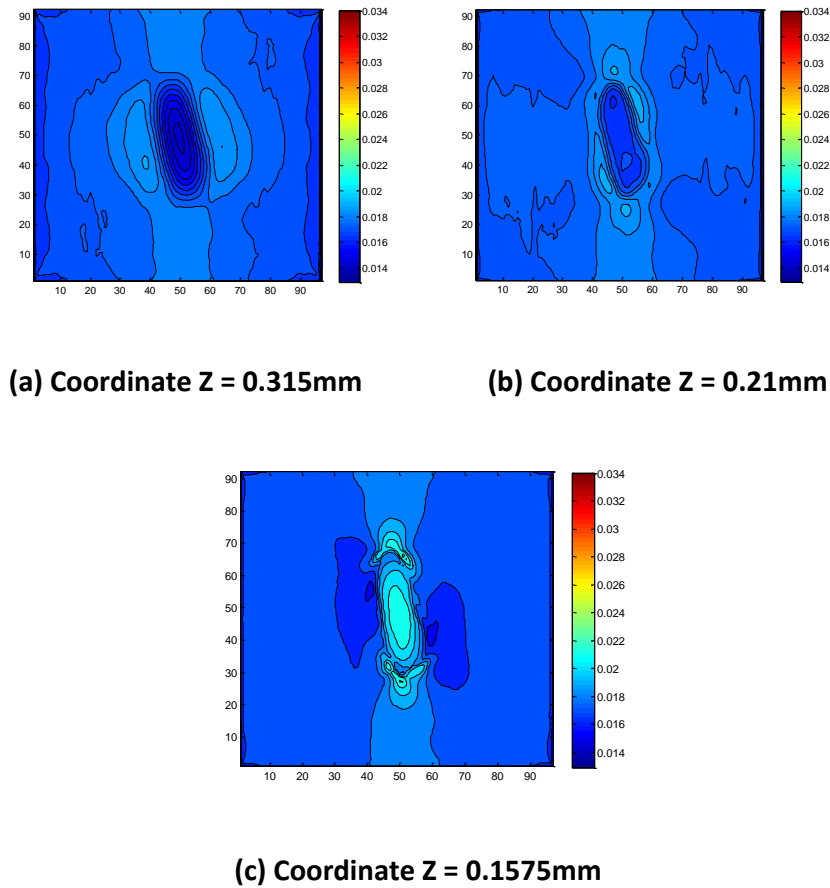


Figure 5.12: DIC results of axial strain



**Figure 5.13: Tension results of MPM simulation with wood particle properties sample 1 in different layer. (a) Layer with coordinate 0.315mm. (b) Layer with coordinate 0.21mm. (c) Layer with coordinate 0.1575mm**

Because wood particle area has relatively lower strain than matrix area in Figure 5.13c which is opposite with DIC result, here we used lower modulus sample 2 (longitudinal modulus 4417MPa) and sample 3 (longitudinal modulus 2208MPa) instead of sample 1. In the Figure 5.14a and b, although MPM results and DIC results have similar strain on matrix area, wood particle area has strain around 2% which is still too low compared to DIC results. The next sections varied other properties of the particles to look for better matching.

### 5.3.2.2 Yield strength study

There are a couple possibilities for the high strain inside the fiber in DIC results (Figure 5.12). First the wood cell wall is a elastic-plastic material and plastic failure could occur during the

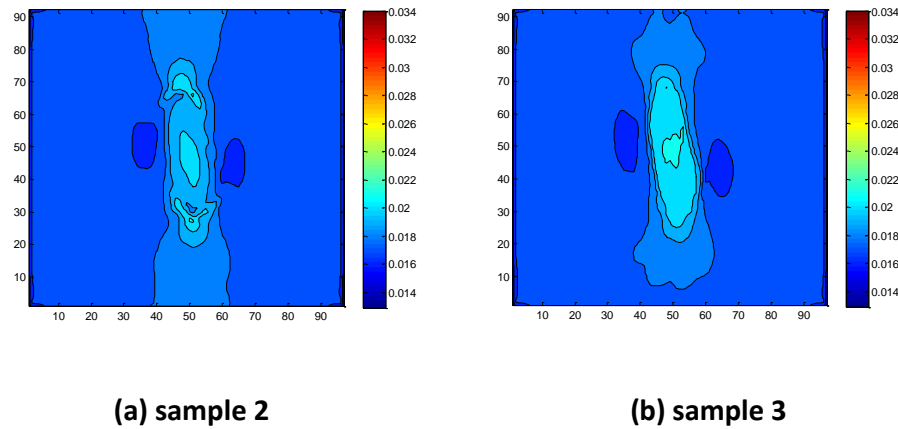


**Figure 5.14: Tension results of MPM simulation in a layer with coordinate Z = 0.1575mm. (a). Axial strain with inclusion property sample 2. (b). Axial strain with inclusion property sample 3**

loading process. Because we only varied modulus but not yield strength of wood particle, the simulation model could be different than the realistic wood structures. Thus, to simulate cell collapse by plastic deformation, the cell-wall material was assumed to be elastic-plastic (using the anisotropic plastic material described in section 5.2.2)

To explore an assumption of collapse by plastic deformation, we used different and lower yield strengths (see table 5.3) in the MPM simulations. Sample 8 assumed the wood particle is an elastic material with yield strength equal to infinity (no yielding in that direction). Samples 9 to 12 assumed various yield strength for the wood particle. All yield strengths for uniaxial tension in the material's x direction were set as infinity because wood has high yield strength in the longitudinal direction and it would not approach that criterion in our

**Table 5.3: Different yield strength with wood particle modulus the same as sample 3**

	yldxx(MPa)	yldyy(MPa)	yldzz(MPa)	yldxy(MPa)	yldyz(MPa)	yldxz(MPa)
sample 8	$\infty$	$\infty$	$\infty$	$\infty$	$\infty$	$\infty$
sample 9	$\infty$	5	5	6	2.5	6
sample 10	$\infty$	2.5	2.5	3	1.25	3
sample 11	$\infty$	1.25	1.25	1.5	0.625	1.5
sample 12	$\infty$	0.625	0.625	0.75	0.3125	0.75

experiments. Samples 8 to 12 used the same modulus as sample 3 at table 5.1 (longitudinal modulus 2208MPa) but with decreasing yield strengths.

Figure 5.15 shows the results of axial strain using different yield strength in a layer with coordinate  $z = 0.1575\text{mm}$ . Figure 5.16a is a simulation result for an elastic material ( $\infty$  yield

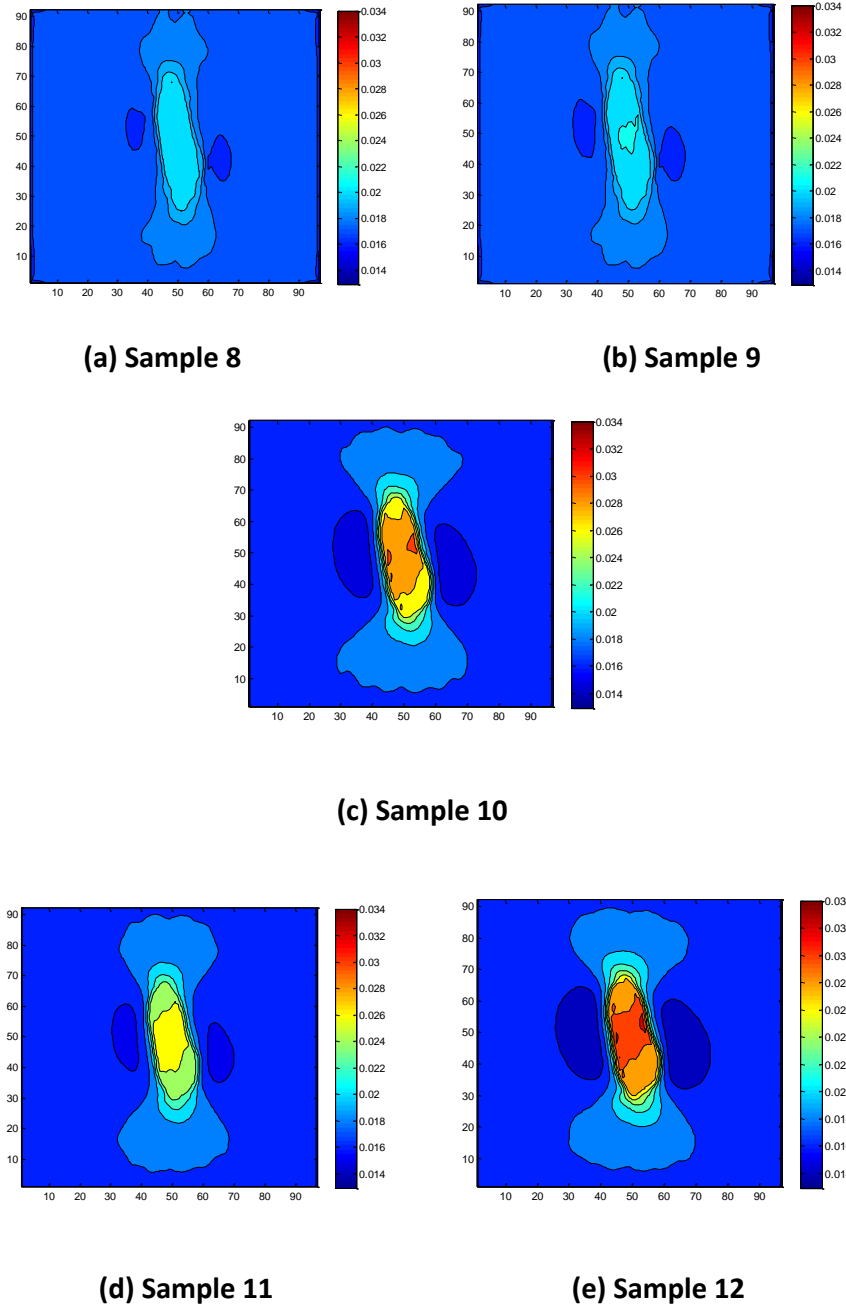


**Figure 5.15: Axial strain results of MPM tension simulation for different yield strength in a layer with coordinate  $Z = 0.1575\text{mm}$**

strength). Figures 5.16b, c, d, and e are simulation results as a function of decreasing yield strength. There were few differences between the elastic results (Figure 5.15a) and the Figure 5.15b's results, indicating that sample 9's yield strength was sufficiently high that deformation was dominated by elastic processes, rather than plastic failure. Figures 5.15c, d, and e show tension results with lower yield strength. The strain in the fiber area increased as yield strength of the wood particle decreased due to plastic strains. The stress at which plastic collapse occurred was approximately proportional to yield strength. Figure 5.15e has the closest axial strain in the wood particle area when compared to DIC results, which indicates the actual particle may have failed, be either plasticity or by fracture.

### 5.3.2.3 Transverse modulus study

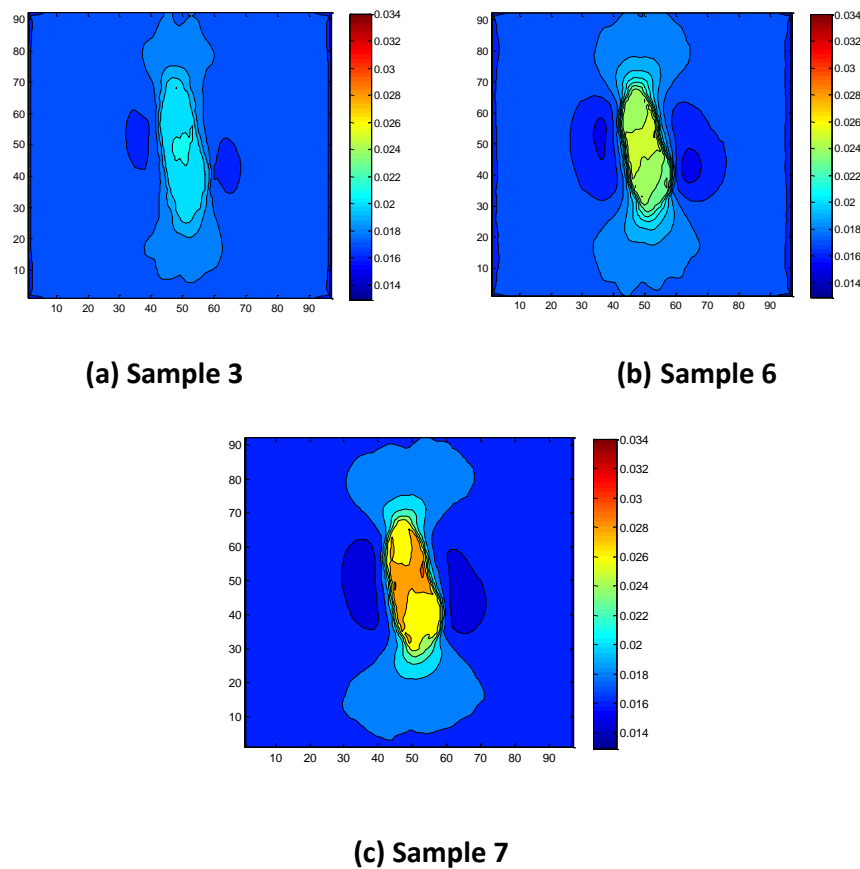
Another possibility is that damage to wood cell walls during processing of the particle results in very low mechanical properties, especially in the transverse direction. Thus relatively low transverse moduli (samples 6 and 7 at table 5.4) were used in MPM simulations and the results are show below. Sample 7's transverse moduli ( $E_{yy}$ ,  $E_{zz}$ , and  $G_{yz}$ ) are one half of sample 6 and one quarter of sample 3. Sample 3, sample 6, and sample 7 used the same yield strengths in table 5.2.

Figure 5.16 shows axial strain results of MPM tension simulation using different wood particle transverse moduli. For those low transverse modulus samples (Figure 5.16b and c), strain in fiber area is relatively higher than Figure 5.16a (normal transverse modulus). Figure 5.16c is the closest to the DIC result. Figure 5.16c represents results using sample 7, which

**Table5. 4: Different transverse modulus for wood particle**

	$E_{xx}$	$E_{yy}$	$E_{zz}$	$G_{xy}$	$G_{xz}$	$G_{yz}$
	(Mpa)	(Mpa)	(Mpa)	(Mpa)	(Mpa)	(Mpa)
Sample 3	2208	228	106	185	171	27
Sample 6	2208	114	53	185	171	13.5
Sample 7	2208	57	26.5	185	171	6.75





**Figure 5.16: Axial strain results of MPM tension simulation for different wood particle transverse modulus in a layer with coordinate  $Z = 0.1575\text{mm}$ . (a). Axial strain with inclusion property sample 3. (b). Axial strain with inclusion property sample 6. (c). Axial strain with inclusion property sample 7.**

has only one quarter transverse modulus of normal transverse modulus in sample 3 (longitudinal modulus  $2208\text{MPa}$ ).

After comparing low yield strength simulations and low transverse modulus simulation with DIC results, the conclusion is that both of them could simulate tension results for axial strain. Sample 12 (low yield stress) has the closest strain in the fiber area. However, both low yield strength model and low transverse modulus have different strain within the stress concentration area of the DIC results.

Another possibility is that the interface between the polymer and wood fiber played an important role in the tension results. MPM can simulate interfacial failure and it is available

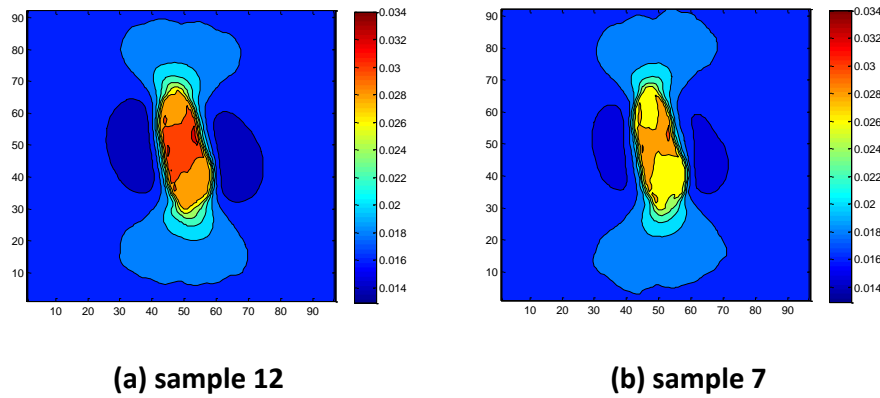


**Figure 5.17: Axial strain in a layer with coordinate  $Z = 0.1575$  mm**

**(a). low yield stress MPM simulation results; (b). low transverse modulus MPM simulation results**

in 2D calculations in the Nairn-MPM code (see Chapter 3). Unfortunately, interfacial effects are not yet available for the 3D calculations done here. 3D calculations with interface properties should be the subject of future work.

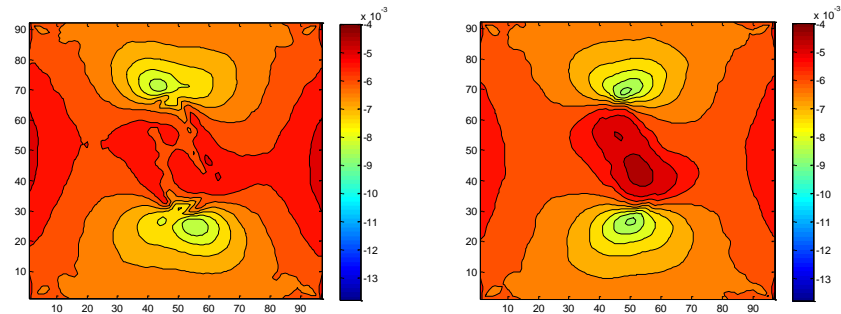
#### 5.3.2.4 Transverse strain ( $\epsilon_{yy}$ ) on 90 degree sample

In Figure 5.18, the DIC result (Figure 5.18c) of the transverse strain ( $\epsilon_{yy}$ ) is different from the simulations (Figures 5.18a and b) at the contour line, but they have similar angle at fiber strain area. Although MPM simulations (Figures 5.18a and b) and DIC experiment (Figure 5.18c) have similar transverse strain in the wood particle area (around 0.4%), Figures 5.18a and b show lower strain (0.6%) than Figure 5.19c (1.1%) on the matrix area. The reason could be absence of interface simulations, because it is x direction tension loading, the wood particle receives less compression in Y direction without interface.

#### 5.3.2.5 Shear strain ( $\tau_{xy}$ ) on 90 degree sample

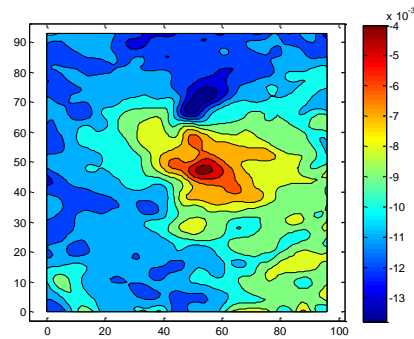
Because of some unknown DIC calculation methods for shear strain, the shear strain results by DIC are suspect. Figure 5.19, however, shows the MPM simulation and DIC agree reasonably well. One problem is that these plots used different scales. It was also noted that the average shear strain by DIC was not zero (it was about 0.4%) as it should be for a test

(and is in MPM simulations) under applied axial strain. More work is needed to find how DIC is determining shear strain.



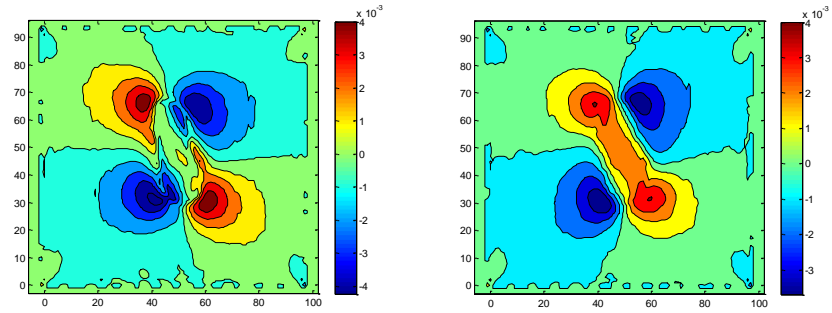
(a) sample 12

(b) sample 7



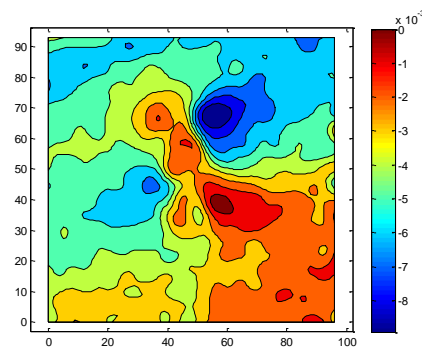
(c) DIC

**Figure 5.18: Transverse strain in a layer with coordinate  $z = 0.1575$  mm (a). low yield stress MPM simulation results; (b). low transverse modulus MPM simulation results.**



(a) sample 12

(b) sample 7



(c) DIC

Figure 5.19: Shear strain in a layer with coordinate  $z = 0.1575$  mm

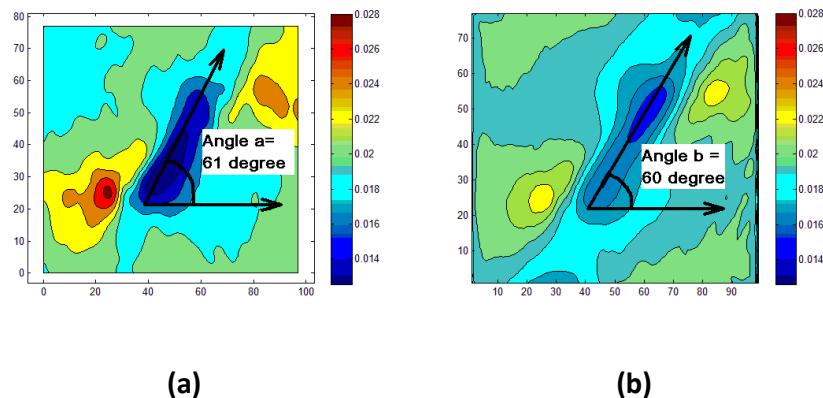
(a). low yield stress MPM simulation results; (b). low transverse modulus MPM simulation results

### 5.3.3 45 degree sample

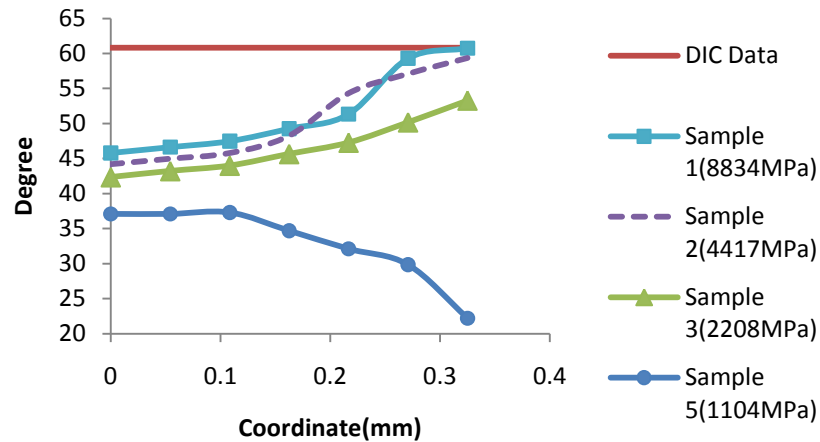
In the 45 degree experiment, the wood particle was oriented at an angle of about 45 degree with respect to the loading direction, but the DIC axial strain results shows a strain reducing zone with an angle higher than 45 degree (see Figure 5.20a).

Figure 5.20a shows the angle between wood particle strain area and the x axis (loading direction) on DIC strain results. The preliminary hypothesis was that the angle of low strain area changes with z coordinate and DIC is seeing the angle on the surface. In order to find the relationship between fiber strain angle, wood particle modulus, and plane position on coordinate system, three samples (Table 5.1) were simulated by MPM from coordinates  $z = 0\text{mm}$  to  $z = 0.325\text{mm}$ .

Figure 5.21 shows visualization results for wood particle strain area that relate with increasing layer coordinate  $Z$ . The angle of strain area increased as coordinate  $Z$  increased. Figures 5.21a and b are for layers containing wood particle. The angles in these two Figures are around 45 degree, which is close to the wood particle angle. The angles in Figures 5.21c and d (layers far away from inclusion) are higher, which indicates the effect of high modulus wood particle on strain field orientation as the  $z$  coordinate increases.



**Figure 5.20: Example of measured angle of wood particle area, (a) DIC axial strain result. (b) One MPM axial strain simulation result.**



**Figure 5.22: Fiber strain angle changes with fiber modulus. The solid circle, solid triangle, broken line, solid squares, and solid line indicate sample 5 (longitudinal modulus 1104MPa), sample 3 (longitudinal modulus 2208MPa), sample 2 (longitudinal modulus 4417MPa), sample 1 (longitudinal modulus 8834MPa), and DIC result.**

**Figure 5.21: Relationship between angles of wood particle axial strain area with layer coordinate Z (wood particle property is sample 1). (a). Angle In a layer with coordinate 0mm. (b). Angle In a layer with coordinate 0.1083mm. (c). Angle In a layer with coordinate 0.2166mm. (d). Angle In a layer with coordinate 0.325mm.**

Figure 5.22 shows how the angle of the wood particle strain area changes with Z coordinate and wood particle modulus. The x axis is the z coordinate, coordinate  $z = 0$  indicates the center layer of the specimen and coordinate  $z = 0.325$  indicate the top layer of the specimen.

The solid line shows the angle of DIC inclusion strain area, which is close to 61 degree. The angle of inclusion strain area on sample 1, sample 2, and sample 3 increased when coordinate Z increased, which indicated the effect of relatively high modulus wood particle on axial strain is lower on layers far away from fiber than on layers containing or close to the fiber. For sample 1 (longitudinal modulus 8834MPa), angle changed from 45 degree on layer with coordinate  $z=0.00$  to 60 degree on layer with coordinate  $z = 0.325$ , which is quite close to the 61 degree from DIC results so that layer with coordinate  $Z = 0.325$  could be the

surface of experimental specimen and sample 1 is close to property of wood particle in the experiment.

Because sample 1 has longitudinal wood particle modulus 8834MPa which is higher than former assumptions for horizontal and vertical wood particle simulations, a possible conclusion is that wood particle in this specimen could be latewood but while particles in horizontal and vertical particle tension experiment are earlywood.

In spite of both Figure 5.22d and Figure 5.21a having the same angles of inclusion strain area, the strain in the strain area in Figure 5.22d is higher than DIC results (Figure 5.21a). Imprecise and unstable DIC results could be one factor. Another factor is wood particle could have angle with x-y plane in the experiment, which differs from our assumption that longitudinal direction of wood particle is parallel to x-y plane.

The solid line on the top is DIC results on the surface. For low modulus particle (sample 5) the angle decreases. But for all higher moduli, the angle increases. We can conclude the wood particle modulus must be 2208MPa or higher. For any high modulus, the angle eventually equals to the experimental result. Furthermore, if the modulus of the particle was known, the angle of the strain area could be used to measure the distance between the inclusion and the surface. All we can say here is that if the wood modulus is between 2208MPa and 8834MPa, the surface was between 0.25mm and about 0.4mm.

## 5.4 Conclusions

The results in this chapter demonstrated the capability of the material point method (MPM) to model an anisotropic material (wood particle) embedded in a polyethylene matrix. It is possible to discretize a micrograph of a wood particle embedded in a matrix into an MPM model. By varying properties of the wood particle and selecting different layers, one can compare strain fields from MPM simulation results to experimental results (DIC) to find best matching conditions. By qualitative comparison, we could deduce that the *in situ* properties of wood particles are lower than bulk wood. From the 90 degree specimen, the particle may contain initial flaws or be prone to transverse failure. From the 45 degree specimen, we could use the change of the strain fields to deduce 3D geometric properties of the specimen.

## CHAPTER 6: WPC QUANTITATIVE ANALYSIS

### 6.1 Introduction

This chapter is similar to the quantitative analysis section of chapter 4. The difference is the work is using anisotropic material wood particle instead of copper wire. 0 degree particle, 45 degree particle, and 90 degree wood particle specimens were imported to 3D MPM simulations. In 3D simulations, we did quantitative comparisons for axial strain ( $\epsilon_{xx}$ ), transverse strain ( $\epsilon_{yy}$ ), and shear strain ( $\tau_{xy}$ ). The quantitative comparisons used Matlab software as the analysis tool.

### 6.2 Materials and Methods:

The specimen was described in Chapter 5, section 5.2.1. The Matlab importing methods were the same as use for the copper validation study in chapter 4. In 3D MPM simulations, the wood particle was defined as elastic-plastic material based on an orthotropic material.

Tables 6.1 to 6.4 give the wood particle properties used in this chapter. The different directions for the material axis were as described in Chapter 5. Table 6.1 shows the orthotropic moduli used for the simulations. All moduli were scaled by a constant ratio while keeping Poisson ratios constant ( $\gamma_{xy} = 0.27595$ ,  $\gamma_{xz} = 0.34858$ ,  $\gamma_{yz} = 0.7089$ ). Sample 2 is based on bulk wood; the others are scaled to lower values (except Sample 1). The density of all samples was  $0.39 \times 10^3 \text{ kg/m}^3$ .

Table 6.2 give the wood particle yield strengths used for samples 1 to 17.

Table 6.3 shows the modulus of wood particles when it was assumed there was a relatively lower transverse modulus. Samples 8 to 12 used 1/2 transverse modulus ( $E_{yy}$ ,  $E_{zz}$ ,  $G_{yz}$  are half of normal values in table 6.1). Samples 13 to 17 used 1/4 transverse modulus ( $E_{yy}$ ,  $E_{zz}$ ,  $G_{yz}$  are quarter of normal values in table 6.1).

Table 6.4 shows properties with lower yield strength samples with wood particle modulus from sample 1 to sample 7 in table 6.1.



**Table 6 1: Wood particle modulus on different sample**

<b>Material properties</b>							
	Density	Exx	Eyy	Ezz	Gxy	Gxz	Gyz
	(10 <sup>3</sup> kg/m <sup>3</sup> )	(Mpa)	(Mpa)	(Mpa)	(Mpa)	(Mpa)	(Mpa)
Sample 1	0.39	17668	1826	850	1486	1372	216
Sample 2	0.39	8834	913	425	743	686	108
Sample 3	0.39	4417	456	212	371	343	54
Sample 4	0.39	2208	228	106	185	171	27
Sample 5	0.39	1656	171	80	139	128	20
Sample 6	0.39	1104	114	53	92.5	85.5	13.5
Sample 7	0.39	552	57	26.5	46.25	42.75	6.75

**Table 6 2: Yield strength used from sample 1 to sample 17**

	yldxx	yldyy	yldzz	yldxy	yldyz	yldxz
	(MPa)	(MPa)	(MPa)	(MPa)	(MPa)	(MPa)
Sample 1-17	∞	5	5	6	2.5	6

**Table 6 3: Modulus of Low transverse modulus sample**

	Exx	Eyy	Ezz	Gxy	Gxz	Gyz
	(Mpa)	(Mpa)	(Mpa)	(Mpa)	(Mpa)	(Mpa)
Sample 8	8834	456.5	212.5	743	686	54
Sample 9	4417	228.25	106.25	371	343	27
Sample 10	2208	114	53	185.5	171	13.5
Sample 11	1104	57	26.5	92.5	85.5	6.75
Sample 12	552	28.5	13.25	46.25	42.75	3.375
Sample 13	8834	228.25	106.25	743	686	27
Sample 14	4417	114	53	371	171	13.5
Sample 15	2208	57	26.5	185.5	171	6.75
Sample 16	1104	28.5	13.25	92.5	85.5	3.375
Sample 17	552	14.25	6.625	46.25	42.75	1.6875

**Table 6 4: Different yield stress with wood particle modulus from sample 1 to sample 7 on table 6.1**

	yldxx	yldyy	yldzz	yldxy	yldyz	yldxz
	(MPa)	(MPa)	(MPa)	(MPa)	(MPa)	(MPa)
sample 18	$\infty$	5	5	6	2.5	6
sample 19	$\infty$	1.25	1.25	1.5	0.625	1.5
sample 20	$\infty$	0.625	0.625	0.75	0.3125	0.75

According to damping study in chapter 2, we again used “feedback damping =  $5000(1/mm^2)$ ”. According to quantitative analysis results in chapter 4, a small region inside the wood particle area was analyzed. The method for quantitative comparisons was the same as in Chapter 4, section 4.2.5. The deviation error equation is:

$$dev \mathcal{E}2 = devError2(\%) = \sqrt{\frac{\sum_{i,j=0}^n ((D_{ij} - \bar{D}_{ij}) - (M_{ij} - \bar{M}_{ij}))^2}{\sum_{i,j=0}^n D_{ij}^2}}$$

$$= \sqrt{\frac{\sum_{i,j=0}^n ((D_{ij} - M_{ij}) - (\bar{D}_{ij} - \bar{M}_{ij}))^2}{\sum_{i,j=0}^n D_{ij}^2}}$$

$$D = DIC \text{ strain Data} \quad M = MPM \text{ strain Data}$$

Here  $\bar{D}_{ij}$  is mean value of DIC strain data on region selected;  $\bar{M}_{ij}$  is mean value of MPM strain data on region selected;  $dev\mathcal{E}2$  is deviation error 2.

## 6.3 Results and Discussion

### 6.3.1 0 Degree Specimen Deviation Error

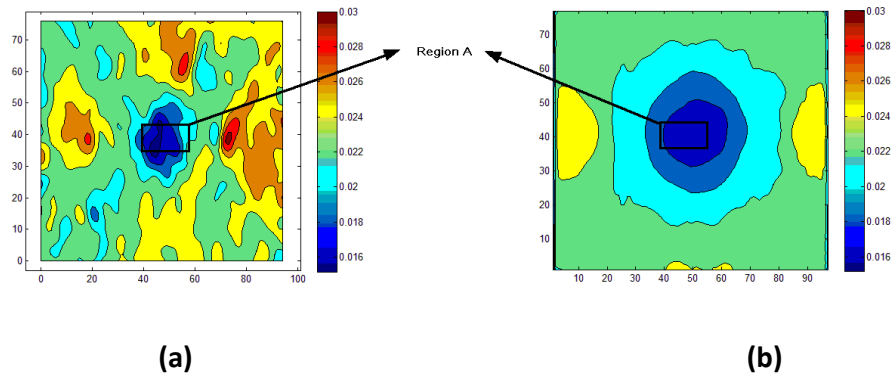


**Figure 6.1: Visualization result of axial strain on 0 degree study. (a)DIC results (b) one MPM simulation results**

According to quantitative analysis results in chapter 4, the best approach is to focus on a small region inside the wood particle area. For the 0 degree specimen, the region is shown in Figure 6.1. Figure 6.1a is DIC axial strain in the 0 degree specimen by DIC experiment and Figure 6.1b is MPM simulation at same applied load. The Region A size was  $22 \times 9$  elements.

Figure 6.2 shows axial strain results of deviation error in Region A for layers in coordinate  $Z = 0.2334$  and  $0.35\text{mm}$ . Wood particle properties used here are from sample 2 to sample 7 in table 6.1. These layers appear to have a minimum deviation error around 10% when the wood particle property is sample 5 (longitudinal modulus  $1656\text{MPa}$ ). The total error on the surface layer (plane 2) was lower than plane 1, which was closer to the particle. We concluded that the surface layer at  $Z = 0.35\text{mm}$  is the closest actual layer for the experiments and that inclusion property sample 5 is closest to wood particle properties. Notably, the *in situ* wood particle modulus is much lower than bulk wood. Furthermore, the minimum at low modulus agrees with qualitative results in Chapter 5 that needed reduced modulus for better plots.

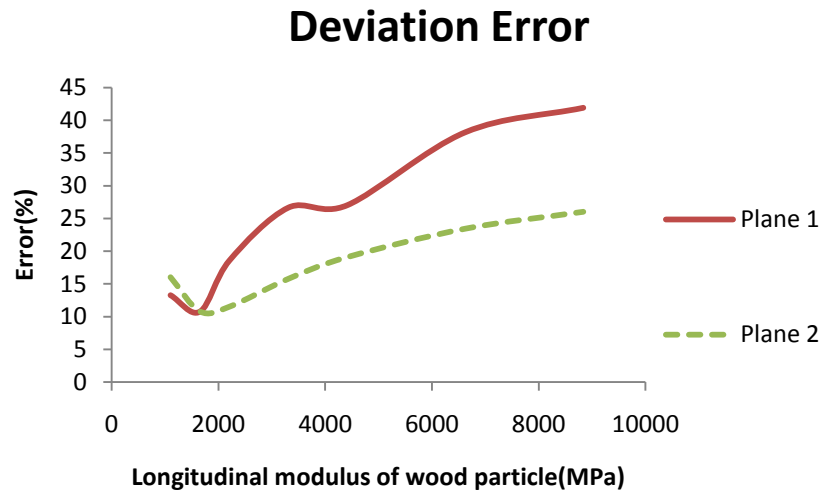


**Figure 6.2: Axial strain ( $\epsilon_{xx}$ ) deviation error of Region A in two layers. Layer 1 is indicated with coordinate  $Z = 0.2334\text{mm}$ ; Layer 2 is indicated with coordinate  $Z = 0.35\text{mm}$ .**

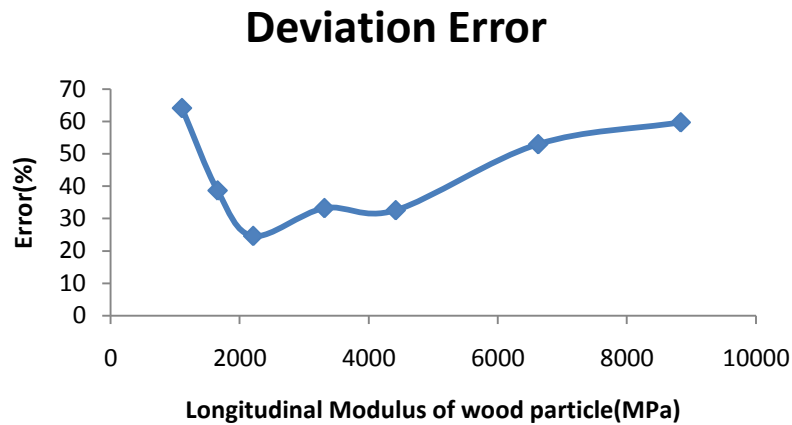


**Figure 6.3: Transverse strain ( $\epsilon_{yy}$ ) deviation error of Region A on layer with coordinate  $Z = 0.35\text{mm}$ .**

Figure 6.3 shows transverse strain results for the deviation error over Region A on the surface layer with coordinate  $Z = 0.35\text{mm}$ . Wood particle properties used here were from sample 2 to sample 7 (see Table 6.1). This Figure shows similar results with axial strain results of layer with coordinate  $0.35\text{mm}$  on Figure 6.2, but here sample 4 (wood particle longitudinal modulus  $2208\text{MPa}$ ) has the minimum error (around 20%). Because the transverse strain may be affected by interfacial properties and we did not model the interface in the MPM simulations, one might consider the axial strain analysis is to be more accurate. But, both results show a low wood particle modulus compared to bulk wood.

Figure 6.4 shows the shear strain results for deviation error over Region A in the surface layer with coordinate  $z = 0.35\text{mm}$ . Wood particle properties used here are from sample 2 to sample 7 (See table 6.1). Although shear strain results also shows sample 5 (wood particle longitudinal modulus  $1656\text{MPa}$ ) has minimum error, the overall error was large (around 52%). The reason may be related to DIC artifacts for shear strain.

In summary, according to axial, transverse, and shear strain analysis results, the specimen in the 0 degree particle study could have mechanical properties close to sample 5 (longitudinal modulus around  $1656\text{MPa}$ ) and the layer with coordinate  $z = 0.35\text{mm}$  is close to the surface layer for the actual specimen.

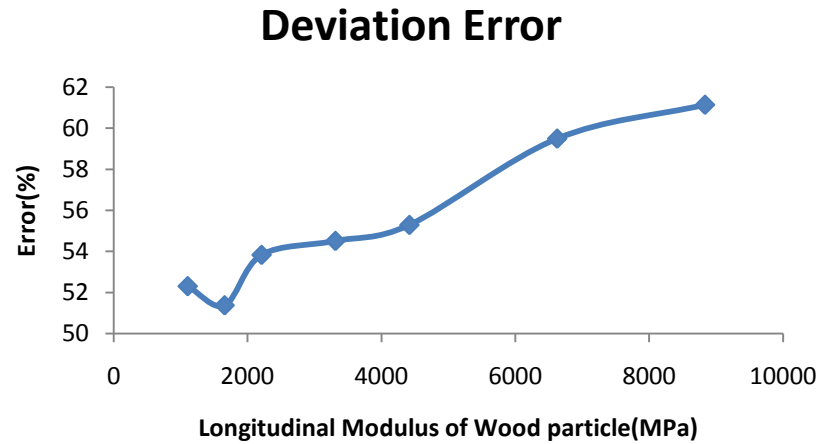


**Figure 6.4:** Shear strain ( $\tau_{xy}$ ) deviation error of Region A on layer with coordinate Z = 0.35mm.

#### 6.3.2 90 Degree Specimen Deviation Error

A small region inside the wood particle area was analyzed for quantitative comparisons. For the 90 degree specimen, the region is shown in Figure 6.5. Figure 6.5 is a visualization result of axial strain on 90 degree study for DIC experiment and MPM simulation. In this Figure, the small region B was taken for deviation error calculation. Region B covered area of 0.3170×0.1918 mm, and resolution of region B is 14×8 elements.

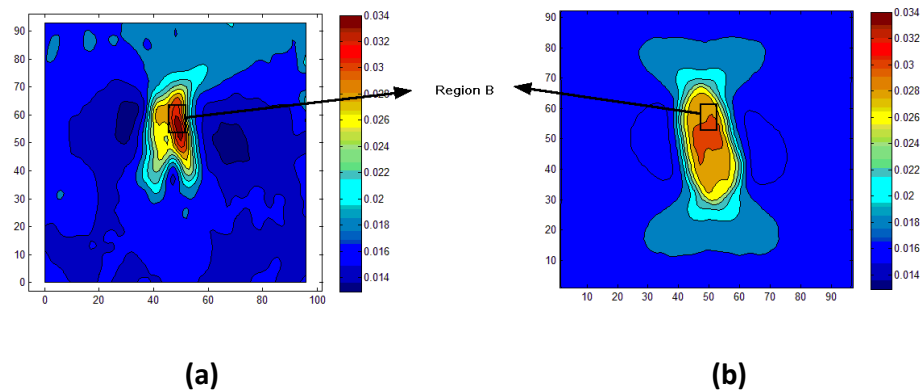


**Figure 6.5:** Visualization result of axial strain on 90 degree study. (a)DIC results (b) one MPM simulation results.

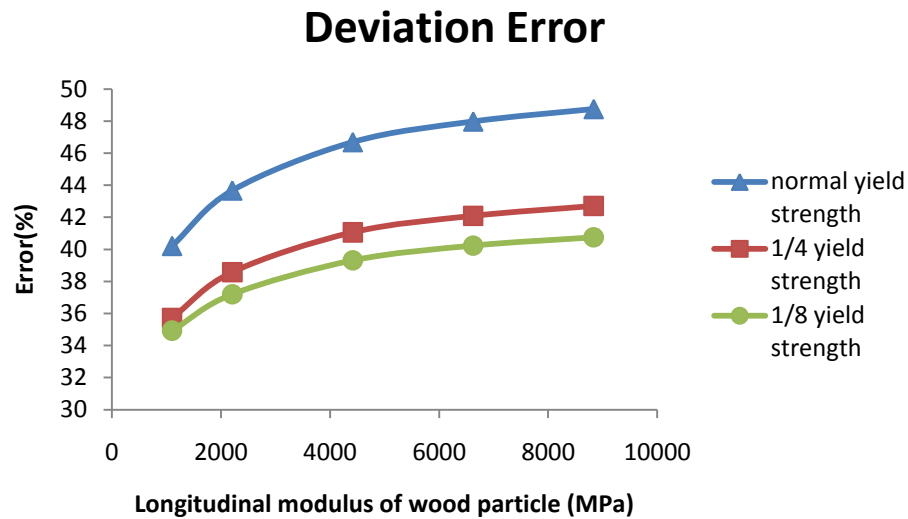


**Figure 6.6: Deviation error for 90 degree MPM simulation results for axial strain with different wood particle yield strength (Layer with coordinate  $z=0.315\text{mm}$ ). Here wood particle modulus is the same as sample 2 to sample 6 in table 6.1 but with different yield strength property (table 6.4). Triangle, square, and circle were indicated with normal yield strength (sample 18), 1/4 yield strength (sample 19), and 1/8 yield strength (sample 20).**

From Chapter 5, it was concluded this wood particle cracked, but could be simulated by using reduced yield strength or reduced transverse modulus for the particle properties. Figure 6.6 shows effect of wood particle yield strength on the deviation error. The normal yield strength (triangle) has high error (above 40%). However, the error got lower as yield strength decreased (square and circle). Unfortunately, no minimum could be found in this plot, but the error decreased in the lower modulus region.

Figure 6.7 shows effect of wood particle transverse modulus on the axial strain deviation error. Here wood particle moduli  $E_{xx}$ ,  $G_{xy}$ , and  $G_{xz}$  remained constant but  $E_{yy}$ ,  $E_{zz}$ , and  $G_{yz}$  were reduced to be half or quarter to get new material properties (samples 12 to 17 in table 6.2). This plot is similar to low yield strength plot (Figure 6.6). The normal transverse modulus (triangle) has high error (above 40%). The error got lower as transverse modulus decreased (square and circle). Like Figure 6.6, no minimum could be found in this plot.

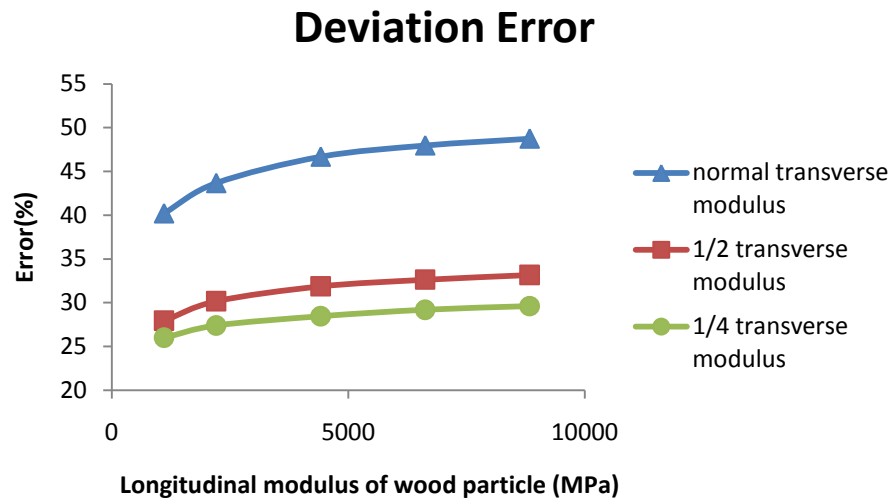
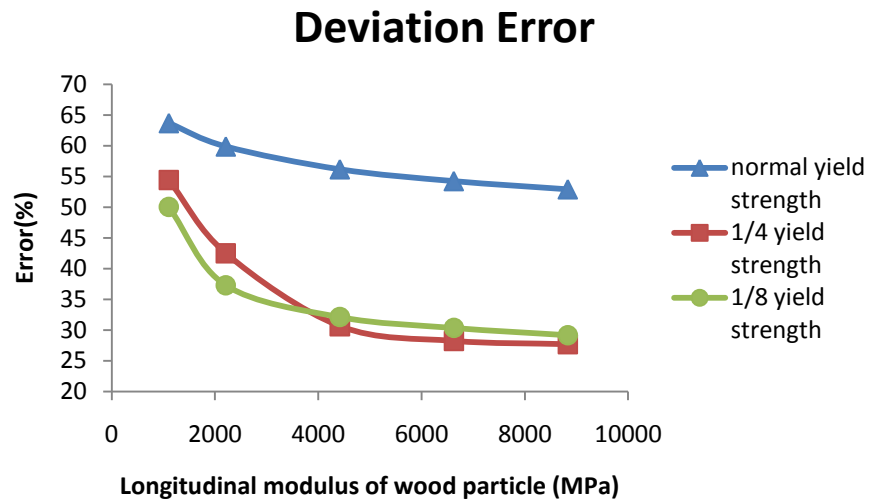


**Figure 6.7: Deviation error for 90 degree MPM simulation results of axial strain with different wood particle transverse modulus (Layer with coordinate  $z=0.315\text{mm}$ ). Triangle, square, and circle are indicated with normal transverse modulus (samples 2 to 6); 1/2 transverse modulus (samples 8 to 12), and 1/4 transverse modulus (samples 13 to 17).**

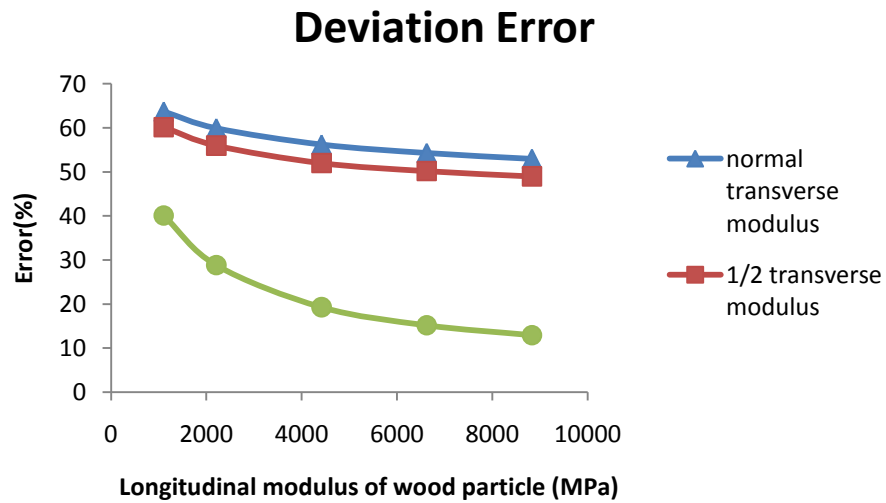
Figure 6.8 shows that effect of transverse yield strength or modulus on wood particle transverse strain deviation error. The yield strength and transverse modulus have powerful effect on the deviation error. The average error between normal sample and 1/4 yield strength sample decreased about 30%, and the average error between normal transverse sample and half transverse sample decreased about 2%. The difference between axial strain and transverse strain results is that transverse modulus are more effective than yield strength on axial strain results but less effective on transverse strain results, the reason may be the absence of interfacial modeling in MPM 3D simulations.

There were unusually large deviation errors for the shear strain, which may be due to unknown DIC calculation methods for shear strain or optical artifacts. Therefore, the shear strain deviation error was not analyzed here.





(a)



(b)

**Figure 6.8: Deviation error for transverse strain. (Layer with coordinate  $z=0.315\text{mm}$ ).**  
**(a) Deviation error for transverse strain with different wood particle yield strength.**  
**(b) Deviation error for transverse strain with different wood particle transverse modulus.**

In summary, no minima were found for the 90 degree specimen. All that could be determining was that the wood particle had likely failed, because it was modeled best with low yield strength and/or low transverse modulus.

### 6.3.3 45 Degree Specimen Deviation Error

A small region inside wood particle area was analyzed for quantitative comparisons. For the 45 degree specimen, the region is shown in Figure 6.9. Figure 6.9 is a plot of axial strain in the 45 degree study by DIC experiment and by MPM simulation. In this Figure, region C was taken for deviation error calculation. The resolution of region C is  $14 \times 8$  elements. Region C covered an area of  $0.315 \times 0.1904$  mm.

Figure 6.10 shows 45 degree deviation error results for axial strain over region C in the surface layer with coordinate  $Z = 0.325$  mm using wood particle properties samples 1 to 6 (see table 6.1). The deviation error decreased as wood particle modulus increased, even for wood particle longitudinal modulus up to 17000 MPa. However, the modulus of wood particle cannot be that high. The reason may be the same as the copper wire study in chapter 4. The effect of the inclusion modulus is small in a layer far away from the inclusion when the modulus of inclusion is much higher than the polymer matrix.

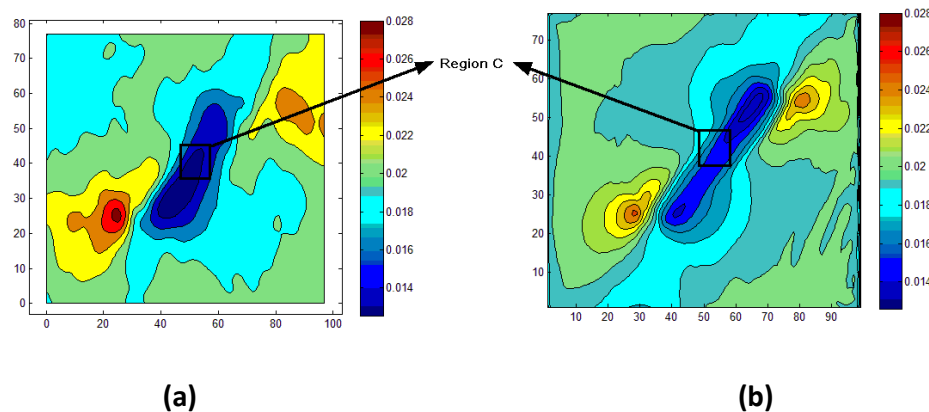


**Figure 6.9: Visualization result of axial strain on 45 degree study. (a)DIC results (b) one MPM simulation results.**

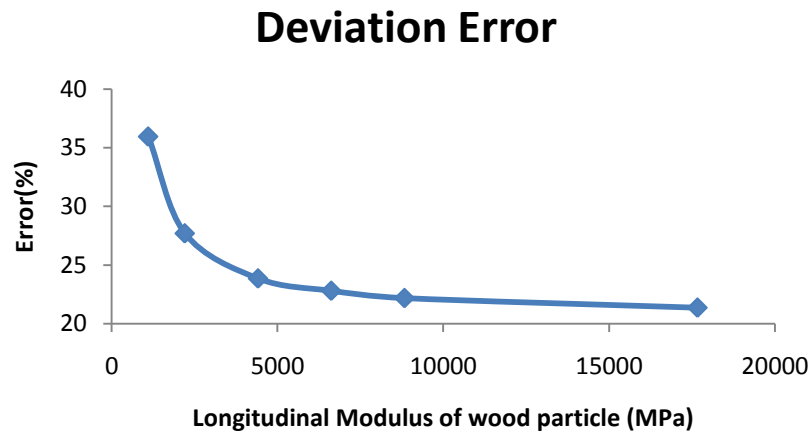


**Figure 6.11: 45 degree axial strain deviation error of Region C in a layer with coordinate  $Z = 0.325\text{mm}$ .**

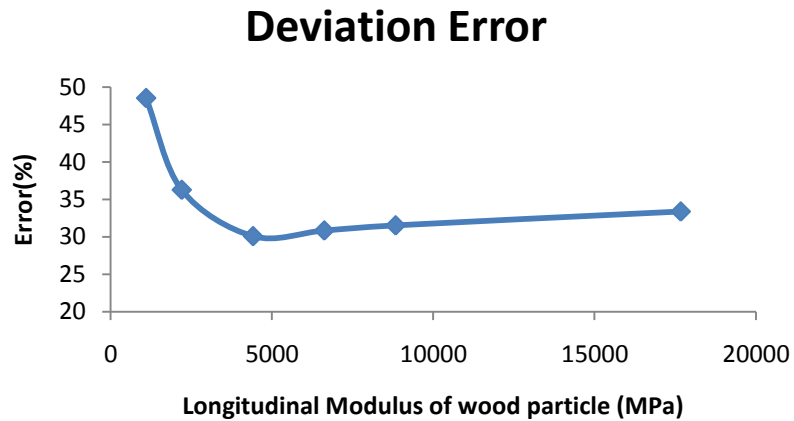


**Figure 6.10: 45 degree transverse strain deviation error of Region C in a layer with coordinate  $Z = 0.325\text{mm}$ .**

Figure 6.11 shows the 45 degree deviation error results for transverse strain over region C in the surface layer with coordinate  $Z = 0.325\text{mm}$  using wood particle properties samples 1 to 6 (see table 6.1). The sample 3 (longitudinal modulus 4417MPa) has a slight minimum error value (30%).

Figure 6.12 shows the 45 degree deviation error results for shear strain over region C in the surface layer with coordinate  $Z = 0.325\text{mm}$  using wood particle properties samples 1 to 6

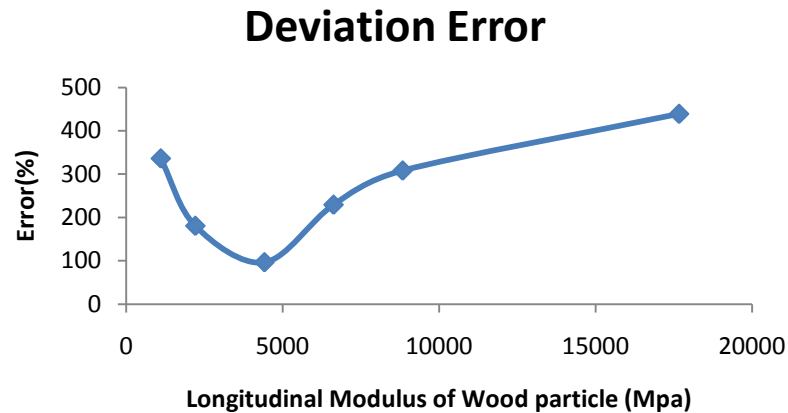


**Figure 6.12: 45 degree shear strain deviation error of Region C in a layer with coordinate Z = 0.325mm.**

(see table 6.1). The sample 3 (longitudinal modulus 4417MPa) has a strong minimum error value. However, the total error in this Figure is large because of possible DIC artifact for shear strain.

According to transverse and shear strain analysis results, the experimental wood particle in the 45 degree particle study could have a modulus similar to sample 3 (longitudinal modulus 4417MPa), but the exact value is hard to get because the axial strain results did not work and shear strain had high absolute errors.

#### 6.4 Conclusion

For the 0 degree, 90 degree, and 45 degree wood particle specimens, quantitative analysis can estimate mechanical properties of *in situ* wood particle. It is concluded that MPM research has capabilities for simulation with inclusions embedded in a polymer matrix structure using three dimensional models when inclusion modulus is within a limit.

Compared to qualitative analysis, quantitative can concentrate on a small area and get more exact results. In the 90 degree particle quantitative analysis study, MPM simulations are demonstrated as having potential for tracking the structure of wood particles during failure. The entire approach, however, is not very robust. We can get some results for mechanical

properties, but it does not seem possible to extract all anisotropic properties from a few DIC tests, as some researchers have proposed.

## CHAPTER 7: CONCLUSION AND FUTUREWORK

This thesis has demonstrated that the material point method (MPM) can handle large-scale, morphology-based models of copper-polymer composites and wood plastic composites. In this research, numerical models were built by Material Point Method (MPM) to obtain strain and stress results of copper-polymer composites and wood polymer composites which were used to compare with DIC results for interpretation of results. The following is a summary of the conclusions and further work suggested by this research:

### 1. Literature review:

(a). Polymeric composites reinforced with bio-materials have many advantages and are widely used in the U.S. WPCs were chosen in this study because they represent the largest share of the current bio-based composites market and because they could benefit substantially by new science on mechanics of natural-particle reinforcement. Moreover, WPCs have similar manufacturing processes, and face similar issues, as other bio-based composites.

(b). Extensive research has been conducted to model isotropic materials such as metal and polymers but few studies have been conducted to model anisotropic materials such as wood. And the exact mechanisms behind the effects of the inclusion geometry on the composite micro-mechanics remain unclear.

(c). In many studies, the wood/polymer interaction was discussed from the chemical point of view and mechanical interlocking which is commonly considered a major mechanism in adhesion. An appropriate tool is needed to model the interface of wood/polymer in 2D models and in 3D models.

2. From the qualitative comparisons and quantitative comparisons for strain results of DIC to material point method (MPM), the following conclusions were drawn:

- (a). MPM modeling could be used to interpret experimental results, to extract material properties of wood/copper fiber and polymer matrix in composites, and to develop interface simulations for copper/polymer composite in 2D MPM models. This work is not limited to 0 degree experiments (inclusion is parallel to loading direction); it could model any angle conditions. Analysis of real experiments required 3D MPM models.
- (b) It is easy to discretize a micrograph of copper/polymer composite and wood plastic composite into a 2D MPM model and possible to extend it to a 3D model of wood plastic composites. In 3D the WPC specimen was assumed to be divided into many slices. Each slice could be digitized into a plane of the model analogous to the methods used here for a single 2D image. A collection of slices would be assembled into a 3D model.
- (c). Because it is hard to get mechanical properties of tiny wood particle, qualitative and quantitative analysis (deviation error calculation) can be used to find their *in situ* properties. Once discretized MPM calculations are very stable, MPM model can be carried out to large deformations, can include elastic-plastic properties, and can automatically model contact between polymer and wood particle.

In summary, MPM is a promising and effective method for two dimensional and three dimensional *in situ* examination and morphological characterization of WPCs and other heterogeneous composites of similar composition.

### 3. Further work:

Interface in 2D experiment has been successful modeled, next step is applying interphase in 3D models. Moreover, because we only used one 2D image of specimen surface slice to represent all planes contains inclusion in the MPM 3D models, more images from different layers are needed to assemble a more accurate 3D model. The modeling also shows the experiments should work best if the inclusion is as close to the surface as possible.

Therefore future experiments should keep the specimen thin and use tomography methods to characterize the full 3D structure of the specimens.

## BIBLIOGRAPHY



- Alireza Ashori. (2008) Wood–plastic composites as promising green-composites for automotive industries! *Bioresource Technology* 99: 4661–4667
- Anatole A. Klyosov, Anatoliĭ Alekseevich Klesov, Wood-plastic composites
- Anke Schirp and Michael P. Wolcott. (2004) Influence of fungal decay and moisture absorption on mechanical properties of extruded wood-plastic composites. *J Mater Sci* (2006) 41:5386–5390
- Bardenhagen, S.G., Brackbill, J.U., and Sulsky, D. (1998) Shear deformation in granular materials.
- Bardenhagen, S.G., Brackbill, J.U., and Sulsky, D. (2000) The material-point method for granular materials *Comput. Methods Appl. Mech. Engrg.* 187: 529-541.
- Bardenhagen, S.G., and Kober, E.M. (2004) The Generalized Interpolation Material Point Method. *Tech Science Press cmes*, vol.5, no.6, pp.477-495.
- Beuth, L., Coetzee, C.J., Bonnier, P. and van den Berg, P. (2007) Formulation and validation of a quasi-static material point method. In 10th International Symposium on Numerical Methods in Geomechanics.
- Bismarck, A., Baltazar-Y-Jimenez, A., Sarlkakis, K. (2006) Green composites as Panacea? Socio-economic aspects of green materials. *Environment, Development and Sustainability* 8 (3), 445–463.
- Chen, Y., Sun, L., Chiparus, O., Negulescu, I., Yachmenev, V., Warnock, M. (2005). Kenaf/ramie composite for automotive headliner. *Journal of Polymers and the Environment* 13 (2), 107–114.
- Clemons, C. (2002) Wood-plastic composites in the United States: The interfacing of two industries. *Forest. Prod. J.* 52:10-18.
- Coetzee, C.J. (2004) The modelling of granular flow using the particle-in-cell method. PhD thesis, University of Stellenbosch, South Africa.
- David W. Green, Jerrold E. Winandy, and David E. Kretschmann. (1999) Mechanical Properties of Wood. *Wood handbook*, 4: 2-8.
- Fu, X.L., Chung, D.D.L. (1997) Single-fiber electromechanical pull-out testing and its application to studying the interface between steel fiber and cement. *Composite Interfaces*, Vol. 4, No. 4, pp. 197-211.
- Harlow F.H.. (1955) A Machine Calculation Method for Hydrodynamic Problems. Los Alamos Scientific Laboratory report LAMS-1956.
- Hashin, Z. (2002) Thin interphase/imperfect interface in elasticity with application to coated fiber composites. *Journal of the Mechanics and Physics of Solids*. 50: 2509 – 2537.

- Huang, S.H., Cortes, P., and Cantwell, W.J. (2006) The influence of moisture on the mechanical properties of wood polymer composites. *J Mater Sci.* 41:5386–5390.
- Ichazo, M. N., Hernandez, M., Albano, C., Gonzalez, J. (2006) Curing and physical properties of natural rubber/wood flour composites. *Macromol. Symp.* 239:192-200.
- International Conference on Woodfiber-Plastic Composites. Forest Prod. Soc., Madison, WI. Pp. 13-17.
- Jacob, M., Joseph, S., Pothan, L. A., Thomas, S. (2005) A study of advances in characterization of interfaces and fiber surfaces in lignocellulosic fiber-reinforced composites. *Compos. Interfaces* 12:95-124.
- Jacob, M., Thomas, S., in press. Biofibres and biocomposites. *Carbohydrate Polymers*. <www.sciencedirect.com>.
- Jiang, H., Kamdem, D. P. (2004) Development of poly(vinyl chloride)/wood composites. A literature review. *J. Vinyl Addit. Technol.* 10:59-69.
- Johnson, C. (1987) Numerical solution of partial differential equations by the finite element method. Cambridge University Press.
- Johnson, D. A., Urich, J. L., Rowell, R. M., Jacobson, R., Caufield, D. F. (1999) Weathering characteristics of fiber-polymer composites. In: *Proceedings of the fifth international conference on woodfiber-plastic composites*, Madison, WI. pp. 203-209.
- Johnson, N.L. (1996) The legacy and future of computational fluid dynamics at Los Alamos. In *Proceedings of the 1996 Canadian CFD Conference*
- Kelly, A. and Tyson, W.R. (1965) Tensile properties of fiber-reinforced metals: copper/tungsten and copper/molybdenum. *Journal of the Mechanics and Physics of Solids*, 13, 329-350.
- Kim, B. W. and Nairn, J. A. (2002) Observations of Fiber Fracture and Interfacial Debonding Phenomena Using the Fragmentation Test in Single Fiber Composites. *Journal of Composite Materials*, 36, 1825-1858.
- Kim, H.S., Yang, H.S., Kim, H.J. (2005) Biodegradability and mechanical properties of agro-flour-filled polybutylene succinate biocomposites. *J. Appl. Polym. Sci.* 97:1513-1521.
- Marek Kociszewski, Cezary Gozdecki, Arnold Wilczyński, Stanisław Zajchowski, Jacek Mirowski. (2011) Effect of industrial wood particle size on mechanical properties of wood-polyvinyl chloride composites. *European Journal of wood and wood products*. 19, Feb, pp.1-6.
- Manas Chanda, Salil K. Roy. (2008) Industrial polymers, specialty polymers, and their applications. Part 2: 151-153.

- Marshall, P. and Leonard, J. (1992) The dependence of data from single fiber pull-out tests on the loading direction. *J. Mater. Sci. Lett.* 1992, 11, 1401.
- Michael Carus. (2010) Market Growth WPC. In Third German WPC Congress.
- Morris, P. I., Cooper, P. (1998) Recycled plastic/wood composite lumber attacked by fungi. *Forest. Prod. J.* 48:86-88.
- Nairn, J. A. (2003) Material Point Method Calculations with Explicit Cracks. *Computer Modeling in Engineering & Science*, 4:649-664.
- Nairn, J.A. (2005) Numerical simulations of transverse compression and densification in wood. *Wood and Fiber Science*. 576-591.
- Nicholas P. Cheremisinoff, *Handbook of engineering polymeric materials*. pp. 831-832.
- Roger M. Rowell. (2004) *Handbook of wood chemistry and wood composites*. 373-374
- Sauer, B.B. and Dipaolo, N.V. (1995) Development of Micro-Debond Methods for Thermoplastics Including Applications to Liquid Crystalline Polymers. *J. Adhesion*. Vol. 53, pp. 245-259.
- Schauwecker, C., Morrell, J. J., McDonald, A. G., Fabiyi, J. S. (2006) Degradation of a wood-plastic composite exposed under tropical conditions. *Forest Products Journal (Forest. Prod. J.)* Vol.56:123-129.
- Smith, P. and K.D. Bright. (1999) New market development for wood plastic composite decking products. *Proc. Fifth International Conference on Woodfiber-Plastic Composites*. Forest Products Soc. Madison, Wisconsin 257-268 p.
- Smith, P. M. (2001) U.S. woodfiber-plastic composite decking market. *Forest Products Journal (Forest. Prod. J.)* Vol. 52:10-18.
- Stark, N.M., Rowlands, R.E. (2003) Effects of wood fiber characteristics on mechanical properties of wood/polypropylene composites. *Wood Fiber Sci.* 35:167-174.
- Stefanie Feih and Karen Wonsyld. (2004) Testing procedure for the single fiberfragmentation test. *Risø-R-1483(EN)*.
- Sulsky, D., Chen, Z., and Schreyer, H.L. (1994) A particle method for history-dependent materials. *Computer Methods in Applied Mechanics and Engineering*, 118:179-196.
- Sulsky, D., Zhou, S.J., and Schreyer, H.L. (1995) Application of a particle-in-cell method to solid mechanics, *Comput. Phys. Commun.* 87, 236-252.

- Su, C and Anand, L. (2003) A new digital image correlation algorithm for whole-field displacement measurement. Available: <http://hdl.handle.net/1721.1/3749>. Last Access: 10/19/2011.
- Tan, H.L and Nairn, J.A. (2002) Material Point Method for Dynamic Energy Release Rate Calculations. Computer Methods in Applied Mechanics and Engineering, 191:2095-2109.
- The Freedonia Group. (2009) Wood-Plastic Composite & Plastic Lumber to 2013. Market research report
- Thomas Lundin, Steven M. Cramer, Robert H. Falk, and Colin Felton. (2004) Accelerated Weathering of Natural Fiber-Filled Polyethylene Composites. Journal of materials in civil engineering. 547-555.
- VTK File Formats for VTK Version 4. 2. VTK User's Guide. Available: <http://www.vtk.org/VTK/img/file-formats.pdf>. Last Access: 10/10/2011.
- Zhou, X.F., Nairn, J.A., Wagner, H.D. (1999) Fiber-matrix adhesion from the single fiber composite test: nucleation of interfacial debonding. Composites, Part A: 30, 1387-1400.

**Appendix A: Matlab code for qualitative and quantitative analysis**

Objective:

Using Matlab software for qualitative and quantitative analysis

Responsibility:

Project manager or designee: Xiang Lin

Instruction:Scope:

This document describes the Matlab code for qualitative and quantitative comparison of copper wire/wood particle embedded in polymer matrix specimen.

```

% User select a file
[fileName,fldrPath,FilterIndex] = uigetfile('*.vtk','Select VTK File');
if(fileName==0)
    return
end

% read all data
[VTKheader,VTKdata] = ReadVTKFile(fldrPath,fileName,{'totalstrain'});
%[VTKheader,VTKdata] = ReadVTKFile(fldrPath,fileName,{'stress'});

% find x and y limits
VTKfields = {VTKheader(:).parname};
spacing = VTKheader(strncmpi('SPACING',VTKfields)).parval;
origin = VTKheader(strncmpi('ORIGIN',VTKfields)).parval;

% cell size in x and z direction (assume y is same as x)
d = spacing(1);
dz = spacing(2);
gridX0 = fix(origin(1)/d-.1);
gridY0 = fix(origin(2)/d-.1);

% totalstrain is data set 1, exx, eyy, and exy are 1, 5, 2
% DIC strains for exx, eyy, and exy, are 10, 11, 12
% but note that VTK starts in lower-left and not upper left
vtkID = 2;
dicID = 12;
levels = 10;

dims = size(VTKdata(1).datval);

zlevel = 03;

Ve=squeeze(VTKdata(1).datval(vtkID,:,: ,zlevel))';
Ve2=squeeze(VTKdata(1).datval(vtkID,6:83,4:58,zlevel))';
vsize = size(Ve);
vx = vsize(2);
vy = vsize(1);

figure(50); contourf(Ve2);
%return

%-----
% importDICdata

fpath = 'C:\Users\linx\Documents\MATLAB\VTK-DIC\DICData\';
fname = 'Wire0040.csv';

newdata = importdata([fpath fname]);

% plot position of the data points
% plot(newdata.data(:,1),newdata.data(:,2), 'r.')

dataheaders = newdata.colheaders;

```

```

% X and Y Data
DICx=newdata.data(:,1);
DICy=newdata.data(:,2);

% number of x and y coordinates in the data
dx = length(unique(DICx));
dy = length(unique(DICy));

% 10 = exx, 11 = eyy, 12 = exy
eDIC=newdata.data(:,dicID);

% arrange so first point is lower-left point
eDICA=flipud(transpose(reshape(eDIC,dx,dy)));

% change sign of shear stresses
if (dicID==12)
    eDICA = -eDICA;
end

%figure(2); contourf(eDICA);
%return

%-----
% need to overlap DIC data with MPM grid lines

u=404.1381;      % pixels/mm from 753/1.8632
ud=u*d;          % pixels per cell

% DIC analysis image relative to original image (y is zero on top)
dicOx=748;
dicOy=317;
dicWidth=850;      % from (dicOx-mpmOx)/u to (dicOx+disWidth-mpmOx)/u
dicHeight=650;     % from (mpmOy+mpmHeight-(dicOy+dicHeight))/u to
                   %      (mpmOy+mpmHeight-(dicOy+dicHeight))/u

% Image extracted for MPM analysis (y is zero on top)
mpmOx=800;
mpmOy=375;
mpmWidth=753;      % from 0 to mpmWidth/u
mpmHeight=543;     % from 0 to mpmHeight/u

% Convert DIC data to plot in MPM grid numbers
% Non integers here because off grid
% DIC image width = (1598-748)/u = 850/u = 2.1032
% DIC image height = (967-317)/u = 650/u = 1.6084
dgx1=(dicOx-mpmOx)/ud;
dstep=5/ud;
dgx2=dgx1+(dx-.99)*dstep;
DICgx=dgx1:dstep:dgx2;
dgy1=(mpmOy+mpmHeight-(dicOy+dicHeight))/ud;
dgy2=dgy1+(dy-0.99)*dstep;
DICgy=dgy1:dstep:dgy2;
[X,Y]=meshgrid(unique(DICgx),unique(DICgy));

% Interpolate DIC data to MPM grid lines

```



```

% MPM grid lines with (0,0) at corner of image used for MPM
% These are the entries in the read VTK file
% Origin is lower left now
vtkOx=gridX0;
vtkOy=gridY0;
vtkWidth=vx-1;
vtkHeight=vy-1;

VTKgX=vtkOx:(vtkOx+vtkWidth);
VTKgY=vtkOy:(vtkOy+vtkHeight);
[Xgrid,Ygrid]=meshgrid(VTKgX,VTKgY);

eDICToV = interp2(X,Y,eDICA,Xgrid,Ygrid);

step = (emax-emin)/levels ;
eDICToV(1,1)=emin;
eDICToV(1,2)=emax;
Ve(1,1)=emin;
Ve(1,2)=emax;
%eDICToV2=squeeze(eDICToV(:,3:85));
eDICToV2 = eDICToV(2:61,2:85);
figure(1); contourf(Xgrid,Ygrid,eDICToV);
figure(2); contourf(Xgrid,Ygrid,Ve);
figure(51); contourf(eDICToV2);
%figure(4); contourf(eDICToV2);
%return

% MPM grid (3 elements inside object)
bXmin=3;
bYmin=3;
bWidth=70;
bheight=47;

% fiber origin and size
fXmin=21;
fYmin=23;
fWidth=36;
fHeight=11;

% number of areas
numAreas=9;

xmax = fix(fXmin+0.2*fWidth);
minWidth = fWidth-2*(xmax-fXmin);
xmin = 3;
xstep = fix((xmax-xmin)/numAreas);
xs = xmax:-xstep:xmin;
xlen = size(xs);

ymax = fix(fYmin + 0.1*fHeight);
minHeight = fHeight-2*(ymax-fYmin);
ymin = 3;
ystep = fix((ymax-ymin)/numAreas);
ys = ymax:-ystep:ymin;

```

```

ylen = size(ys);

bmax = xlen(2);
if(ylen(2)<bmax)
    bmax=ylen(2);
end

display(['Error Results for Strain: ' num2str(vtkID) ' z level = '
num2str(zlevel)])

Er1 = [];
for i=1:bmax

    cmpOx = xs(i)-gridX0;
    cmpOy = ys(i)-gridY0;
    cmpWidth = minWidth+2*(i-1)*xstep;
    cmpHeight = minHeight+2*(i-1)*ystep;

    areasize(i) = cmpWidth*cmpHeight;

    cx = (gridX0+cmpOx):(gridX0+cmpOx+cmpWidth);
    cy = (gridY0+cmpOy):(gridY0+cmpOy+cmpHeight);
    [Xc,Yc] = meshgrid(cx,cy);

    eDICcmp = eDICToV(cmpOy:(cmpOy+cmpHeight),cmpOx:(cmpOx+cmpWidth));
    Vecmp = Ve(cmpOy:(cmpOy+cmpHeight),cmpOx:(cmpOx+cmpWidth));
    AveDICStrain(i) = mean2(eDICcmp);
    AveVTKStrain(i) = mean2(Vecmp)

    Ediff = (Vecmp-eDICcmp).^2;
    Enorm = (eDICcmp).^2;
    Er1(i) = sqrt(sum(Ediff(:))/sum(Enorm(:)))*100;

    eDICcmp(1,1)=emin;
    eDICcmp(1,2)=emax;
    %figure(2*i+1); contourf(Xc,Yc,eDICcmp)
    Vecmp(1,1)=emin;
    Vecmp(1,2)=emax;
    %figure(2*i+2); contourf(Xc,Yc,Vecmp)
end

aveDICVnew = mean2(eDICcmp)
aveDICV = aveDICVnew;
aveVTKVnew = mean2(Vecmp)
aveVTKV = aveVTKVnew;

for i=1:bmax

    cmpOx = xs(i)-gridX0;
    cmpOy = ys(i)-gridY0;
    cmpWidth = minWidth+2*(i-1)*xstep;
    cmpHeight = minHeight+2*(i-1)*ystep;

    areasize(i) = cmpWidth*cmpHeight;

```

```

cx = (gridX0+cmpOx):(gridX0+cmpOx+cmpWidth);
cy = (gridY0+cmpOy):(gridY0+cmpOy+cmpHeight);
[Xc,Yc] = meshgrid(cx,cy);

eDICcmp = eDICtoV(cmpOy:(cmpOy+cmpHeight),cmpOx:(cmpOx+cmpWidth));
Vecmp = Ve(cmpOy:(cmpOy+cmpHeight),cmpOx:(cmpOx+cmpWidth));

Ediff = (Vecmp-eDICcmp).^2;
Enorm = (eDICcmp).^2;
Er1(i) = sqrt(sum(Ediff(:))/sum(Enorm(:)))*100;

eDICcmp(1,1)=emin;
eDICcmp(1,2)=emax;
%figure(2*i+1); contourf(Xc,Yc,eDICcmp)
Vecmp(1,1)=emin;
Vecmp(1,2)=emax;
%figure(2*i+2); contourf(Xc,Yc,Vecmp)

C = size(eDICcmp);
M = ones(C(:,1),C(:,2));
AveDIC = aveDICV.*M;
SubDIC = eDICcmp-AveDIC;

D = size(Vecmp);
N = ones(D(:,1),D(:,2));
AveVTK = aveVTKV.*N;
SubVTK = Vecmp-AveVTK;

%figure(50); contourf(Xc,Yc,SubDIC)
%figure(51); contourf(Xc,Yc,SubVTK)

Ediff2=(SubDIC-SubVTK).^2;
Enorm = (eDICcmp).^2;
Er2(i) = sqrt(sum(Ediff2(:))/sum(Enorm(:)))*100;
end

xp = 1:bmax;
%figure(2*bmax+3); plot(xp,Er1);
rawError = Er1';
B = areasize';
DevError = Er2';

```